UNIVERSITAT POLITÈCNICA
DE CATALUNYA
BARCELONATECH

The Institute
of Photonic
Sciences

All optical manipulation of a single nitrogen-vacancy centre in nanodiamond

MICHAEL GEISELMANN

under the supervision of

PROFESSOR ROMAIN QUIDANT

submitted this thesis in partial fulfillment

of the requirements for the degree of

DOCTOR

by the

UNIVERSITAT POLITÉCNICA DE CATALUNYA
BARCELONA, 2014

To my wife and parents

To Gérard and Chavela

Acknowledgements

The thesis and the work for the last four and a half years would not have been possible without the support of many people. I want to start thanking Romain Quidant, who gave me the opportunity to work in this exciting research field. He motivated me, when I had hard times in the lab and gave me the freedom to choose my way to get to the results presented in this thesis. I highly appreciated that. Furthermore I was lucky to work with Frank Koppens in the lab and with Javier García de Abajo on the theory side. I learned a lot from all of them.

I want to thank those people who were directly involved in my research project: Mathieu for the help getting started and Renaud for the help getting finished apart from all the hours of physics discussion that I learned a lot from. Thanks to Jan R. for the fabrication of hundreds of samples to test and measure and all the tricks for working in an optics lab.

In the dark lab I seldom was lonely. My lab mates Jon, Esteban, Chris, Giorgio, Mathieu, Johann, Bea made the time in the lab unforgettable. Thanks for all the good music Jon!

Thanks to my office mates Mariale and Valeria and shortly Yury and Pascal who made the work atmosphere very pleasant.

I must thank each of the PNO group members, for discussions about physics in the meetings and over coffee and fun times during and after work. Mark, Giorgio, Mau, Guillaume, Mathieu, Srdjan, Jose, Esteban, Jon, Jan, Jan R., Sudhir, Sukanya, Jordi, Renaud, Johann, Pascal, Mariale, Valeria, Valeria, Bea, Chris, Sebas, Francesco, Marko, thanks for the good times!

I want to thank ICFO administration, human resources, purchasing and the mechanical and electronic workshops. They made the paper work and getting started at ICFO very smooth. Thanks to Xavi and Jose Carlos and their teams I could focus on my research and get support from the mechanical and electronic side to build the experiment.

Also I want to mention the people apart from those above who made life inside and outside ICFO very enjoyable and helped me getting through the PhD: Sebas, Marta, Pablo, Nicolo, Gabi, Michela, Stefan, Mussie, Anjana, Benni, Dominik, Iris, Nili, Jana, Tai, Laura, Eyal, Camila, Paulinha, Gustavo, Alba, Christian, Chris H.

Last but certainly not least I want to thank my parents, my sisters and my family in Germany who always supported me in my decisions. Vielen Dank, dass ihr immer für mich da seid!

Michelle, gracias por siempre estar aquí para mí y soportar mi humor cuando algo no salió tan bien en el laboratorio. Te amo!

Resumen

La interacción de fotones con emisores cuánticos individuales como los centros de nitrógeno-vacante (NV) es esencial para la elaboración de futuros dispositivos integrados de óptica cuántica. Una estrategia prometedora para alcanzar este objetivo es de aprovechar de los últimos avances de la nano-óptica para aumentar la interacción con emisores individuales, así como fortalecer el acoplamiento entre varios de ellos. Sin embargo, para aprovechar al máximo las capacidades de este matrimonio entre centros de NV y nano-estructuras ópticas se requiere de herramientas adecuadas para controlar con precisión su interacción.

En esta tesis, se utiliza la manipulación óptica para atrapar y manipular en 3D nano-diamantes individuales que contienen un solo centro de NV.

En primer lugar, demostramos el uso de pinzas ópticas como una herramienta para lograr la captura precisa y manipulación espacial tridimensional de nano-diamantes individuales conteniendo un solo centro de NV. Sorprendentemente, encontramos que el eje del centro de NV está casi fija dentro de la trampa y puede controlarse in situ mediante el ajuste de la polarización de la luz del láser de captura. Combinamos este control espacial y angular con la manipulación coherente del espin del centro NV y con medidas de tiempo de vida de fluorescencia de un sistema fotónico integrado. Demostramos que los centros NV atrapados ópticamente pueden servir como una nueva ruta para ambos magnetometría vectorial tridimensional y de detección de la densidad local de estados electromagnéticos.

En un segundo paso, nuestra técnica de manipulación se desarrolló aún más hacia el posicionamiento de un nano-diamante individual en una antena plasmónica. La fuerza de gradiente del campo electromagnético del plasmon excitado actúa como una pinza óptica local para atraer los nano-diamantes funcionalizados a las regiones de mayor aumento del campo de la antena, donde quedan adsorbidos. La proximidad del centro NV inmovilizado en la nano-antena es corroborado por la disminución observada del tiempo de vida de la fluorescencia.

Por otra parte, se observa una disminución de la fluorescencia NV tras la iluminación infrarroja. Identificamos como origen de la disminución de la fluorescencia la promoción del electrón excitado a una banda, que tiene un canal de decaimiento rápido. Esta hipótesis es comprobada por el excelente acuerdo entre nuestro modelo simple de ecuación cinética y el experimento.

Por último, demostramos que un centro NV puede funcionar como un interruptor óptico eficiente y rápido controlado a través de un láser de control infrarrojo independiente. Además, el sistema híbrido formado por un solo NV acoplado a una nano-antena de oro aumenta la profundidad de modulación.

Los resultados presentados en esta tesis demuestran la capacidad de manipular y posicionar nano-diamantes conteniendo un centro NV con pinzas ópticas. Esto allana el camino hacia un sensor de campo magnético y de temperatura en ambiente liquido usando el espin del centro NV. Además, el control de posicionamiento y acoplamiento a nano-estructuras fotónicas y plasmónicas podría tener un impacto para aplicaciones potenciales en circuitos completamente ópticos o dispositivos de óptica cuántica .

Contents

Motivation

Nanotechnology is defined after the European Commission as the manipulation of matter with dimensions at the atomic, molecular and macromolecular scale, where properties differ significantly from those at a larger scale [1]. During the last 30 years, a huge interest has been devoted to understand the new physical properties that appear when reducing the size of matter down to the nanometer scale. To understand these physical, chemical and biological processes from a fundamental point of view, nanometer precision and sensitivities down to the single electron or single photon level are essential. The study of new materials as well as the progress made in fabrication and manipulation techniques with nanometer accuracy have enabled to analyze some of the elementary mechanisms at the nanometer scale and led to their control for potential applications.

For future technology quantum optics is a promising research field relying on photons whose interactions may be mediated by a quantum system [2, 3, 4, 5]. Such a quantum system provides single photon sources that can be employed for nanoscopy, bio-marking as well as for quantum technologies [6, 7, 8, 9]. Since the experimental proof of the quantum nature of light [10], a variety of optical quantum systems have been identified including trapped ions and atoms [11, 12], single molecules [13, 14], quantum dots (QDs) [15, 16] and nitrogen-vacancy (NV) centres [17]. Each of these systems has its advantages and drawbacks: atoms and ions have sharp transition lines and thus have a good two level quantum system, but they have to be trapped in vacuum. QDs and molecules on the other hand are available in a large quantity for a different emission wavelength, which is interesting for potential applications. However it is still challenging to stabilize the emission of a single QD [18, 19] or a single molecule and experiments have to be done at cryogenic temperatures [20] or in a solid state matrix for molecules [21].

In this context NV centres in diamond have attracted much attention because they act as artifical atoms, protected by the stable diamond lattice. At room temperature, they do not have a well defined transition line, due to their phonon interaction. Yet, they have been characterized as a stable single emitter that does not bleach nor blink [17] and they are found in bulk diamond near the surface [22] or in nanodiamonds (NDs) in the range from around 5-100 nm [23]. This size is advantageous because they can be put into biological systems [24, 25] or coupled to plasmonic nanostructures [26, 27, 28] and photonic structures [29, 30, 31, 32, 33] just like fluorescent molecules or QDs. It has been shown that their electric dipole couples to its environment, which was used to design single emitter sources or single photon wave-guiding structures [34, 35, 36]. This coupling to the environment also makes them a good candidate to sense their surrounding electromagnetic local density of state (LDOS).

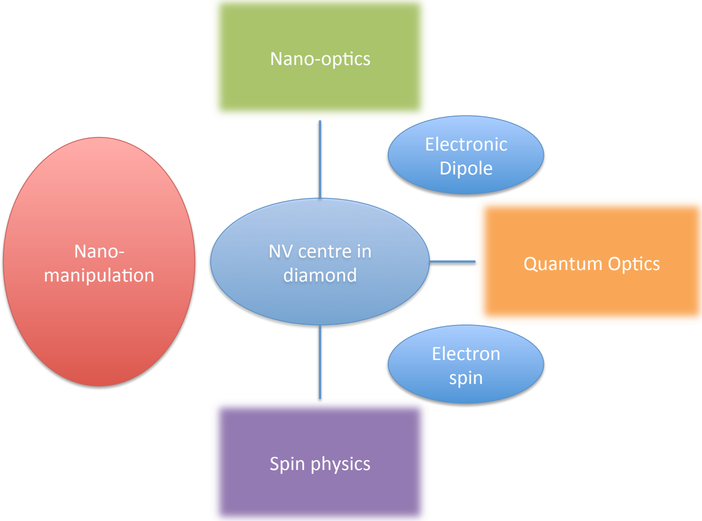

Figure 1: **Overview of the fields involved in this thesis.** The NV centre in diamond plays an important role in spin physics as its electron spin can be used for quantum information as well as for magnetometry. Its electronic dipole can be used as a single photon source, which is relevant for quantum optics as well as for nano-optics. However spatial manipulation of the NV centre is crucial for any of its applications. In this thesis I introduce a novel approach of manipulating nanodiamonds in liquid environment using optical tweezers.

Apart from the electric dipole, the negatively charged NV centre has an electron spin that can be manipulated and read out optically at room temperature

[22]. This electron spin is a very promising quantum system as coherence times of the electron spin in bulk diamond were demonstrated to reach the millisecond range [37]. This property can be used either as a quantum bit for quantum operations [38, 39, 40, 41] as well as a magnetic field sensor with nanometer resolution and sensitivities down to 100 pT / $\sqrt{Hz}$ [42]. Very recently it was even demonstrated that the NV spin can be used to measure temperature [43, 44, 45].

As illustrated in Fig. 1 the unique properties of NV centres are exploited in different contexts and fields of science. Yet, in all applications spatial control of the position of the NV centre is critical.

Manipulation of these NDs has so far been accomplished using an Atomic Force Microscope (AFM) attaching the nanocrystal at the apex of the AFM tip [46, 47, 26, 27, 48, 49, 50]. In this thesis I present a different manipulation approach based on optical trapping that is compatible with complex liquid environments like biological samples or microfluidics. As a non-invasive technique, optical tweezers have been used so far to manipulate micro-meter sized particles with excellent accuracy [51, 52].

In this thesis I study the use of both conventional tweezers and plasmonic tweezers. I show trapping and 3D manipulation of 70 nm NDs using conventional optical tweezers. Both the electric dipole and the electronic spin are exploited as a probe for local density of states and magnetic fields, respectively. In a second experiment I use plasmonic optical tweezers for a deterministic positioning of 40 nm NDs in the hotspot of a plasmonic antenna. I furthermore discovered that the NIR laser line used in both trapping approaches can be used to fast and efficiently switch the fluorescence of the NV centre by promoting the electron to a higher energy dark state.

Chapter 1 gives an overview of the NV centre in diamond and its state of the art manipulation techniques.

In Chapter 2 we present the experimental platform combining optical tweezers with manipulation and read out of the electron spin and measurement of g^2 and lifetime of the electric dipole.

Chapter 3 presents the results in 3D optical manipulation of a single ND hosting a single NV centre. The optical tweezers assure translational manipulation in three dimensions with an additional angular degree of freedom using the polarization of the laser beam. The achieved control is used to demonstrate probing of magnetic fields as well as electromagnetic LDOS in a liquid environment.

In Chapter 4 I show deterministic positioning of single NDs in the hot spot of a plasmonic nanostructure using the near field assisted trapping. We also systematically study the optical properties of the emitter coupled to the metal nanostructure.

In Chapter 5 I present a new transition process promoted by the absorption of two colour photons. The presence of an off-resonant near infrared (NIR) laser is shown to promote the electron of the excited NV centre to a dark fast decaying state.

1

The Nitrogen Vacancy centre in diamond

The optical transparency of a diamond crystal is due to its large band gap and thus the absence of electronic transitions at energies in the visible spectrum. However the transparency can be altered by the presence of a defect in the carbon matrix. If the defect is stable inside the diamond matrix, it gives rise to a new energy level structure inside the diamond bandgap. Transitions within this new energy level can interact with the lattice phonons and can thus create phonon sidebands. The defect centre can be excited by an appropriate light source and promotion of the electron to the excited state can result in emission of a zero phonon line (ZPL) and a broadened phonon side band of the electronic-phonon transitions. If the energy gap of the created level is smaller than the bandgap of the hosting material the emission is not absorbed and can be detected as fluorescence. Since this fluorescence gives colour to an originally transparent diamond, these defects are called colour centres. Among the large amount of colour centres in diamond (more than 500) only less then ten of them have been characterized as bright single photon sources [9].

Over the past decade nitrogen-vacancy (NV) defect centres in diamond got very much attention. They are stable single photon emitters at room temperature [53, 17, 9] and were used to develop single photon sources [9, 54, 55, 56]. Their stable emission in the visible spectrum made them ideal to study light matter interactions with photonic [57, 30, 32, 58, 59] and plasmonic nanostructures [60, 26, 27, 28, 35], where NV centres serve as quantum light sources. The stable photo-emission also brought NV centres in nanodiamond (ND) to biology as a fluorescent bio-marker in cells [61, 24] and there are propositions to image neuron networks [62].

Besides the stable photon emission of its electric dipole, the negative charged NV^- centre can also operate as a quantum bit at room-temperature based on its free electron spin that can be read out optically [63, 64]. The NV^- centre has been used to build quantum registers [39, 65, 37] using nearby N and C^{13} atoms, to demonstrate entanglement between two adjacent NV^- centres [66] and to develop all kind of sensors ranging from magnetic [49, 67, 42, 68, 69, 70, 71, 72, 73] and electric field probes [74] to temperature sensors [75, 45, 43, 44].

In this chapter I discuss the basics of the NV centre physics and present the state of the art in the spatial manipulation of NDs hosting NV centres.

1.1 Physics of the Nitrogen Vacancy centre

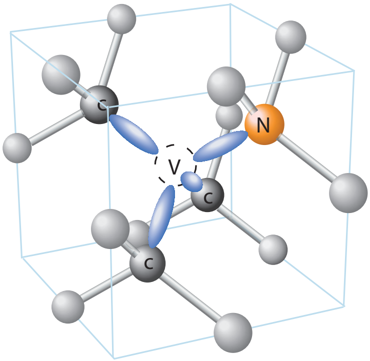

Figure 1.1: **Schematic of the NV centre in diamond.** It consists of a substitutional nitrogen atom (N) adjacent to a vacant lattice site (V) within the carbon (C) lattice (Image taken from [55]).

The NV centre is a defect centre in the diamond carbon lattice, containing a nitrogen atom and a missing carbon atom (vacancy) that form a C_{3V} symmetry (Fig. 1.1). It can exist in two charged states. The neutral charge state NV^0 has five unpaired electrons, four from the neighboring carbon atoms and one from the nitrogen atom [76]. For the negatively charged NV^- centre, electron spin resonance measurements indicate that the centre has an electron paramagnetic ground state with an electron spin angular momentum S=1. It is thus assumed that it has six electrons, where two electrons are unpaired [77, 78].

1.1.1 Energy level of the NV centre

The characteristic features of the NV^- and NV^0 are the Zero Phonon Lines (ZPLs) at 1.945 eV (637 nm) [79] and 2.156 eV (575 nm) [80], respectively and their related vibronic phonon side band at lower energies, where photons are emitted (Fig. 1.2). Despite the intensive studies during the last decades, still new insights in the energy level have recently been gained [81] and still have to be gained. For example the relative energies of the triplet and singlet states of the NV^- and of the doublet and quartet states of the NV^0 are still unknown [82].

In this thesis the focus lies on the negative charged NV^- centre because of its electronic spin that can be optically prepared and read out via a third metastable state, as explained in section 1.1.2. Consequently, the generic notation NV in this thesis refers to the negative charge state, if not mentioned otherwise.

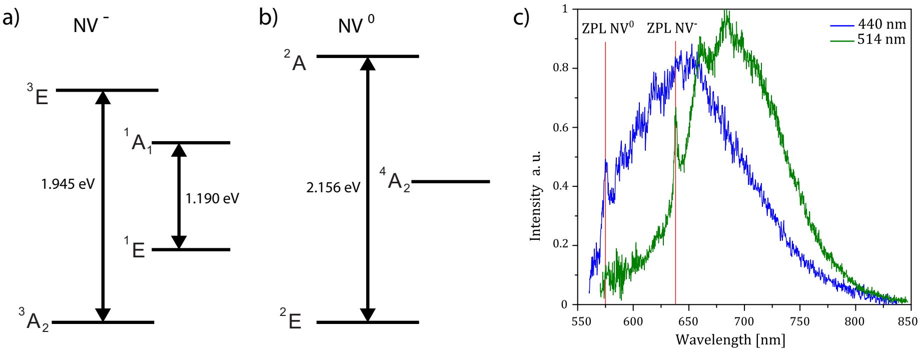

Figure 1.2: **Electronic structure of the NV centre.** Schematics of the known optical transistions of the NV^- (a) and NV^0 (b) charged state. The observed zero phonon lines (ZPLs) are indicated with their energies in a) and b) and the emission spectrum for NV^- and NV^0 is shown in c) upon excitation with 514 nm and 440 nm laser lines, respectively. The ZPLs are marked with a red line. (Spectra taken from [83])

1.1.2 Initialization, preparation and read out of the spin state

As illustrated in Fig. 1.1, NV centres in a diamond lattice obey a C_{3V} symmetry. This is the foundation of theoretical models used to understand the energy level of a NV centre. There are two approaches: ab initio calculations [84, 85, 86, 87] and semi-empirical molecular model of deep level defects in semiconductors [77, 78, 88, 89, 90, 91, 92]. Both models disagree in some aspects and complement themselves in others [82]. Nevertheless they agree that, in a first approximation, a NV centre consists of a triplet groundstate with $m_s = 0$ and $m_s = \pm 1$ sublevels, a triplet excited state with $m_s^* = 0$, $m_s^* = 1$ and $m_s^* = -1$ and one metastable singlet state ^1A (Fig. 1.3). The $m_s = \pm 1$ sublevels are degenerate at zero external magnetic field and for no internal strain.

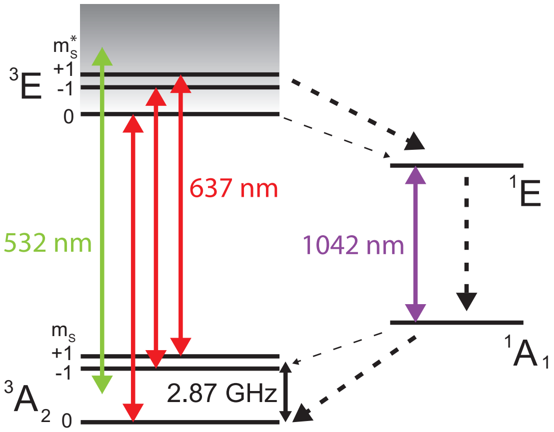

Figure 1.3: **Level structure of a NV centre.** The triplet groundstate $^3A_2$ is split in a $m_s = 0$ and a $m_s = \pm 1$ sublevel by 2.87 GHz. Off-resonant green excitation ($\lambda = 532$ nm) brings the electron to the excited triplet state, from where it decays emitting fluorescence (ZPL = 637 nm). The ZPL at 1042 nm of the metastable state could only be observed after exciting the system with green laser light [90, 93]. Radiative transitions are represented by solid lines, nonradiative by dashed lines. Thicker dashed lines represent stronger transitions. Due to the different intersystem crossing rates (dashed lines), spin polarization of the NV$^-$ centre to the $m_s = 0$ state is possible.

The NV centre can be excited with an off-resonant 532 nm laser [22]. Starting from the $m_s = 0$ sublevel, the system is excited to the $m_s^* = 0$ sublevel of the excited state, following the selection rules of a spin conservative transition, and decays by emitting fluorescence with a ZPL at 637 nm. Consequently, when promoted from the $m_s = \pm 1$ sublevel to the excited $m_s^* = \pm 1$ sublevels, there is a higher probability to decay via intersystem transitions to the metastable singlet state and from there to the $m_s = 0$ triplet groundstate without emitting a photon. This enables the spin polarization of the NV centre into the $m_s = 0$ sublevel state of the triplet ground state [77, 78].

Spin polarization is very important for applications to quantum information. Indeed, the initial state has to be known before undertaking a sequence of operations. For every room temperature implementation of a NV centre as a single electron spin the same process applies for preparation, control and read out of the spin. This sequence is sketched in Fig. 1.4.

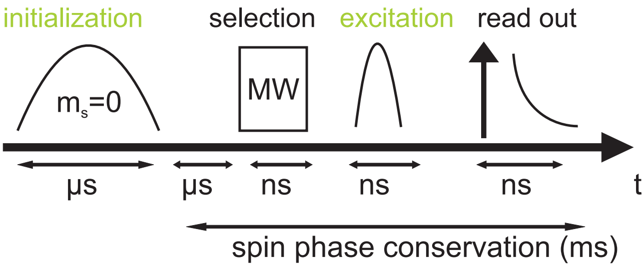

Figure 1.4: **Process for spin polarization, spin preparation and read out the electronic spin.** First a green pulse is applied to spin polarize the system into the $m_s = 0$ state. In a second step the spin state can be prepared applying a microwave pulse and finally apply another green illumination to read the spin state.

As the paramagnetic groundstate is split into a spin singlet ($m_s = 0$) and a spin douplet ($m_s = \pm 1$) by approximately 2.87 GHz, it can be manipulated with a microwave field [94]. At the suitable microwave transition frequency populations of these two levels can be inverted. For instance, when the system is initialized to the $m_s = 0$ sublevel, upon a microwave pulse of the right length and power, the spin is flipped and the system ends up in the $m_s = \pm 1$ sublevel.

While the spin polarization can be controlled by combining suitable optical and microwave illumination, the read out of the spin state can be achieved by monitoring the intensity of the NV fluorescence. In particular, the fluorescence intensity drops by up to 30 % when the system is excited from the $m_s = \pm 1$ groundstate sublevel compared to the excitation from $m_s = 0$ sublevel. This is because the intersystem decay of the excited $m_s = \pm 1$ state has a higher transition rate to the metastable state than from the $m_s = 0$ excited state. The optical spin read out is experimentally described in the Optical Detectable

Magnetic Resonance Spectroscopy section 2.3.

1.2 NV centres for sensing applications

The electron spin in the NV centre is an excellent probe for AC and DC external magnetic fields [49, 67, 42, 68, 69, 70, 71, 72] as well as for electric fields [74] or even temperature [75, 45, 43, 44]. Additionally the electric dipole can also be used to sense the electromagnetic local density of optical states (LDOS) [95, 96]. However the sensitivity and resolution are dependent on the coherence time of the electron spin, the proximity to the sample and the number of NV centres in the sensing volume [82]. Two kinds of architectures for sensing with NVs can be used: NV centres in bulk diamond or in NDs.

1.2.1 Bulk diamond versus nanodiamond

NV centres arise randomly from the presence of natural nitrogen impurities in diamond, but it is possible to create them artificially. Ultra-pure bulk diamond crystals are grown with chemical vapor deposition (CVD) or high pressure high temperature (HPHT) synthesis. In a second step ion implantation in combination of annealing made it possible to create NV centres at predefined positions with nanoscale accuracy [97, 98, 99]. However there is no 100 % certainty that the NV is formed at the predefined position, as the vacancy has to migrate towards the implanted nitrogen atom [99]. The advantage using this technique on ultra-pure bulk diamond is that it has a very low concentration of additional nitrogen or ^{13}C atoms, which are the main causes for decoherence [100]. Spin coherence times of T_2 >1.8 ms have been demonstrated recently with decoupling techniques [101, 102, 103, 37]. Furthermore it has been shown that it is possible to implement NV centres only a few nanometers from the diamond surface [104], which enables to sense a sample lying on the diamond surface.

Alternatively, CVD grown nanocrystal diamonds with sizes ranging from 5 nm to 100 nm can also host single NV centres [9]. Up to now the NV centres in NDs feature large decoherence, due to nirogen and ^{13}C impurities in the crystal and surface effects [105]. Finally their radius determines the proximity of the electron spin to the sample. Even though the size of the CVD grown ND can be controlled, it is still a challenge to control the actual position of the NV centre inside the nanocrystal [106].

Although NV centres in bulk diamond have much longer coherence times and were used for several sensor applications as well as for quantum operations, the possible pre-selection of NV centres in NDs and their ability to be transported to the location of interest makes ND interesting for sensing and quantum technology. Various research teams are nowadays improving the quality of the NDs to be able to compete with the properties of ultra-pure bulk diamond [107, 108].

1.2.2 State of the art in nanodiamond manipulation

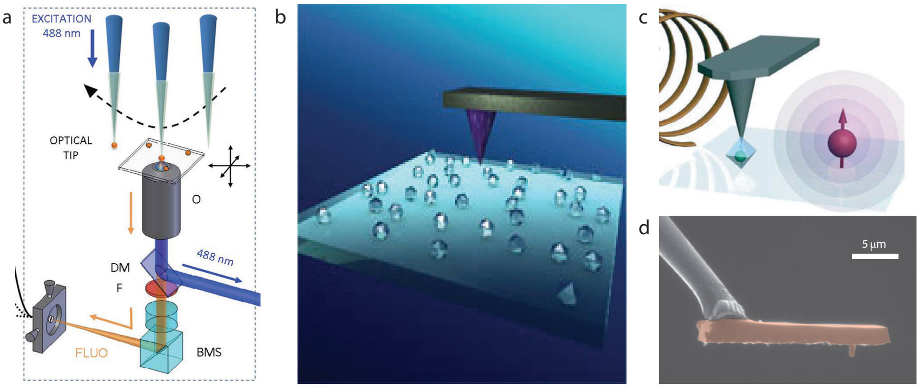

Figure 1.5: **Existing nanodiamond manipulation techniques.** a) Picking up a ND with an optical fiber. b) Pushing the NDs with an AFM tip. c) Sticking a pre-selected diamond to an AFM tip. d) Etching an ultra-pure diamond with a NV centre in the tip and sticking it to an AFM cantilever. (Images are taken from [48, 109, 49, 50])

In parallel to the improvement of the intrinsic properties of the ND, the nanosize of the NDs was shown to be advantageous in several experimental configurations, allowing one to place a single electric dipole in very close proximity to photonic [54, 110] and plasmonic [111, 26, 27, 48, 112, 28] systems. Consequently coupling of the quantum emitter to the nanostructure or fabrication of customizable single-photon sources [27, 28] were achieved. Furthermore, a mobile single NV centre was shown to be useful as a nanoprobe of a magnetic field [49, 69, 42, 71, 50] or a probe for the electromagnetic local density of optical states (LDOS)[27, 26].

Manipulation of single NDs has so far been achieved by using scanning probe-based approaches such as atomic force microscopy (AFM) as shown in Fig. 1.5. One way is to push the NDs on the sample with an AFM tip [26]. However, in order to get a large number of position measurements, this technique is rather cumbersome. Another approach is to stick the ND at the apex of an AFM tip or a tapered optical fiber [49, 48, 54]. This technique served as a scanning probe with a single NV centre [49, 69, 71, 48, 113, 54]. More recently an AFM cantilever featuring a single NV at the extremity of a tip was directly engineered in a ultra-pure bulk diamond [50].

Although these approaches have led to a remarkable level of control, positioning of the NV at the AFM tip is cumbersome. Also, the presence of the host tip can affect the intrinsic properties of the NV centre as well as the local fields being probed. Furthermore, this AFM-based approach typically operates in gas environments, whereas liquid-phase environments are generally required for bio-applications. Importantly, no technique has so far demonstrated in situ control over the orientation of the NV axis, which is critical for vectorial magnetic and electromagnetic sensing based on a single spin or optical dipole, as well as for the implementation of quantum information-processing schemes.

To overcome the problems encountered by the AFM-based technique, I developed a platform where a single ND hosting a single NV centre can be manipulated in liquid using optical tweezers. In chapter 2 the technical details of this manipulation platform are presented. In chapter 3 I demonstrate the potential of this platform for magnetic and LDOS sensing. Furthermore in chapter 4 a new approach to position NDs close to plasmonic antennas is presented, taking advantage of the near field enhancement of the plasmonic system.

2

Experimental Setup

The original goal of my thesis was to develop and test a new approach to manipulate a single NV centre using optical tweezers. For that purpose I designed and built an experimental setup that combines an optical trap to capture the ND in solution with the spin manipulation and optical read out of the NV centre.

In this chapter I present the experimental details of the optical trapping setup, the fluorescence read out and the spin manipulation of a NV centre in diamond. First in section 2.1 the optical setup is presented as a whole and then each part of it is successively detailed in the following three sections.

Section 2.2 focuses on the fluorescence detection of the NV centre in the diamond. The excitation and detection path as well as the different options for collecting the fluorescence signal from a single NV centre are presented. This includes fluorescence imaging, fluorescence spectroscopy, time resolved lifetime and correlation measurements.

Section 2.3 presents the spin manipulation techniques using microwave fields. As discussed in chapter 1 the spin state of a NV centre can be readout optically. Here, the experimental implementation of the radio frequency system as well as the sequences to manipulate the spin of the NV centre are detailed.

Finally section 2.4 describes the principles of optical tweezers and its implementation to trap a single ND.

2.1 Optical Setup

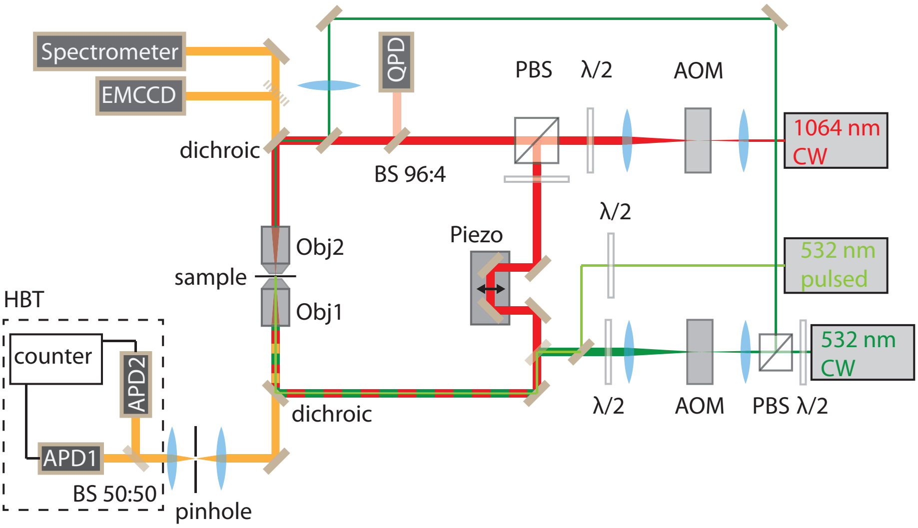

Figure 2.1: **Sketch of the optical setup.** The trapping laser (CW, λ=1064 nm: red line) is first focused through an acousto-optic modulator (AOM) and then separated into two beams at a polarizing beam splitter (PBS) to be focused through two different objectives (Obj1, Obj2) to the same point at the sample plane. The excitation laser for the NV centre (CW, λ=532 nm: green line) is split at the output of the laser. One beam is focused through an AOM and then combined with the trapping laser to be focused to the same point at the sample plane. The second beam is focused at the back-aperture of the Obj2 to illuminate a large area at the sample plane. The pulsed green laser for fluorescence spectroscopy (70 ps, λ=532 nm: light green line) is overlapped with the other two lasers. The fluorescence (orange line) is collected with Obj1 for detection with two avalanche photo diodes (APDs) in a Hanbury-Brown and Twiss (HBT) configuration and with Obj2 for spectroscopy and fast tracking with an electron-multiplying charge coupled device (EMCCD).

Fig. 2.1 sketches the optical setup we developed combining spatial manipulation of a single ND and optical read out of several observables of the NV centre.

A NIR laser[1] (λ = 1064 nm, shown in red) to trap the NDs, a CW green

---

[1] Ventus IR 1064 1.5W

laser[2] ($\lambda = 532$ nm, shown in dark green) for exciting the NV centre and a third ps-pulsed green laser[3] ($\lambda = 532$ nm, shown in light green) for measuring the lifetime of the emitter are all focused to the same point at the sample plane. Fig. 2.2 and 2.3 display two pictures of the actual setup and show the experimental implementation of the sketch in Fig. 2.1.

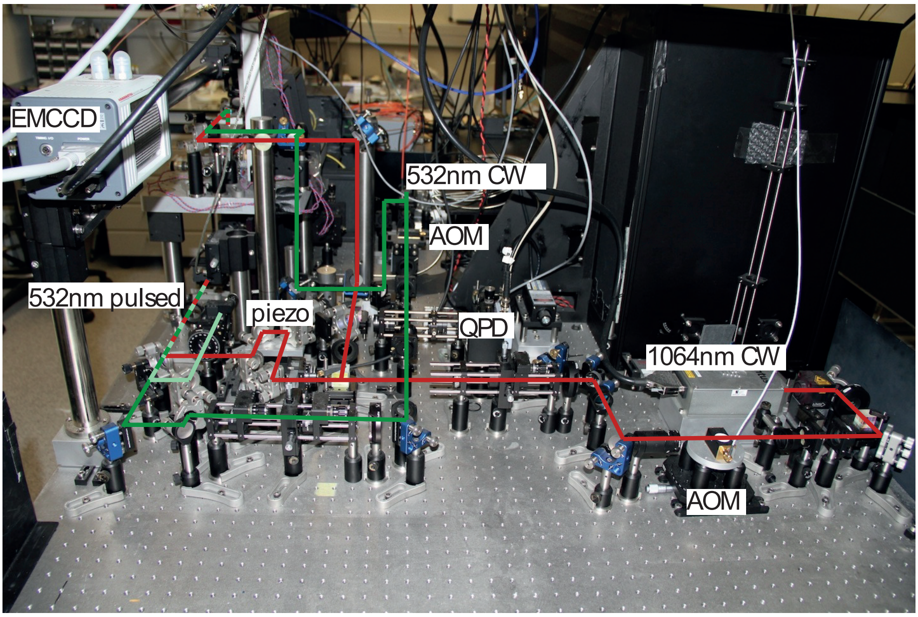

Figure 2.2: **Overview of the optical setup** showing three different laser sources and their respective optical path.

Three dimensional sample positioning The liquid chamber containing a diluted solution of NDs is mounted on a Printed Circuit Board (PCB) that is connected to the microwave generator to perform spin manipulation experiments (section 2.3). The board is mechanically connected to a Piezo cube, which permits nanometer positioning in all three dimensions. Further detail of the liquid chamber fabrication is given in 2.4.3.

---

[2] Ventus VIS 532 250mW
[3] PicoQuant LDH-FH Series

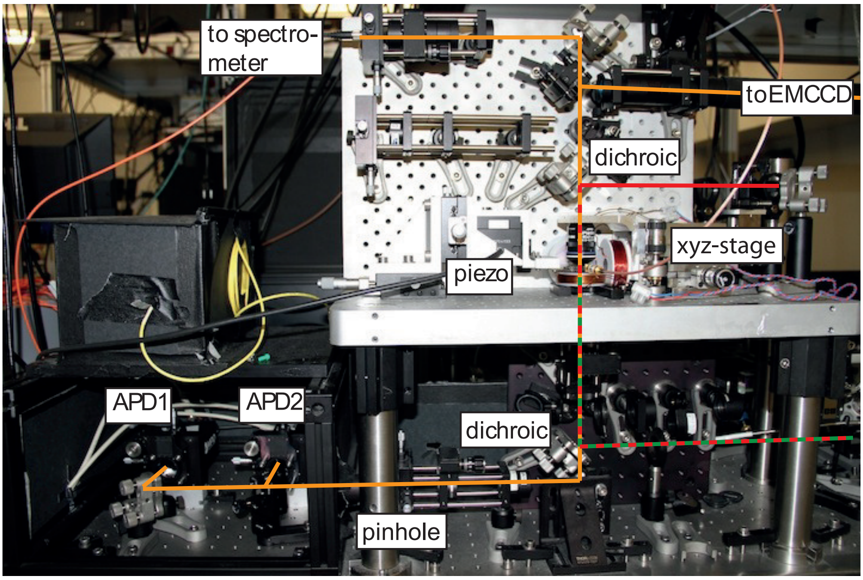

Figure 2.3: **Sample holder and detection paths.** The sample is placed horizontally on a support that is connected to a 3D piezoelectric scanner. The green and red lines correspond to the 532 nm and 1064 nm laser beams, respectively (Fig. 2.1) and the orange path correspond to the fluorescence of the NV centres that is separated from the laser sources with dichroic mirrors. The fluorescence can be collected either from above to image the fluorescence in real time using an EMCCD camera and to measure a spectrum of the NV centre fluorescence (section 2.2.1) or from below to measure fluorescence lifetime (section 2.2.2) and second order correlation (section 2.2.3) using APDs.

2.2 Fluorescence measurements of single NVs

In this section I present the typical fluorescent measurements that characterize a NV centre. Whereas the NIR laser is used to trap the ND (section 2.4) the visible green laser is used to excite the NV fluorescence. The absorption band of the NV centre is centered around 570 nm, but it can be efficiently excited with a green 532 nm CW laser [22]. It is first focused through an acousto-optic modulator (AOM), controlled by a LabView field-programmable gate array (FPGA) card to be able to switch it on and off. It then passes through a beam expander before being focused through objective 1. A dichroic mirror is reflecting the 532 nm laser beam to the objectives and let pass the emitted fluorescence of the NV centre. Its broadband fluorescence can be detected in this setup by APDs, an EMCCD camera or a spectrometer:

Avalanche Photo Diode (APD) The emitted fluorescence from the NV centre is spatially filtered by a 15 μm pinhole to get rid of fluorescence outside the 1 μm detection volume. Two APDs detect the fluorescence signal (Fig. 2.3) and are connected to both the LabView card as well as a Time-Correlated Single Photon Counting (TCSPC) module.

Electron-multiplying charge-coupled device (EMCCD) At the exit of the green CW laser, a beamsplitter deviates a part of the laser beam, which is focused to the back-aperture of objective 2 to illuminate an area of around 20 μm^2 of the sample plane. The emitted fluorescence of this plane passes through the upper dichroic mirror and is focused with a 600 mm lense to an EMCCD camera. This enables to identify a fluorescent ND in real time, whether it is adsorbed on the coverslip or dispersed in solution.

2.2.1 Fluorescence Spectroscopy

As already mentioned in chapter 1, the fluorescence spectrum of the NV centre is characterized by its ZPL at 637 nm and the phonon sideband extending up to 800 nm [17]. To measure the spectra of a single NV centre, a fiber coupled spectrometer equipped with an Andor CCD camera is integrated in the optical setup (Fig. 2.3 upper left corner). Fig. 2.4 shows a spectrum of the fluorescence of a ND with a single NV centre that enables to nicely resolve the ZPL from the sideband. The ZPL is located at 637 nm and the fluorescence at higher wavelength origins from the phonon side band. At shorter wavelength the fluorescence peaks at around 613 nm, which is attributed to the Raman signal of the diamond [17] as well as the fluorescence of the glass substrate.

For this reason we filter out this part of the fluorescent spectrum for further measurements by adding a long-pass edge filter at 633 nm.

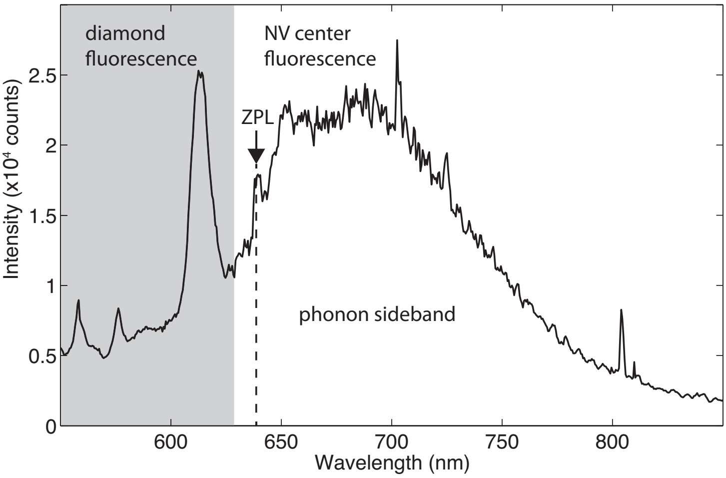

Figure 2.4: **Spectrum of a ND with a single NV centre lying on glass.** The zero phonon line (ZPL) at 637 nm and the phonon sideband at higher wavelength are indicated. In all our fluorescence measurements, we filter the grey region of the spectrum that contains Raman scattering from diamond and fluorescence from the substrate and solution. The integration time was 15 minutes.

2.2.2 Fluorescent lifetime measurements

Another way to identify the NV centre in diamond is based on fluorescent lifetime measurements. As the lifetime of a single electric dipole gives direct insight into the surrounding local density of states (LDOS) near photonic nanostructures [114], the NV centre can act as a LDOS probe as demonstrated in section 3.3.

A pulsed green laser source ($\lambda = 532$ nm) is used to excite the NV centre. The fiber coupled ps-pulsed green laser is superimposed with the CW green laser employing a 50:50 beamsplitter and is focused through the objective 1 (Fig. 2.1). A collimation lens after the fiber can be adjusted to align the focus of laser with the other two lasers.

For the detection of the fluorescence we use an APD that is connected to a TCSPC module. From the laser control a trigger signal starts the counter that registers the events of the APD and puts them into an histogram.

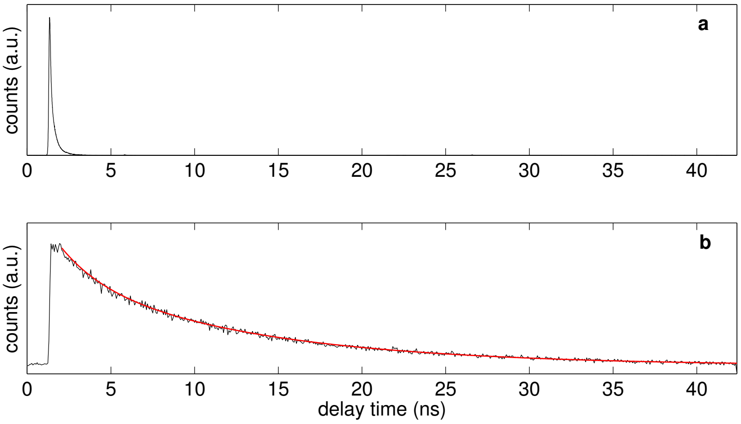

Figure 2.5: **Lifetime measurement with pulsed green light source.** a) Instrument response function using Erythrosin dye. b) Lifetime measurement of a single NV centre in ND (black line). The lifetime of 12 ns for this specific NV is obtained by a two exponential fit (red line).

To measure the instrument response function (IRF) of the system we use Erythrosin that absorbes around 532 nm and has a sub nanosecond lifetime (< 100 ps). To collect the fluorescence we momentously remove the bandpass filter mentioned above. Fig. 2.5a displays the fluorescence response of the pulsed laser measured with Erythrosin. Fig. 2.5b shows the lifetime of a NV centre. A two exponential fit shows that the fluorescence lifetime of the NV centre is around 12 ns. Thus the lifetime can be fitted using an exponential decay without taking into account the IRF for deconvolution. The instant when the detection starts can be adjusted by a delay cable. For this experiment, the delay between the trigger pulse and detection of the pulse is around 1 ns.

For a repetition rate of 5 MHz the typical count rates for the fluorescence of the NV are around $5 - 10 \times 10^3$ counts per second. With this rate the histogram can be acquired in less than 10 seconds in order to further treat it and fit an exponential decay curve to retrieve the fluorescent lifetime of the emitter (section 3.3). The fluorescent lifetime can differ strongly from one ND to another and is centered around 15 ns [115].

2.2.3 Second-order correlation

Spectral and the lifetime measurements allow to determine if a ND hosts NV centres or not. However such measurements do not bring information, whether the fluorescence is from a single or several NV centres.

To identify the quantum character of light, the statistics of the light source have to be studied [116]. To this aim we measure the second-order correlation of the photons emitted, defined by:

$$g^{(2)}(\tau) = \frac{< n_1(t) n_2(t+\tau) >}{< n_1(t) >< n_2(t+\tau) >}, \tag{2.1}$$

with $n_1(t)$ and $n_2(t)$ the counts of detector 1 and 2 respectively [116, 117].

In order to make sure that the fluorescent ND under study only hosts one single NV centre we measure the second-order correlation of its emitting fluorescence using the CW green laser as excitation. This is performed using a Hanbury-Brown Twiss (HBT) setup [118] (Fig. 2.1), where the fluorescence signal is divided by a 50:50 beamsplitter and focused onto two separate APDs, that are connected to a TCSPC module. With this experiment using two detectors, Hanbury-Brown & Twiss identified a way to get a correlation without taking care of the deadtimes or afterpulsing of the detectors. The beamsplitter should be a 50:50 beamsplitter over the emission band of the NV to efficiently acquire a $g^2(\tau)$ histogram. As no beamsplitter is reliably 50:50 over the whole emission band, the counts at each APD are slightly different, which makes the coincidence counting less efficient.

When a photon arrives on APD1 the time counter starts counting until APD2 detects a photon. If another photon arrives first to APD1 again, the counter is reset. The counting module collects all events and groups them into a histogram. A time delay between both APDs is established by putting a 40 m coaxial cable to APD2. If a dip in the histogram is observed at zero time delay ($g^{(2)}(0) < g^{(2)}(\tau)$), the quantum character of light is proven [117]. In theory the number N of emitters can be determined by the depth of the dip $g^{(2)}(0) = N(N-1)/N^2$ [9]. The histogram acquired with the TCSPC module is proportional to the second-order correlation $g^{(2)}(\tau)$, but it also acquires noise from the auto-fluorescence of the substrate and dark counts from the APDs. For this reason the dip usually doesn't go to zero for a single emitter, without data treatment [53, 117]. Here I will present only the non-treated correlation histograms. However if the antibunching dip fulfills $g^{(2)}(0)/g^{(2)}(\infty) < 0.5$ the single photon character is proven and we verify that we deal with one single NV centre in the crystal.

Before measuring the histogram we have to determine the adequate power to excite our quantum system to avoid population of the metastable state [119].

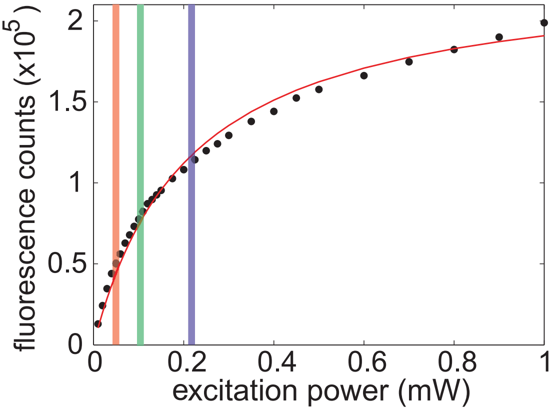

Figure 2.6: **Fluorescence saturation of a single NV centre for increasing excitation power.** With a saturation fit of $A(1-e^{(-P/P_{sat})})+B\cdot P$ we extract the excitation saturation power P_{sat} to be 110 μW with a fluorescence count rate at 7.8×10^4 Hz. The three vertical lines represent the excitation power used for the correlation measurements in Fig. 2.7. The linear behavior at high excitation power P corresponds to the fluorescence rate of the diamond crystal itself.

By measuring the fluorescence intensity as a function of the green excitation power, we observe the characteristic saturation curve for a NV centre [17] shown in Fig. 2.6 with a saturation power of 110 μW. When the saturation power is reached one photon is enough to excite the system and any additional photon from the excitation laser only contributes to the linear increase in fluorescence from the diamond as the system is already in the excited state.

Fig 2.7 shows measured correlation histograms for different excitation power. From the first measurement with low excitation power we can determine that we have a single NV centre since $g^{(2)}(190\text{ ns})/g^{(2)}(0\text{ ns}) \approx 0.3 < 0.5$. With increasing power bunching is observed. This is characteristic for a quantum system with a three level system [117]. For the case of a NV centre the third level is a metastable state, which has a non-radiative decay towards the ground state (Fig. 1.3).

The acquisition time is expected to decrease with increasing excitation power. In the case of 55 μW excitation we have an acquisition time of 280 s at a count rate at each detector of around 2.6 10^4 counts/s (Fig. 2.7a) whereas for 110 μW we obtain Fig. 2.7b in 112 s at a count rate of 4 10^4 and for 220 μW we get the histogram in 58 s as the count rate increased to 5.4 10^4 at each APD. Thus, the quantum nature of the emission and the number of emitters contained in a ND can be obtained in less than a minute at saturation power.

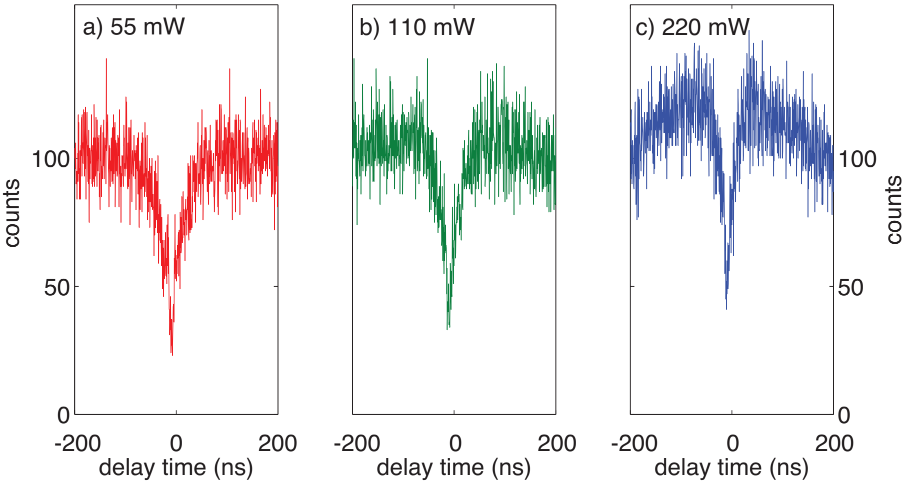

Figure 2.7: **Second order correlation function of a single NV centre for different excitation powers.** a) Below saturation power, antibunching is observed indicating the single photon character of the NV centre. b) At saturation power only slight bunching is observed. c) Driving the NV centre above saturation makes the bunching visible, which indicates the presence of the metastable state of the NV centre [119].

With the correlation, lifetime and spectral measurement I described the main characteristic fluorescence measurements associated to the electric dipole of a NV centre in diamond. In the following section we combine the fluorescence detection with microwave excitation to manipulate and read out its electronic spin.

2.3 Optical Detectable Magnetic Resonance (ODMR) Spectroscopy

As already discussed in section 1.1.2 the electron spin of the NV centre can be initialized and read out optically using the different fluorescence levels due to the inter system crossing (ISC) towards the metastable state [22]. The manipulation of the spin states however is done using microwave (MW) fields, as the two spin levels are separated by around 2.87 GHz [22]. Spin manipulation and read out requires precise timing of the optical excitation and detection as well of the applied MW fields. For this purpose we use a pulse blaster card in combination with a FPGA LabView card.

2.3.1 Electronic architecture

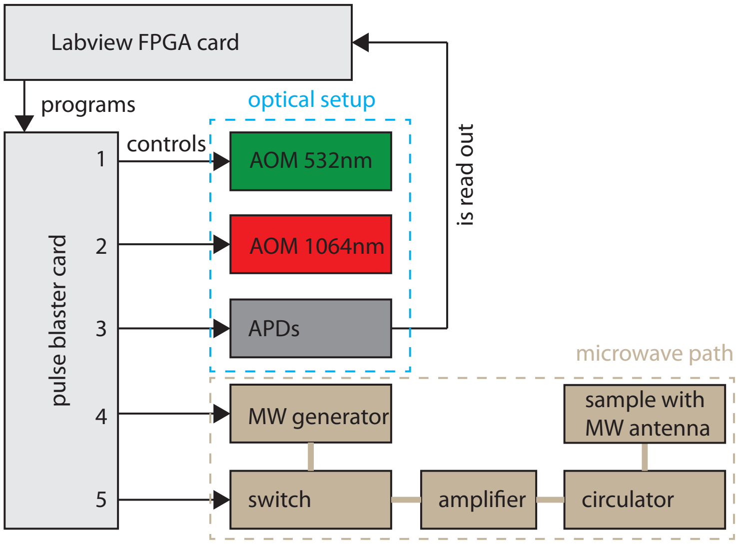

Figure 2.8: **Sketch of the electronic architecture.** The experiment is controlled by a LabView FPGA card. Via an user interface the LabView programs a pulse blaster card that controls with nanosecond accuracy the electronic parts in the optical setup as well as the microwave (MW) generation.

Fig. 2.8 shows a sketch of the electronic architecture assuring the precise timing of the electronic elements in the optical setup as well as the MW generation with nanosecond precision. The pulse blaster card sends a TTL pulse to control the on/off state of the green CW laser as well as the NIR CW laser by switching the respective AOMs. A third channel is connected to the LabView FPGA card for a precise temporal readout of the APD. Channel four and five are used to control the MW fields: channel four sweeps the frequency of the MW generator and channel five controls the on-off state of the MW through a RF switch. After the switch, the MW is amplified by 10 dB and passes a circulator to protect the amplifier from reflections before reaching the MW antenna at the sample. The MW antenna is a 15 μm thick gold wire that is integrated in the liquid chamber. Fig. 2.9 shows the programmed circuit board (PCB) sample holder with the gold wire across the sample. As the gold wire isn't shielded like a coaxial cable it radiates and thus serves like an antenna. An impedance matched 50 Ω resistance terminates the antenna to suppress reflections at the end of the antenna.

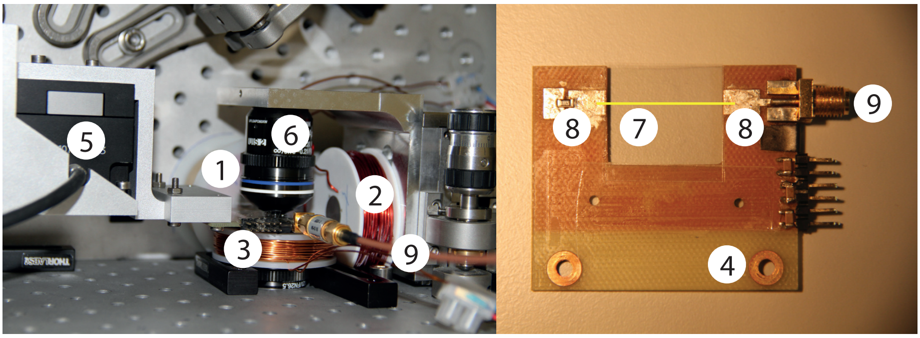

Figure 2.9: **Integration of the RF electronics and magnetic coils around the sample** Three coils are positioned in x y and z to create a vectorial magnetic field (1-3). The sample is mounted on a PCB board that is fixed to a sample holder (4), itself mechanically connected to a xyz piezo stage (5). A bottom and top objective (6) focus the laser beams to a diffraction limited spot in the liquid chamber. A 15 μm gold wire (7) crosses the liquid chamber and is fixed with silver paint to the PCB (8), where it is connected via a RF cable (9) to the MW generator.

2.3.2 Electron Spin Resonance

In this section I detail the pulse blaster sequence used to measure the ESR resonance of the electronic spin as well as the implementation of coils to expose the spin to a static magnetic field.

The actual transition frequency from the $m_s = 0$ ground state to the

$m_s = \pm 1$ ground state is found by sweeping the MW frequency over the expected transition frequency close to 2.87 GHz. The pulse sequence executed by the pulse blaster to acquire an electron spin resonance spectrum is shown in Fig. 2.10. First the system is optically polarized, so that the spin state has high probability to be in $m_s = 0$ state [22]. Then the APD is gated and a reference signal is taken without applying a MW field. After another polarization cycle the fluorescence signal in presence of the MW field is recorded. For the trapping experiment presented in chapter 3 the NIR laser is switched off during the gating of the APD for the fluorescence detection to avoid a drop in fluorescence. Further detail of this fluorescence drop is discussed in section 3.1 and chapter 5. The sequence is averaged for 667 times for one frequency before going to the next frequency step.

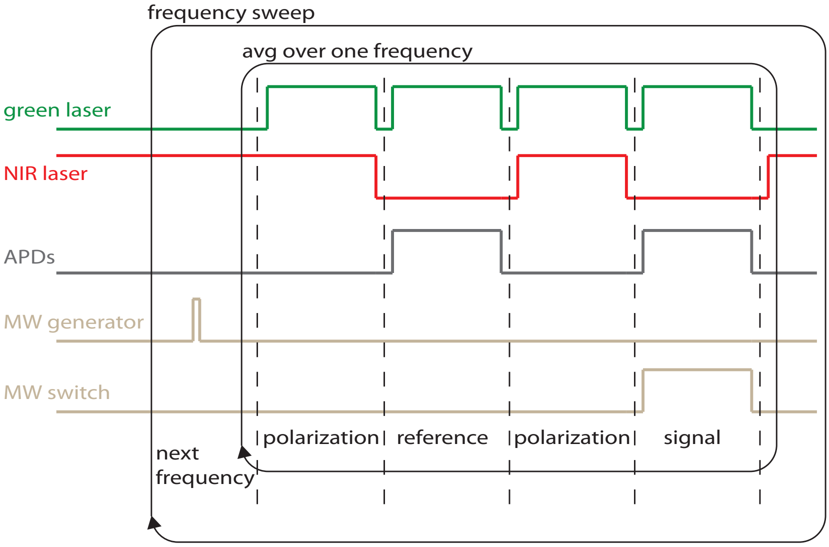

Figure 2.10: **Scheme of the pulse blaster sequence to perform ODMR experiments on a trapped NV centre.** The green laser, the NIR laser, the APDs and the MW switch are gated for each MW frequency. The MW generator is triggered to sweep to the next frequency.

Magnetometry In chapter 3 we use the magnetic sensitivity of a single NV centre to determine the orientation of the trapped NV. For this purpose we need to generate a constant magnetic field with contributions in x,y and z direction. We use three coils that create a magnetic field when a current is set. The coils are placed in close proximity to the objectives to create at their focus a magnetic field of a few mT (Fig. 2.9). A Hall probe is used to calibrate the magnetic field contribution of each coil in x,y and z. In the LabView program we implement a direct transformation matrix from the current applied to the produced magnetic field in space.

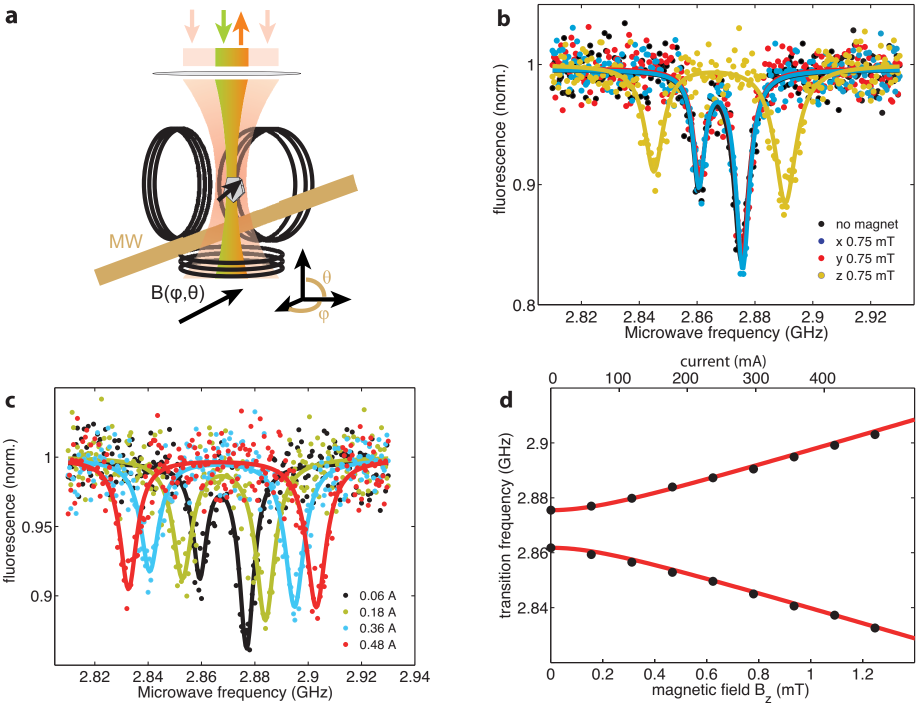

Figure 2.11: **Calibration of the coils for magnetic field measurements.** a) Sketch of the coils generating a vectorial magnetic field acting on the NV. b) ESR measurements performed on a single NV having its NV axis along z. Only the projection of a magnetic field along the z-axis produces a Zeeman shift of the $m_s = \pm 1$ sublevels. c) ESR measurement performed on the same NV centre for different currents through the z-coil. d) Fit of the Zeeman frequency splitting in a low magnetic field to retrieve the conversion coefficient of current to magnetic field.

The coil calibration can be verified using the NV centres to detect the produced magnetic field, if one NV center is pointing in the direction of one of the axis:

Due to the Zeeman splitting the transition frequency of the $m_s = \pm 1$ state shifts, which can be observed in the ESR spectrum. The Hamiltonian for a NV centre is given by [71]

$$\mathcal{H} = hDS_z^2 + hE(S_x^2 - S_y^2) + \hbar\gamma_e \mathbf{B}\mathbf{S} \tag{2.2}$$

where h is the Planck constant, D and E are axial and transverse zero-field splitting (ZFS) parameters, respectively, z is the NV defect spin quantization axis, γ_e is the electron gyromagnetic ratio, and **B** is the local magnetic field applied to the NV electron spin **S**. Only projections of the magnetic field along the NV electron spin axis are contributing. The ZFS E is supposed to be zero in bulk diamond, but can have non-zero values in NDs, due to strain inside the diamond lattice [82]. This is generally observed with the ND we use.

We select an ESR transition that only changes applying a magnetic field in one direction (Fig. 2.11b). We then check the calibration of the magnetic field generated by the coils tracking the Zeeman splitting measured with the ESR (Fig. 2.11c, d). For magnetic fields smaller than 10 mT (i.e. $hD >> \hbar\gamma_e B_z$) the quantization axis is the NV axis and after diagonalization of the Hamiltonian the ESR frequencies are obtained [71]

$$\nu_{\pm} = D \pm \sqrt{E^2 + (\frac{\gamma_e B_z}{2\pi})^2} \tag{2.3}$$

The actual frequency transitions for a given coil current can then be fitted to formula 2.3 to retrieve the coefficient for the current to magnetic field conversion. The conversion coefficients for our coils are (xx,yy,zz)=(0.46,0.65,0.38) A/mT. These conversion coefficients verify the measurements performed with the Hall probe.

2.3.3 Spin manipulation techniques

Once the spin transition frequency that flips the spin from the $m_s = 0$ state to the $m_s = \pm 1$ state or vice verse is determined, the spin can be directly addressed and thus be manipulated using the MW transition frequency.

Rabi oscillation

To perform spin manipulation experiments it is crucial to know the parameters for the so-called π pulse to flip the spin by an angle of 180 degree in the Bloch sphere (e.g. changing populations of the $m_S = 0 \leftrightarrow m_S = \pm 1$ sublevels) or to bring the spin in a superposition state by applying a $\frac{\pi}{2}$ pulse [22].

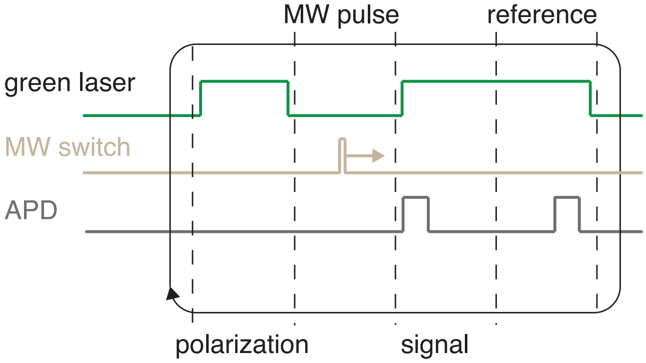

Figure 2.12: **Pulse blaster sequence for Rabi oscillation measurement.** The system is first polarized by a 2 μs green laser pulse. Then the MW is applied and the APD reads out the fluorescence. The duration of the MW pulse is increased from 10 ns to 2010 ns in 400 steps and the overall averaging is 50000 times. The second reading of the APD is a reference to compare the signal, as sometimes oscillations don't origin from the Rabi oscillations itself but from setup problems.

The parameters defining a π pulse are the power and the time duration of the MW pulse. Fixing the MW frequency at a certain power and increasing the duration of the pulse results in an oscillation of the population of the different ground states and thus in an oscillation of the fluorescence signal, known as Rabi-oscillation. The pulse scheme for the pulse blaster is shown in Fig. 2.12 and a typical Rabi-oscillation for different MW powers is shown in Fig. 2.13. First the system is again initialized to the $m_s = 0$ sublevel by applying a pulse of the green laser. Then the MW is applied and the fluorescence is read out. The MW pulse duration is sweeped from 10 ns to 2010 ns in 400 steps. When the pulse has the area (power × duration) that matches a π pulse, the system ends up in the $m_s = \pm 1$ sublevel, which goes with a maximum drop in fluorescence originating from ISC to the metastable state [22]. After a 2π pulse the system again ends up in the original $m_s = 0$ state.

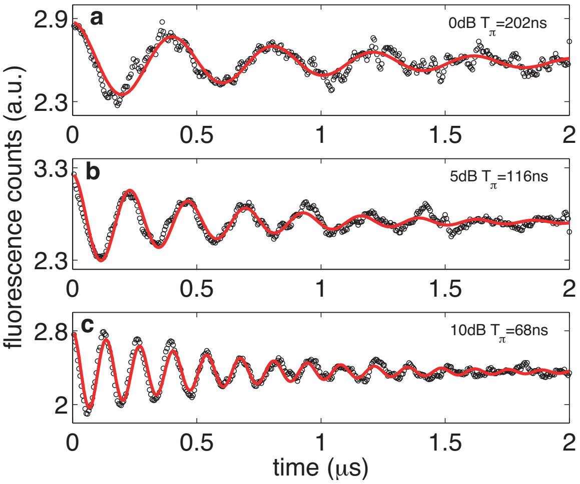

Figure 2.13: **Rabi oscillations of a single NV centre.** The microwave frequency is set at the transition frequency of the $m_s = 0 \leftrightarrow m_s = \pm 1$ sublevel. The pulse duration of the microwave is increased while the power is fixed. Oscillations in fluorescence monitor the transitions of the sublevels. The measurement is fitted with a damped cosine function. Resulting π pulse width is 202 ns for 0 dB in a) to 68 ns for 10 dB in c).

In practice decoherence through a nuclear spin bath of ^{13}C and nitrogen impurities limits the number of oscillations. This damping of the oscillation can be understood measuring the dephasing time with an echo experiment.

Hahn echo

Damping in the Rabi oscillation is due to two reasons: First the population decay (characteristic timescale T_1) results from Raman interaction with lattice phonons at room temperature [100]. Second the spin-spin decoherence time T_2^* resulting from interaction between the electron spin and an adjacent nuclear spin bath from ^{13}C or additional N atoms [100]. As their spins create a non-zero magnetic field, this field interacts with the electron of the NV. The spin coherence time defines how long the spin is coherent enough to perform spin manipulations. As the spin-lattice decoherence takes place on a much longer time scale we are only limited by the spin-spin decoherence time ($T_1 >> T_2 >> T_2^*$) [100]. Wheras the T_2^* time refers to a reversible dephasing effect, with a Hahn echo we can only measure the irreversible T_2 decoherence of the spin-spin coupling [120, 100].

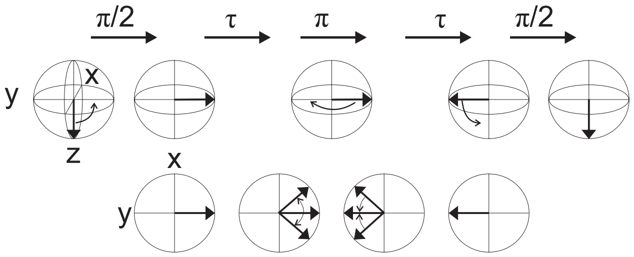

Figure 2.14: **Echo sequence on the Bloch sphere.** First row: Bloch sphere. Second row: xy-plane of Bloch sphere. The spin is brought by a $\pi/2$ pulse in a superposition state of the two groundstates (xy-plane). It develops for a waiting time τ and dephases due to fluctuations in the surrounding spin bath. A π pulse inverts the spin by 180 degree and after a second waiting time τ the dephasing is inverted and an echo of the original spin is established. An additional $\pi/2$ pulse converts the echo phenomena into populations for measurement.

The Hahn echo sequence ($\frac{\pi}{2} - \tau - \pi - \tau$) consists of $\frac{\pi}{2}$ and π microwave pulses and waiting times τ (Fig 2.14). As we monitor the spin optically, a $\frac{\pi}{2}$ pulse has to be added to convert the spin echo phenomena into populations [22]. The obtained measurement can be fitted with an exponential decay $exp(-\frac{2\tau}{T_2})^2$ [105], which gives us a value for the spin-spin decoherence time T_2 (Fig. 2.15).

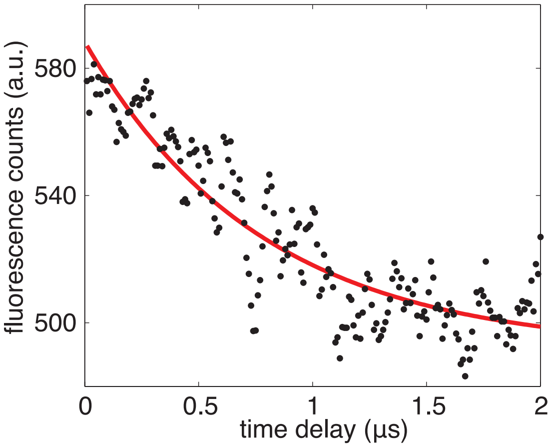

Figure 2.15: **Hahn echo measurement:** Fluorescence dependence with the delay time τ between pulses. An exponential fit gives the spin-spin decoherence time of $T_2 = 1.55 \mu s$

With the developed setup we are able to detect and read out optically the spin state of a single NV centre and manipulate it with MW fields. Thus we are able to measure magnetic fields using the electron spin of the defect centre. However spin-decoherence measurements show very low T_2 times compared to bulk diamond T_2 values [41], which limit our magnetic sensitivity (section 3.2.3).

2.4 Optical trapping

One of the main originalites in this thesis is to manipulate a ND hosting a single NV centre by means of optical tweezers (chapter 3). This section gives a short description of our trapping platform, the particle detection used in the experiment and an approach to trap a single ND for several hours.

2.4.1 Principles of optical trapping

Optical tweezers have shown to be a very efficient tool to manipulate different kinds of micro-size objects ranging from colloids, droplets to living cells. They are usually implemented along the optical path of an optical microscope, using a high numerical aperture objective to focus the laser beam to a diffraction limited spot. A small object located nearby the laser focus experiences two force contributions: the scattering force (or radiation pressure) and the gradient force.

The scattering force is a repulsive force pointing along the incident k-vector and can be written for a particle with radius $a << \lambda$ as [121]:

$$F_{scatt} \propto \frac{\alpha^2}{c n_m \lambda^4} I_0 \tag{2.4}$$

with α the polarizability, c the speed of light in vacuum, n_m the refractive index of the medium, I_0 the intensity and λ the wavelength of the trapping laser. The gradient force, originating from the gradient of the electromagnetic field intensity, tends to pull it towards stronger intensity regions [121]:

$$F_{grad} \propto \frac{\alpha}{c n_m^2} \nabla I_0 \tag{2.5}$$

The object gets stably trapped when the intensity profile at the laser focus enables the gradient force to dominate both scattering forces and Brownian motion. The total force magnitude depends on the trap profile and the polarizability of the specimen

$$\alpha = n_m^2 a^3 \frac{m^2 - 1}{m^2 + 2} \tag{2.6}$$

of the object, determined by its radius a and the dielectric function contrast $m = n_p/n_m$ between the surrounding medium (refractive index n_m) and the particle (refractive index n_p). In this thesis we are interested to trap nanometer-sized ND in a water environment. As the refractive index of diamond ($n_p = 2.39$) is large compared to the one of water ($n_m = 1.32$) at $\lambda = 1064$ nm, nano-sized ND sill have a polarizability large enough to be trapped.

The choice of trapping sources follows several criteria [121]: the stability of the laser, the output power of the laser, wavelength mode quality, transparency of the medium, etc. A 1064 nm laser provides a very good mode quality, is very stable regarding power fluctuations and is available at different output powers for a reasonable price. The wavelength is still in the transparency window of water and is furthermore in the transparency window for biological samples, which might be beneficial for further experiments.

NIR trapping laser The NIR laser is focused through an AOM which is controlled by the Labview FPGA card. The first order of the laser beam passes through a beam expander whereas the zero order is blocked. Thus the AOM serves as a beam shutter that allows to switch the beam on and off in less than 100 ns. A polarizing beamsplitter (PBS) then divides the beam in two parts. One beam that is focused through the lower fixed high NA objective 1 and the second beam that goes through the above high NA objective 2, mounted on a xyz-stage shown in Fig. 2.3. The implementation of a counter-propagating beam cancels the scattering force and therefore results in a higher confinement in z. The beam intensity in both arms can be controlled with a $\lambda/2$ plate in front of the PBS. In one of the beam paths a piezo motor is integrated to control the phase between the two beams (Fig. 2.1, 2.2).

To make sure that the trapped particle is excited with the green laser at the same position as it is trapped with the NIR laser, the green laser is corrected for the achromatism of the objective. The NIR laser beam has to be collimated and overfills the back-aperture of the objective for efficient trapping. Therefore one lens of the beam expander for the green laser is mounted on a z-stage to diverge the beam and thus adjust the focus of the beam at the sample plane. This is done using fluorescent molecules that can be easily excited with one and two photon absorption (532 nm and 1064 nm). This alignment can also be performed using the drop in the NV fluorescence in presence of the NIR laser (chapter 5).

2.4.2 Particle detection

The lateral confinement of the particle in the optical trap is assessed by standard position detection of the particle. We use a back focal plane detection that relies on the interference between the forward scattered light from the ND in the trap and the unscattered light from the trapping laser. The interference signal is detected with a standard Quadrant Photo Diode (QPD) [121, 122]. The detector consists of four quadrants that are summed pairwise and give differential signals for both x and y dimensions. Out of the detected time trace we can generate a histogram for the particle movement inside the trap. Fourier-transformation of the time trace results in a power spectrum (Fig. 2.16a). However, the detector

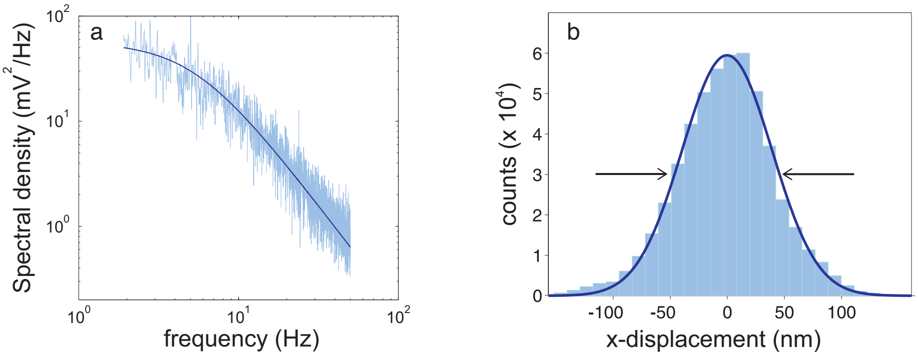

Figure 2.16: **Position measurement with QPD for one direction.** a) Power spectrum of the trapped particle and its lorentzian fit with a cut-off frequency of 5.7 Hz. b) Histogram of the particle movement in the trap with calibrated nm scale.

signal measures the uncalibrated power spectrum

$$P_{exp}(f) = \frac{D_{exp}}{f_c^2 + f^2} \tag{2.7}$$

with f_c the cut off frequency and D_{exp} a constant. This is related to the true power spectrum

$$P(f) = \frac{k_B T}{\pi^2 \gamma (f_c^2 + f^2)} \tag{2.8}$$

by $P_{exp}(f) = \rho^2 P$, where ρ represents the linear sensitivity of the detector (in volts/unit distance) [121]. By fitting the experimental power spectrum with equation 2.7 and compare D_{exp} to the theoretical diffusion coefficient $D = k_B T/\gamma$ with $\gamma = 6\pi\nu a$ the hydrodynamic drag coefficient on a sphere with radius a in a medium with viscosity ν, we get the units in nm [121]. Finally, the cut-off frequency f_c of the power spectrum is related to the stiffness κ of the trap via [121]

$$f_c = \frac{\kappa}{2\pi\gamma} \tag{2.9}$$

Fig. 2.16 shows the fitted power spectrum of a 70 nm trapped ND and the histogram of the particle deplacement measured with a QPD. The ND was trapped in a 4:1 glycerol water mixture with a viscosity of $\nu = 7.7$mPa s [4] to

---

[4] *www.met.reading.ac.uk/sws04cdw/viscosity_calc.html*

slow down the Brownian motion and to avoid to have several particles in the trap. The resulted stiffness of the trap is $\kappa = 183$ pN/μm (equation 2.9), which allows us to move the ND over distances up to 100 μm without loosing it.

For further confinement along the z axis, the scattering force is canceled out by trapping a particle with two counter-propagating beams [123]. As the deplacement detection in z is not accurately accessible with the QPD, we modeled the optical potential of a counter-propagating beam. In Fig. 2.17 the optical trapping potential for a spherical 70 nm diamond particle is calculated[5]. We find a lateral confinement of 71 nm and a confinement of 38 nm along the beam propagation axis Z. This demonstrates the Z confinement to be smaller than the lateral confinement that is still dependent on the laser intensity.

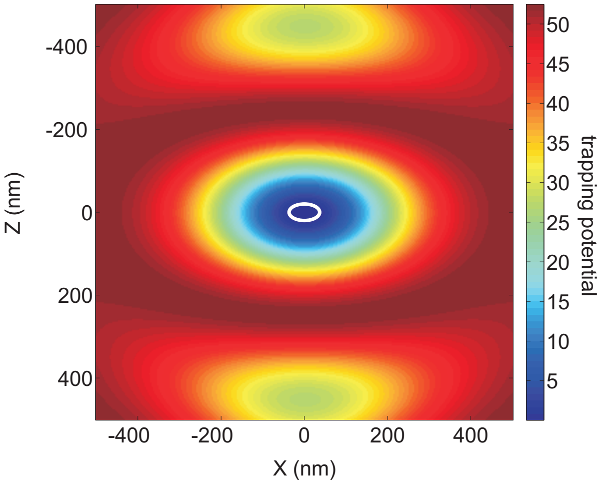

Figure 2.17: **Optical trapping potential for a characteristic 70 nm diamond particle.** The particle is assumed to be spherical. The potential is plotted in units of kT (color scale, for T=300 K). The region likely occupied by the particle (potential<kT) is limited by a white elliptical contour. Each of the two Gaussian, linearly polarized, counter-propagating beams defining the trapping well has a power of 50 mW. The NA is 1.2 for both of them. The refractive indices of the diamond and the fluid are 2.39 and 1.46, respectively, at the optical wavelength of 1064 nm. We describe the response of the particle in the electrostatic limit, so that the potential is simply given by $-\alpha|E(r)|^2$, where α is the particle polarizability and E(r) is the trapping field at position r [124].

---

[5] using a code developed by J. F. Garcia de Abajo

2.4.3 Single NV trapping

As already discussed earlier, we aim at manipulating a single NV centre, which results that we only want to trap one single ND. I.e. the ND should not cluster and once trapped one ND, another ND should not jump into the trap. For manipulation with optical tweezers the concentration of the NDs in a water solution is therefore critical.

Nanodiamond preparation. [6] The ND sample (Microdiamant, MSY 0-0.1 m) was refluxed for 6 days at 90° in a 9:1 ratio of concentrated sulphuric to nitric acids. The NDs were collected by centrifugation and ultrasonicated using a tip probe sonotrode (Branson, 101-063-346) for 1 hour before being additionally refluxed under the previous conditions. The NDs were then washed with deionised water and ultrasonicated in 0.1 M sodium hydroxide for 1 hour, rinsed with water and re-ultrasonicated in 0.1 M hydrochloric acid. The sample was rinsed and resuspended in deionised water. Finally, several centrifugation steps were used to size select the required ND particles and Dynamic Light Scattering (DLS) [7] measurements were used to determine the size distribution of the particle to be 74±15 nm.

Solution preparation The ND water solution is sonicated for two hours in a ultrasonic bath to break possible clusters that could have been formed. Furthermore the solution is filtered with a centrifuge filter for five minutes at 18 krps to filter out remaining big clusters. The actual size distribution is verified with a DLS device. A droplet of the solution is finally placed between two 170 μm thick cover slips that are sealed by a thin layer of vacuum grease at the border of the cover slips. The final thickness of the liquid chamber varies between 30 μm and 50 μm. The 15 μm gold wire for MW manipulation passes inside the chamber.

---

[6] This step was performed by J. Say from Macquire Univeristy Sydney

[7] Malvern Instruments Zetasizer NS

Multiple particle trapping was one main challenge to overcome for this experiment. If the solution is too dense, there is a lot of NDs with NV centres, but the possibility to trap several NDs is high. For a very diluted solution however it takes too long to trap a ND with a single NV centre. To prevent that several NDs are in the optical trap we investigate two approaches:

Choice of the host medium Using a viscous medium slows down the Brownian motion of the particles inside the solution. Nevertheless the viscous medium should not be auto-fluorescent upon green laser illumination and should be solvable with another less viscous medium to be able to adjust the viscosity. I tried several viscous media, such as immersion oils, refractive matching liquids, Agar (used to immobilize biological samples) and glycerol. The only medium that did not auto-fluoresce and that could be solved in water was glycerol. The diffusivity $D = k_B T / 6\pi\eta r$ with η the dynamic viscosity and r the radius of the particle drops by a factor of 85 from a pure water solution compared to a 4:1 glycerol water mixture. In a proper diluted solution this makes it very unlikely that two particles are trapped consequently during the time of the experiment. Additionally the decrease of diffusion makes it possible to image the diffusing fluorescent NDs with the EMCCD camera in real time.

Optical ring beam Using an axicon lens, a ring beam can be created for the NIR laser with a diameter of $d = 2ltan[(n-1)\alpha]$ with l the distance of the image plane, n the refractive index of the axicon and α its opening angle. This ring beam can be imaged to the focal plane of the objective by choosing the right lenses[8]. Fig. 2.18 shows the beam path and the final beam shape in the focus of the objective imaged with a CCD camera. Once a particle is trapped, the axicon beam is switched on to protect the particle in the trap. The scattering force of the ring beam prevents that a second particle comes close to the trap, but is scattered away instead. The advantage of this method is that this works in a water only solution, for experiments where a low viscosity is needed. Unfortunately, in this case it is not possible to track the fluorescent ND with the EMCCD camera in real time. For this reason in the following chapter we use the viscous medium to be able to track the ND.

---

[8] using Zemax software for optimization

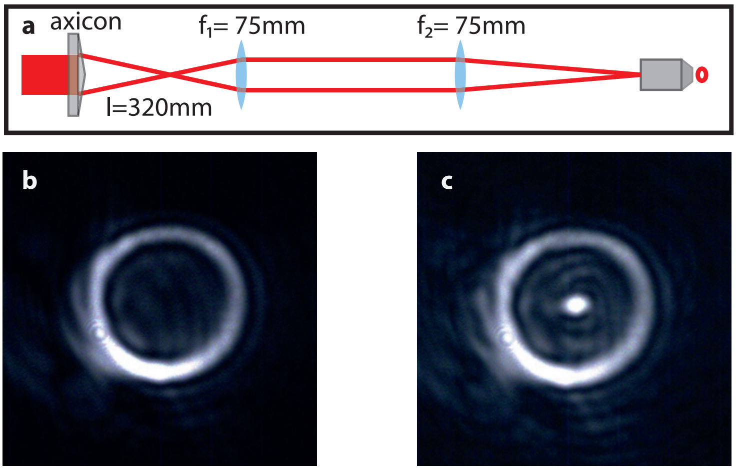

Figure 2.18: Optical ring beam. a) An axicon creates a ring beam that is imaged to the focal plane of the objective. b) Ring beam at the focal plane imaged with a CCD camera. c) Ring beam and trapping beam imaged with a CCD camera.

With the described experimental setup we now have everything to optically trap a single ND, characterize the NV fluorescence and manipulate the spin by means of MW radiation, which is detailed in the next chapter.

3

Three dimensional optical manipulation of a single electron spin

Nitrogen vacancy (NV) centres in diamond are promising elemental blocks for quantum optics [125, 56], spin-based quantum information processing [126, 127], and high-sensitivity sensing [67, 49, 69, 42, 71, 50, 74]. NV centres can be found in bulk diamond as well as in nanodiamonds (NDs). Particularly, the nanometer size of the ND makes them well suited for coupling to photonic or plasmonic structures. However, fully exploiting the capabilities of these NV centres requires suitable strategies to accurately manipulate them.

In this chapter, we use the setup presented in chapter 2 and experimentally demonstrate 3D optical manipulation of individual NDs hosting a single NV centre. We actively select a single ND that is diffusing in liquid. Once trapped, we achieve a high level of control of the spin position is achieved along the three spatial axes with nanoscale resolution (section 3.1). Remarkably, the orientation of the trapped NV remains nearly fixed over time and can be accurately controlled, which allows the implementation of coherent manipulation of a single NV spin and vectorial magnetometry (section 3.2). Finally, in section 3.3, we illustrate that the trapped NV can be raster scanned above a patterned surface to map its lifetime. This provides direct insights into the electromagnetic LDOS near an integrated channel waveguide.

3.1 Optical manipulation of single nanodiamonds

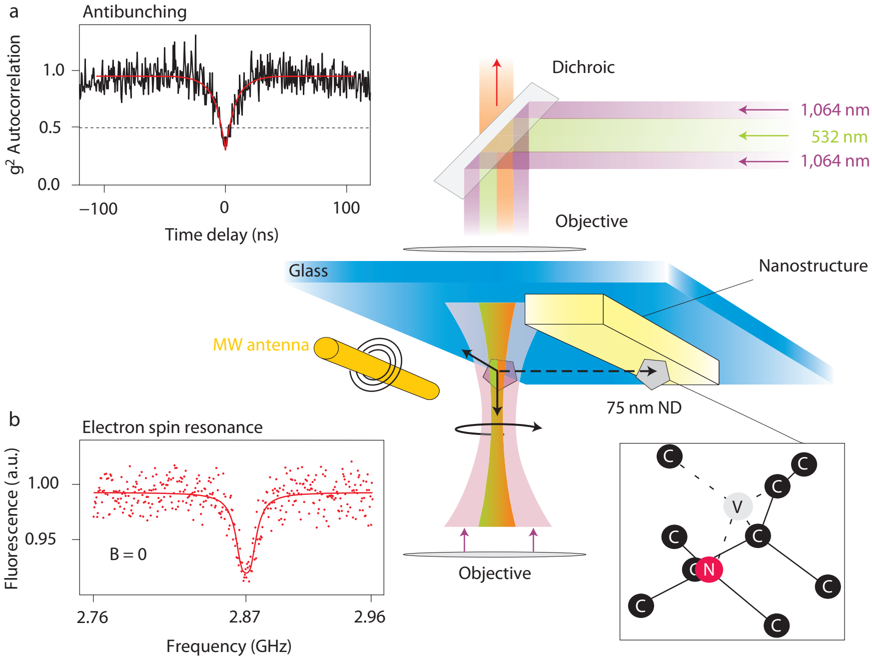

Figure 3.1: **3D Optical trapping and manipulation of a single electron spin.** A near-IR laser (λ=1064 nm, shown in light red in the central sketch) is focused through two high-NA objectives to trap a ND containing a single NV centre. A superimposed 532 nm laser (shown in green) excites the NV. The emitted photoluminescence (orange) passes a dichroic filter and is detected with two APDs. The central schematic shows the basic elements of our experiment. a) Correlation measurements of a trapped ND confirming the single-photon character of the NV luminescence ($g^{(2)}(0) < \frac{1}{2}$). The red line is an exponential fit with a decay of 18 ns. b) Optically detected magnetic resonance measurement of a single NV centre.

The NDs used in this experiments[1] have diameters around 75 nm and are dispersed in a 5:1 glycerol/water mix (refractive index $n = 1.46$) confined in a static fluidic chamber. Due to the small size of the ND the stability of the trap

---

[1] provided by Jana Say and Louise Brown from Macquarie University Sydney

is enhanced by canceling out the scattering forces and producing constructive interference along the optical axis (Fig. 2.17), as shown in section 2.4.2. This is achieved by tightly focusing (NA = 1.2) to the same point two equally intense and collinearly polarized counter-propagating beams (45 mW per beam) from a Nd:YAG (λ = 1064 nm) laser (Fig. 3.1 and 2.1). This strategy enables us to trap and manipulate a single ND ($n = 2.391$) as small as 50 nm in all three spatial directions.

To deterministically trap an individual ND containing a single NV centre, we use a highly sensitive EMCCD camera (section 2.2) in fluorescence imaging mode to follow the diffusion of the NDs in real time (Fig. 3.2a). We immobilize the fluorescent ND of interest by bringing it close to the focus of the dual-beam trap moving the sample with the piezo stage.

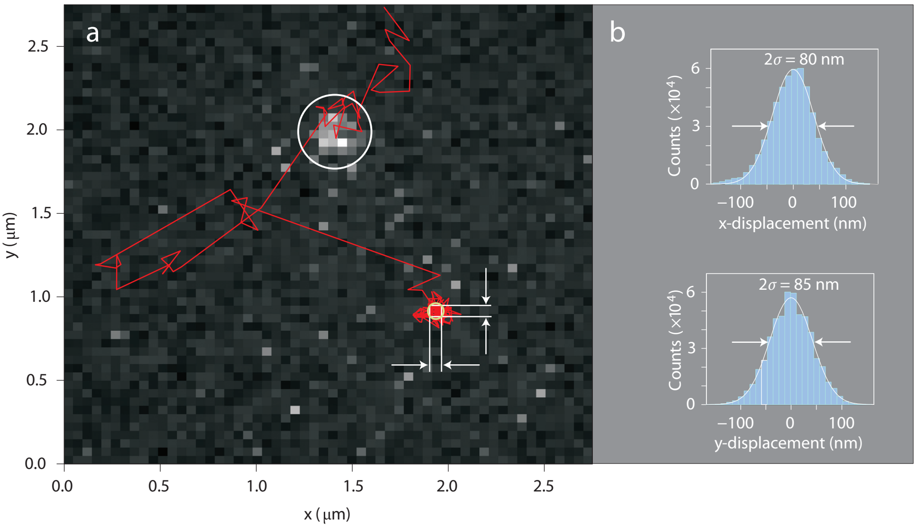

Figure 3.2: **Tracking and trapping of a single ND with a single NV-center.** a) EM-CCD image of a fluorescent nanodiamond (white circle) and its position trace (red line). Tracking the fluorescence makes it possible to direct the nanodiamond with the XYZ piezoscanner close to the trap, where it is captured and confined. b) Position histograms of the time trace of the trapped ND retrieved from position tracking with a quadrant photo diode [121]. The solid blue lines are Gaussian fits to the position histograms. The standard deviation is 40 nm. The particle is confined within less than 80 nm during 70% of the time.

Trap characterization.

Using standard position measurements based on a QPD [121] (section 2.4.2), we were able to retrieve the position histogram of the trapped ND along each of the two directions (x and y) perpendicular to the optical axis. The full-width at half-maximum FWHM of the Gaussian distribution was of the order of 80 nm along both directions (Fig. 3.2b). Because position detection is known to lack accuracy for determining the trap confinement in the z direction, an estimate based on the spatial confinement of the interference fringes is provided through simulation in section 2.4.2 (Fig 2.17). Assuming that the ND remains localized in one fringe at the focus, we expect its confinement in the z-direction (along the beams) to be smaller than 50 nm. The trap stiffness achieved is such that the ND can be moved in the chamber over distances as large as 100 μm with velocities up to 10 μm/s.

Modulation of the trap beam

Subsequently, we superimpose the green laser onto the NIR beam and focus it to the same spot at which the ND is trapped. It excites the NV centre and the fluorescence is detected with the APDs. We observe a lower fluorescence count rate for trapped NV centres compared to adsorbed ones. We identified the NIR laser to be responsible for the decrease in fluorescence that was limiting our signal over noise. To overcome this issue we implemented a modulation of the trap beam gated by an AOM. The APD is triggered to read the fluorescence counts for 5 μs when the NIR laser beam is off. Then the NIR laser is switched on for 5 μs meanwhile the APD is off. This modulation of the trapping beam does not drastically perturb the trapping efficiency, since diffusion times in our viscous medium are much lower than the switching times of the beam. Applying this technique, we could perform all fluorescence measurements, namely second order correlation, lifetime and ESR on a trapped NV centre. Further study enabled us to identify the origin of this quenching, which is presented in chapter 5.

To verify that a trapped ND only hosts a single NV centre, we perform coincidence measurements using HBT detection (section 2.2.3). Figure 3.1a shows measured antibunching below the threshold of 0.5, proving that the trapped ND contains a single NV centre.

3.2 Optical Detected Magnetic Resonance on optically trapped NVs

We have shown that we can trap single NDs hosting a single NV centre. We first aim at using the single electronic spin as a mobile magnetic probe. The electronic spin is sensitive to an external magnetic field through the Zeeman effect. The Zeeman effect is directly related to the projection of the magnetic field along the spin axis that is fixed inside the ND. To this end a crucial requirement is the stability of the NV axis (that is, the spin quantization axis) inside the trap.

3.2.1 Determination of the NV axis orientation

Conventional trap characterization methods do not give direct information about the rotation of the particle inside the trap. Given that the trapped particle is not a conventional particle, but has a single electron spin, which axis is fixed inside the crystal, the stability of the crystal can be assessed by means of optically detected ESR measurements (Fig. 3.3).

To this end, the ND is positioned in the vicinity of a gold wire microwave antenna, which was integrated into the chamber and connected to a microwave generator (section 2.3.2). The ESR spectrum is obtained by monitoring the NV fluorescence while scanning the microwave frequency over the $m_s = 0 \leftrightarrow m_s = \pm 1$ transition at 2.87 GHz. The Hamiltonian of the electron spin reads (section 2.3.2)

$$\mathcal{H} = hDS_z^2 + hE(S_x^2 - S_y^2) + \hbar\gamma_e \mathbf{BS}. \tag{3.1}$$

Without external magnetic field (B = 0) and without internal strain (E = 0), the $m_s = \pm 1$ states are degenerate, leading to a single dip in the ESR spectrum[2], as shown in Fig. 3.3a. In contrast, when we apply an external magnetic field, its vector projection along the intrinsic magnetic dipole of the NV induces Zeeman splitting of the $m_s = \pm 1$ states. Consequently, the orientation and stability of the NV axis can be determined by maximizing the Zeeman splitting induced by a fixed-amplitude (1.5 mT) external magnetic field along each of the three spatial directions (shown in Fig. 3.3b-d).

Comparing the relative splitting Δ for fields along each axis, the contribution of the respective magnetic field is determined as follows: we estimate (for weak external magnetic fields < 10 mT) the polar angles corresponding to the

---

[2] In most of the NDs the $m_s = \pm 1$ state is not degenerate, because of internal strain.

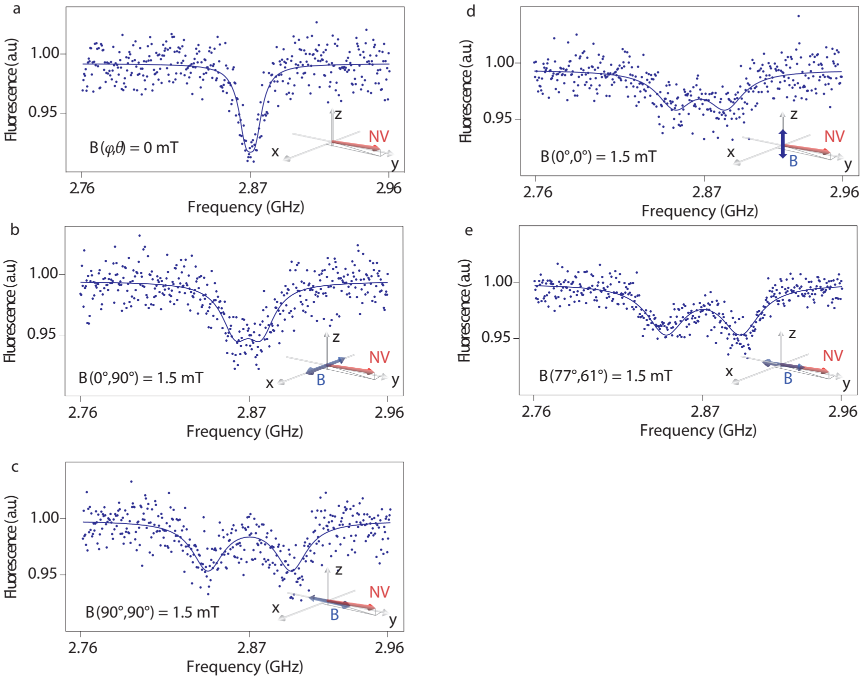

Figure 3.3: **Determination of the NV spin axis orientation.** a)-e) Optically detected electron spin resonance spectra of a trapped ND with a single NV-center (correlation measurement in Fig. 3.1). The datapoints of the frequency sweep were aquired in steps of 0.5 MHz. The solid lines are a two-Lorentzian fit to determine the transition frequency. The insets illustrate the NV-axis and the direction of the magnetic field B. a)-d) Determination of the NV-axis orientation. a) No magnetic field is applied. The $m_s = \pm 1$ ground state is degenerate. b) For the X projection of the magnetic field onto the NV axis only a small Zeeman splitting is visible. c),d) For the Y and Z projection of the magnetic field onto the NV axis already a larger Zeeman splitting is observed. e) When the magnetic field is aligned with the NV axis, a maximal splitting is recorded.

orientation of the NV axis as

$$\phi = atan(\Delta y/\Delta x) \tag{3.2}$$
$$\theta = atan[\Delta x/(\Delta z cos\phi)] \tag{3.3}$$

where $\Delta x = \nu_{1,x} - \nu_{2,x} - E, \Delta y = \nu_{1,y} - \nu_{2,y} - E, \Delta z = \nu_{1,z} - \nu_{2,z} - E$ are the Zeeman splittings produced by magnetic fields along X, Y and Z directions, respectively. In Fig. 3.4 this estimate is compared with the calculated ESR frequencies $\nu = D \pm \sqrt{(\gamma_e B_z/2\pi)^2 + E^2)}$ of the spin Hamiltonian [71] for an adsorbed NV centre. D and E are the zero field splitting parameters, γ_e is the electron gyromagnetic ratio and B_z is the field along the NV axis. We find good agreement between experiment and theory (Fig. 3.4).

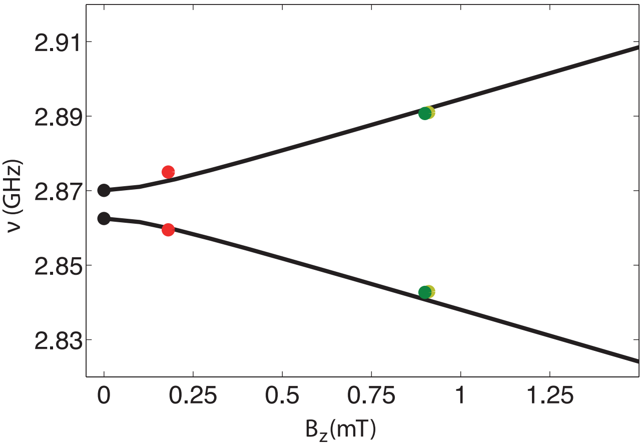

Figure 3.4: **Zeeman splitting as the function of the magnetic field along the NV axis.** The solid lines are calculated from the theoretical model based on the spin Hamiltonian for a field B_z along the NV axis. The circles are experimental data from the ESR frequencies of an adsorbed NV for an external field applied along X, Y and Z and its calculated field projection for $\theta = 45°$ and $\phi = 11°$ onto the NV axis using equations 3.2 and 3.3.

Applying equations 3.2 and 3.3 to the measurements in Fig. 3.3 we determine for this trapped NV the polar coordinates θ=61 ° and ϕ=77 °. Fig. 3.3e shows that the Zeeman splitting is maximum for this specific direction of the field, which corresponds to the NV spin axis.

Stability of the NV axis in the trap

In addition to give the vector spin direction, this data indicates that the particle is not substantially rotating in the trap over the time of the measurement. Because the measurement is based on averaging, the different projections of the magnetic field on the NV axis would under rotation result in substantial broadening of the ESR resonance, preventing the two different transitions from being resolved. We attribute this behaviour, which was observed for the majority of the trapped NDs (around 80%), to the asymmetrical shape of the nanocrystals. Fig 3.5 shows scanning electron microscopy (SEM) pictures of an evaporated droplet of a concentrated ND solution. This geometrical asymmetry mostly contributes to the stability of the ND within the trap by providing a preferential trapping orientation [128]. The orientation is determined by the preferential alignment of the major polarizability axis of the polarization ellipsoid of the particle along the local direction of the light electric field in order to minimize the interaction energy with the electric field (Fig. 3.6).

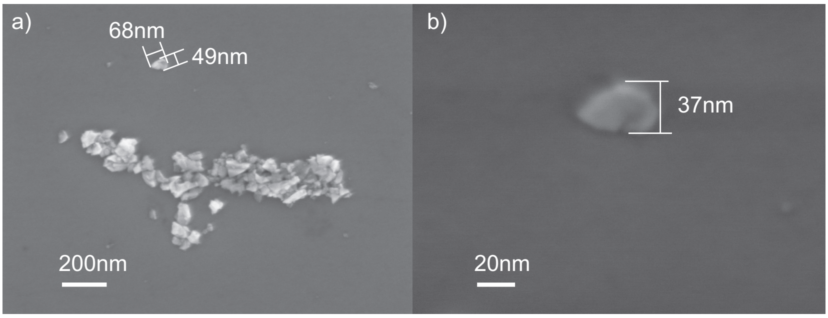

Figure 3.5: **Morphology of the NDs.** a) SEM image obtained on an evaporated droplet of a concentrated ND solution. Most of the crystals have an asymmetrical shape, which prevents rotation in the optical trap. b) Tilted SEM image of a single ND. This crystal has a size of 68 nm x 49 nm x 37 nm.

Long-term stability was evaluated by repeating these measurements after 30 min, and we found that the NV orientation was the same within an error range of ±10 °. This strongly depends on the aspect ratio of the trapped ND and the power of the trapping laser creating the trapping potential.

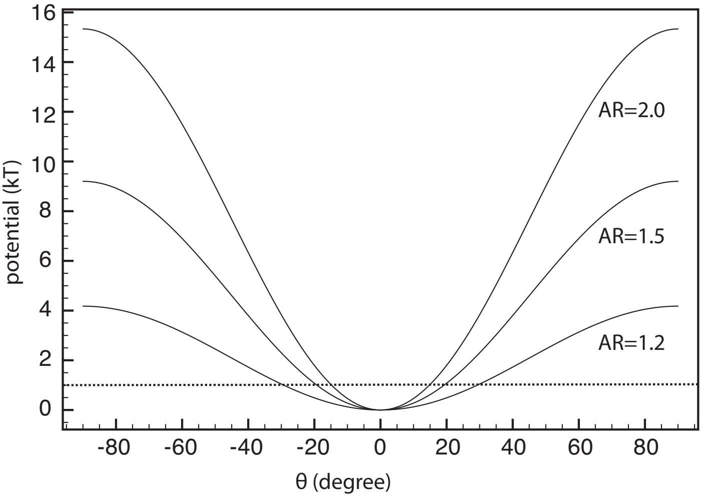

Figure 3.6: **Dependence of the trapping potential on the aspect ratio of the ND** We use the same parameters as in Fig 2.17, with the particle assumed to be placed at the center of the trapping well. The different aspect ratios (ARs) under consideration are indicated by labels. The angle denotes the orientation of the near field referred to the long axis of the particle ellipsoid, where the potential is set as zero. The region likely visited by the orientation of the particle lies under the dashed line potential=kT. The potential is proportional to the weighted polarizability $\alpha_{||} cos2(\theta) + \alpha_{\perp} sin2(\theta)$ where $\alpha_{||}$ and $\alpha_{\perp}$ are the polarizabilities along and perpendicular to the long axis, as calculated from Gans theory [129].

3.2.2 Control of the NV axis orientation

We have seen that the asymmetrical shape of the ND gives a preferential orientation of the ND in the optical trap with respect to the trapping E-field. Consequently, changing the orientation of the polarization axis of the trapping laser should allow us to control the orientation of the NV axis with respect to the optical axis.

This additional degree of control over the trapped NV is demonstrated in Fig. 3.7a-c, in which we monitor the orientation of the NV axis for three different directions of the trap polarization. For each orientation of the E-field polarization axis, two ESR spectra are acquired for two successive orientations (x and y) of the magnetic field (at constant magnitude B=1.5 mT). An angular change $\Delta\phi$ in the direction of the field polarization leads to a rotation of the NV axis (projected in the xy plane) by the same angle, therefore permitting us to align the NV axis orientation relative to the B-field lines to be probed. The reproducibility of the experiment is shown in Fig. 3.8 on another trapped ND. The rotation control of the spin axis of the NV centre is confirmed and plotted versus the trapping laser polarization in Fig. 3.9. Although trapping with a Gaussian beam limits rotation around a single axis, further rotation control could be achieved by introducing electric fields having components along the z-axis either through additional trapping beams or through beam shaping with a spatial light modulator (SLM)[130].

The control of the electron spin not only in three dimensions, but also through angular rotation is a huge advantage of this technique. Unlike AFM-based approaches, where the NV axis is fixed, this angular control potentially enables vectorial magnetometry in liquid environment. Therefore not only the projection of the magnetic field on a fixed spin axis can be measured, but the spin axis can be rotated to be able to detect the direction of the magnetic field.

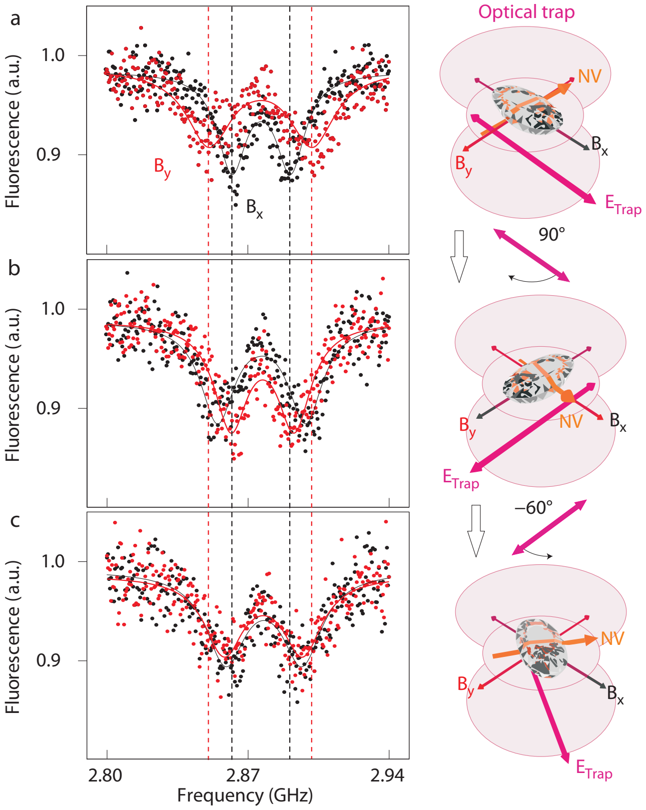

Figure 3.7: **Orientation control of an optically trapped single spin.** Control of the NV-axis orientation by rotating the polarization of the trapping laser. Two consecutive frequency sweeps were performed for each orientation of the ND with a constant magnetic field directed in X and Y, respectively. A rotation in polarization by an angle $\Delta\phi$ rotates the NV-axis by the same angle in the XY-plane as monitored by the change in $\vec{\mu}\vec{B}$. The dashed lines indicate the position of the magnetic field splitting in a) as a guide to the eye. Due to internal strain, the ground state for this NV was already degenerate for B=0.

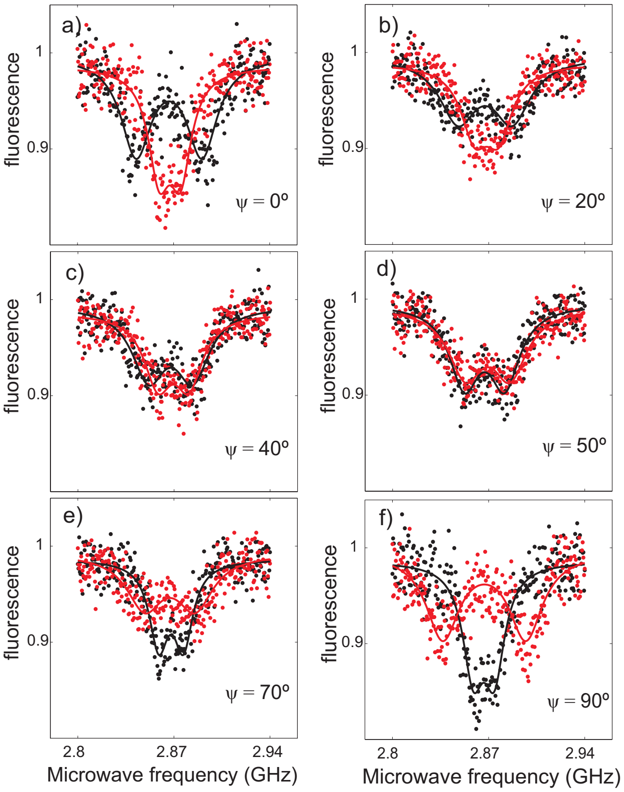

Figure 3.8: **Reproducibility on the orientation control of the trapped NV:** This additional set of data on another trapped NV demonstrates the rotation of the spin axis over 90 degrees. a)-f) Evolution of the ESR spectrum while changing the orientation of the polarization axis of the trapping beam. For each orientation of the E-field polarization axis, two ESR spectra were acquired for two successive orientations (X, black dots, and Y, red dots) of the magnetic field (at constant magnitude). The solid lines are two-Lorentzian fits of the measurements. The polarization of the trapping laser beam was varied in five steps. The orientation change of the ND is observed by measuring the projection of the constant magnetic field in X and Y, respectively, on the NV centre axis. The actual angle of the NV axis in the XY plane is calculated using equations 3.2 and 3.3.

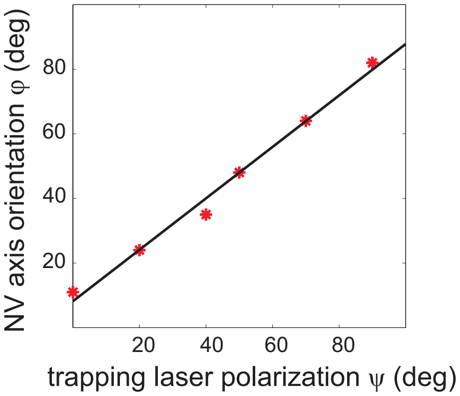

Figure 3.9: **Angular change $\Delta\phi$ of the NV axis** versus the angular change in the trapping beam polarization $\Delta\psi$ (red dots). A fit (black solid curve) proves the linear dependence of $\Delta\phi$ with $\Delta\psi$.

3.2.3 Magnetic sensitivity and broadening of the ESR linewidth

The magnetic sensitivity is liked to the characteristics of an ESR measurement. The intensity of an ESR spectrum as a function of the microwave frequency ν_m has a lorentzian shape and can be expressed as

$$I(\nu_m) = R[1 - CF(\frac{\nu_m - \nu_0}{\Delta\nu})], \tag{3.4}$$

where R is the fluorescence count rate, C the contrast of the ESR spectrum and F the ESR line shape factor. The magnetic sensitivity of a NV centre measured with an ESR spectrum is linked to the minimum detectable magnetic field δB_{min} through [42, 131, 132]

$$\eta(T/\sqrt{Hz}) = \delta B_{min}\sqrt{\Delta t} \approx \frac{h}{g\mu_B}\frac{\sqrt{R}}{max|\frac{\partial I}{\partial \nu_0}|}, \tag{3.5}$$

which can be written as

$$\eta \approx 0.77\frac{h}{g\mu_B}\frac{\Delta\nu}{C\sqrt{R}}. \tag{3.6}$$

It has been shown that the contrast C of the ESR as well as the linewidth $\Delta\nu$ is dependent on the MW power and the green excitation power [132]. Therefore the ESR spectrum can be optimized for a higher sensitivity in the magnetic field measurement by adjusting the MW power and the green excitation laser

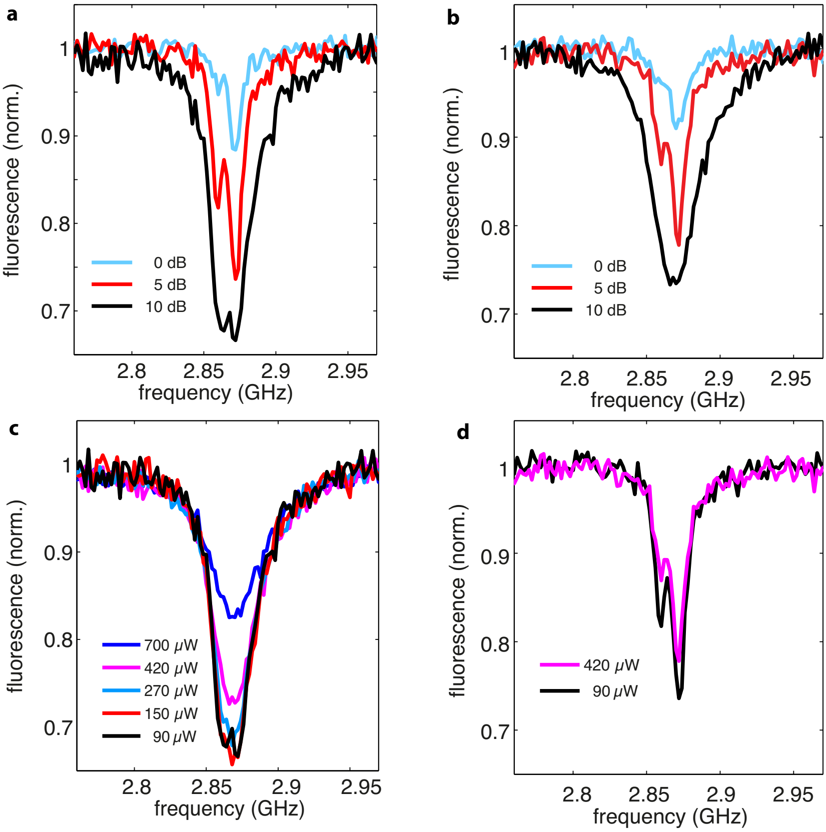

Figure 3.10: **Power broadening of the ESR spectrum for adsorbed NVs.** a),b) For a constant green laser excitation of a) 90 μW and b) 420 μW, ESR spectra are acquired for different MW power. c),d) For a constant MW power of c) 10 dB and d) 5 dB, ESR spectra were acquired for different green laser power.

power. Fig. 3.10 shows the dependence of MW power and green laser power for an adsorbed NV centre. The linewidth $\Delta\nu$ broadens for increasing MW power (Fig. 3.10a,b) but the contrast also increases. For decreasing green laser illumination (Fig. 3.10c,d), the contrast C increases and $\Delta\nu$ decreases but the fluorescence count rate R drops as less photons arrive to excite the NV centre.

Thus a trade-off has to be found to have sufficient contrast C but at the same time a narrow linewidth $\Delta\nu$ and a high fluorescence count rate R. We choose a laser power around the saturation power (150 μW) to avoid population to the metastable state from $m_s = 0$ and a microwave power of 5 dB. As the MW power is also dependent on the distance of the ND from the MW antenna, the studied NVs are usually not further than 20 μm away from the MW wire.

Fig. 3.11 shows microwave (MW) power broadening of the ESR line width for both an adsorbed and a trapped NV. For the trapped NV, further broadening is attributed to the small-angle precession (±10°) of the NV axis within the trap. However it is hard to compare two different NV centres. Unfortunately we couldn't study the same ND in the trap and adsorbed, as it is either in solution or on the coverslip.

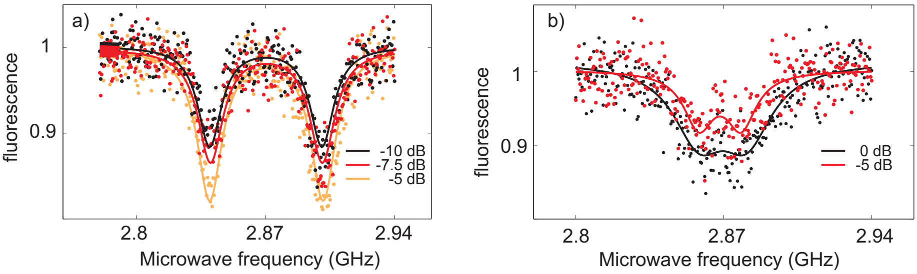

Figure 3.11: **MW Power broadening of ESR spectra for both adsorbed and trapped NV centres.** ESR spectra on an adsorbed (a) and trapped (b) NV centre for different levels of microwave power. The solid lines are two-Lorentzian fits to the measurement. A decrease in linewidth as well as in contrast is observed for lower power. The linewidth of the trapped NV centre is broader than for an adsorbed one. We attribute this additional broadening to the small-angle precession (±10°) that the ND experiences in the trap.

Fundamentally the ESR linewidth is limited by the spin-spin decoherence time T_2^* and the optimum sensitivity of a magnetometer based on a single electronic spin is given by [42]:

$$\eta \approx \frac{\hbar}{g\mu_B \Upsilon \sqrt{T_2^*}} \tag{3.7}$$

where $\Upsilon \leq 1$ is related to the detection efficiency of the system. A bath of nuclear spin impurities from neighboring ^{13}C atoms creates a fluctuating magnetic field that decreases the coherence time of the electron spin of the NV centre. As discussed in chapter 1 usually NDs have more impurities compared to bulk diamond. Incidentally, according to Taylor et al. [42], magnetic sensitivities for NDs with a dephasing time $T_2^* = 1$ μs, measured in section 2.3.3, can be as low as 1 μT Hz$^{-1/2}$.

Here we calculate the magnetic field sensitivity η of the trapped spin from the experimental ESR data using [132]

$$\eta = 0.77\ h\ \Delta\nu\ (2\ \mu_B\ C\ \sqrt{R})^{-1} \tag{3.8}$$

where h is the Planck constant, $\Delta\nu$= 0.023 GHz is the linewidth of the ESR dip, μ_B the Bohr magneton, C = 0.08 is the contrast for the ESR and R = 40 kHz is the count rate. The sensitivity depends on the particular trapped NV because C and R can change due to the different environment provided by each ND. We use here values averaged over 5 NVs and get a sensitivity of η = 40 μT Hz$^{-1/2}$.

This novel manipulation technique is therefore an ideal platform for probing vectorial magnetic fields in three dimensions with nanoscale resolution and a magnetic sensitivity of 40 μT Hz$^{-1/2}$ [42, 132]. The sensitivity in our measurements could be improved by implementing a Ramsey type magnetometry [42], avoiding power broadening [132] and increase the stability of the ND in the trap using higher aspect ratios and feedback trapping techniques [133].

In parallel to our work Horowitz et al. reported on ESR measurements of NV centres in optically trapped NDs [134]. They trap several NDs with hundreds of NV centres in each ND. That approach facilitates the trapping process as no selection and pre-characterization is needed. Yet, the data treatment of the ensemble measurement due to random dynamics inside the trap is more sophisticated to perform magnetometry. Trapping a single ND with a fixed orientation of the NV axis allows a higher level of control for vectorial magnetometry.

3.3 Probing the Local Density of States (LDOS)

In the last section we used the electron spin of the NV centre to probe magnetic fields. Here we use the electric dipole to probe the electromagnetic Local Density of States (LDOS) of its surrounding. We access the LDOS by measuring the radiative lifetime of the single NV centre [96].

3.3.1 Decay rate of an electric dipole

The fluorescence lifetime is expected to be inversely proportional to the number of available photon states that are accessible to the emitting electric dipole of the NV. This quantity is also known as the electromagnetic LDOS, which measures the sum of field intensities of all normalized photon modes as a function of both photon energy and space position [95].

The decay rate Γ_0 of an electric dipole $\mathbf{D}$ in vacuum is given by Fermi's golden rule:

$$\Gamma = \frac{2\pi}{\hbar} \sum_{f} | < f|\hat{H}_I|i > |^2 \delta(\omega_i - \omega_f), \tag{3.9}$$

with $\hat{H}_I = -\mathbf{DE}$ the interaction Hamiltonian in the dipole approximation [96] and $|i >$ and $|f >$ the initial and final state of the system.

This decay rate can also be rearranged to:

$$\Gamma = \frac{\pi\omega}{3\hbar\epsilon_0} \mathbf{D}^2 \rho_\mu(\mathbf{r}_0, \omega_0) \tag{3.10}$$

where $\rho_\mu$is the LDOS projected on the dipole of the emitter with:

$$\rho_\mu(\mathbf{r}_0, \omega_0) = \frac{6\omega_0}{\pi c^2}[\mathbf{n}_\mu \cdot Im\{\mathbf{G}(\mathbf{r}_0, \mathbf{r}_0; \omega\} \cdot \mathbf{n}_\mu], \tag{3.11}$$

where $\mathbf{G}$ is the Greens function and $\mathbf{n}$ the dipole orientation. Therefore the LDOS for a given emission frequency is directly proportional to the imaginary part of the induced field (represented by the Greens function) acting back on the dipole [95].

When considering a dissipative environment the decay rate Γ_{tot} presents two contributions:

$$\Gamma_{tot} = \Gamma_{rad} + \Gamma_{nr} \tag{3.12}$$

Γ_{rad} is called the radiative decay rate and corresponds to the photons emitted spontaneously by the quantum system that can be detected by measuring the fluorescence. The second part, Γ_{nr} is the non-radiative dacay rate, corresponding to the de-excitation of the emitter via photon absorption. Performing a fluorescence lifetime measurement we can only access to the total radiative decay rate Γ_{tot} that is inverse proportional to the LDOS.

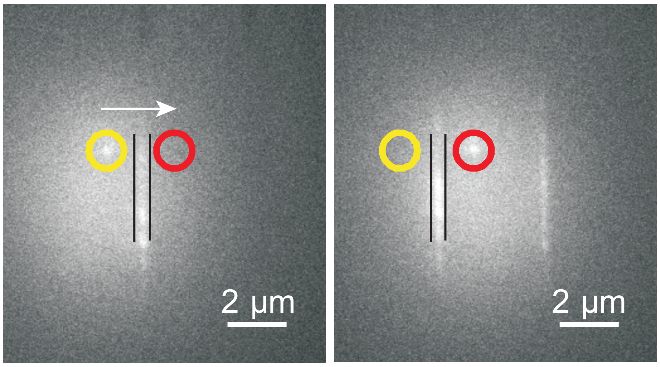

Figure 3.12: **Positioning of a single NV centre relative to a 250 nm thick TiO_2 waveguide.** The image is taken with an EM-CCD camera while illuminating a large area with a 532 nm laser beam focused to the backfocal plane of the objective (section 2.2). The bright spot is the photoluminescence arising from the NV centre, while the bright lines correspond to the fluorescence from the TiO_2 waveguide.

3.3.2 LDOS mapping with a trapped NV centre

For this purpose, a trapped single NV centre was raster-scanned across a TiO_2 channel waveguide patterned on a glass substrate. The ND is brought as close as possible to the surface sample in such a way that we do not lose the nanocrystal while scanning it over the 100 nm high waveguide. At each point of the scan (scan step, 15 nm), we measured the fluorescence lifetime of the NV centre (Fig. 3.13a). The fluorescence intensity profile features a maximum above the waveguide. This maximum is attributed predominantly to significant autofluorescence from the TiO_2 (as can be seen in the EM-CCD fluorescence image in Fig 3.12). Conversely, information about the NV-waveguide coupling and the LDOS is provided by the lifetime data, from which the contribution of the NV fluorescence can be isolated by separating its long-lived fluorescence signal from the short-lived autofluorescence of the rest of the structure using a two-exponential fit. A clear lifetime decrease is observed when the NV is in close proximity to the TiO_2 waveguide. A decrease in lifetime of the NV centre is thus associated with an increase in the LDOS.

The LDOS profile across the waveguide is calculated using a Boundary Element Method [135] that solves the Maxwell equations at each point for a radiating unit dipole. As the emission of the NV centre is broadband, we calculate the LDOS for ten different wavelengths and weight them in proportion to the experimental NV emission spectrum. The LDOS is normalized to that of a

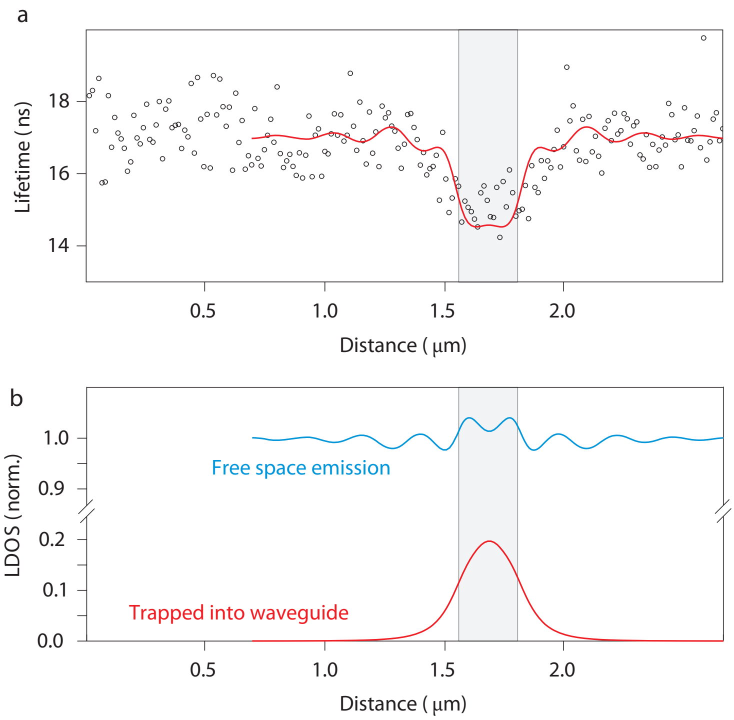

Figure 3.13: **LDOS mapping across a TiO_2 waveguide** a) Fluorescence lifetimes of the NV centre, which were acquired at different points across and over the waveguide (average over 2 consecutive scans). The red line shows the calculated lifetime of a single emitter scanned 50 nm above a 250 nm TiO_2 waveguide. b) Calculated free space and waveguided contributions of the LDOS for a dipole scanned 50 nm above a 250 nm TiO_2 waveguide. The free space part has only a small contribution in comparison to the guided part that is trapped in a waveguide mode and is responsible for the change in lifetime of the NV centre. The shaded area corresponds to the position of the waveguide.

dipole positioned away from the waveguide. In Fig 3.13b, we show the spatial dependence of two contributions to the LDOS: emission far from the system (upper curve) and emission into a guided mode of the waveguide (lower curve). The former seems to depend only mildly on position showing an oscillation that origins from the interference between the emitter and the reflected field from the glass surface and the dielectric waveguide [136]. The waveguide mode contribution however shows a peak that follows the observed decrease in lifetime, which is due to the higher density of states above the waveguide. Two fitting parameters are used to match the calculated LDOS with the inverse of the measured fluorescence lifetime: the distance of the emitter to the waveguide, as we don't know where the emitter is located in the 70 nm ND and a constant to account for the baseline of the LDOS determined by the fluorescence lifetime away from the waveguide. As shown by the red line in Fig 3.13a, the theory is in good agreement with the experiment for a dipole 50 nm away from the waveguide and a baseline of 17 ns.

3.4 Conclusion

In this chapter I demonstrated spatial and angular manipulation of optically trapped single NV centres. Beyond opening new opportunities for nanoscale magnetic and optical sensing in three dimensions and in liquid environments, it is non-invasive and is potentially applicable to cell biology [137, 138]. We also foresee that an extension to multiple ND trapping could be used for the implementation of flying qubits [139] and nanoscale control of spin-spin interactions using plasmonic tweezer structures [140], realizing a significant advance in scalable quantum computing and simulation schemes.

4

Near field-assisted trapping and positioning

Controlling the interaction between single quantum emitters and a photonic or plasmonic nano-structure is important for application in integrated solid-state quantum devices, such as single photon sources [141, 35, 9, 142]. The ability to position the quantum emitter at an optimum position is thus crucial, for example to expose it to the enhanced local density of optical states (LDOS) produced by a resonant mode. Positioning quantum emitters close to plasmonic structures has so far been achieved by combining surface chemistry with two-step electron beam lithography (EBL) [143, 144]; by identifying the adsorbed emitter first and then positioning the plasmonic nanostructure through EBL in a second step [60, 145]; or by mechanically pushing the emitters with the tip of an atomic force microscope (AFM) to the desired position [27, 146, 28].

Optical trapping appears to be a suitable tool for achieving dynamical control over the position of the emitter, as we have demonstrated in chapter 3 through three-dimensional manipulation of a single 70 nm nano-diamond (ND) crystal hosting a single nitrogen-vacancy (NV) centre using optical tweezers. However, as the trapping strength is proportional to the volume of the particle, smaller particles would require unrealistically high powers to be trapped. As an alternative to conventional optical tweezers, the force field produced by hotspots in plasmonic nanostructures enables the trapping of particles as small as 10 nm upon relatively low incident laser intensities [147, 140, 148, 149].

We present in this chapter near-field-assisted positioning of NDs in the plasmonic hotspot of a gold gap antenna and quantify through lifetime measurements the electromagnetic coupling between NV centres and the antenna plasmon mode.

In section 4.1 we explain the experimental implementation of near field based trapping. In section 4.2 the deterministic positioning of the NDs to a gap plasmonic antenna is demonstrated and in section 4.3 the interaction between the nano-antenna and the NV centre is studied by analyzing the lifetime change of the NV centre, when placed in the hot spot of the antenna.

4.1 Surface Plasmon-based trapping

Surface plasmons (SP) are electromagnetic resonances supported at the interface between a metal and a dielectric that leads to the enhancement of light absorption and a strong field concentration at the metal surface. In the specific case of 3D metal nanostructures (Localized surface plasmons), plasmon properties can be tuned by either playing on the geometry, illumination conditions and dielectric environment. Through an appropriate design, metal nanostructures can be engineered to act either as efficient nanosources of light or nanosources of heat. While the basic physics of (SP) is now well understood [150], there has been over the last years a clear move towards applications [151].

With the aim of miniaturizing and integrating optical tweezers at the surface of a chip, a novel trapping scheme based on surface plasmons-induced forces was recently suggested [152]. In this configuration, a substrate, patterned with micro/nano plasmonic structures and illuminated with unfocused laser light is used to create a near-field optical potential landscape able to trap objects in solution at specific locations of the surface. By properly engineering the geometry of the pattern and its illumination conditions, efficient trapping of micro-colloids under laser intensity 2 to 3 orders of magnitude weaker than the intensity needed with conventional optical tweezers for trapping the same objects was demonstrated [153].

Since the trapping mechanism originates from the confinement of the optical field nearby the plasmonic structures (which act as a microlens substituting the high numerical aperture objective required in conventional optical tweezers), this approach enables achieving parallel trapping in an array of traps maintaining a single laser beam illumination. More recently, it was shown that optical antennas formed by two adjacent gold bars that enable concentrating light well beyond the diffraction limit in their gap and can be used to extend plasmon trapping down to the submicron scale. In particular, efficient parallel trapping of 10 nm gold beads under moderate incident laser intensity was reported [148].

4.1.1 Experimental implementation

In this chapter we experimentally demonstrate deterministic near field assisted trapping and positioning of NDs hosting NV centres with a setup similar to the one used in chapter 3 (Fig. 4.1).

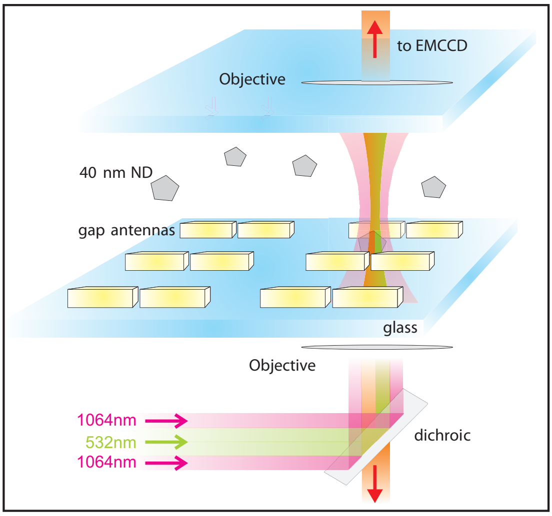

Figure 4.1: **Scheme of the near field-assisted trapping setup.** The NDs are in solution between two coverslips separated by 30 to 50 μm. The gap-antenna array is located on the lower cover slip. The distance between neighboring antennas is 5 μm, which allows us to excite an individual antenna with a NIR laser beam ($\lambda = 1064$ nm) focused through a high-NA objective (NA=1.2). A green laser ($\lambda = 532$ nm) is superimposed to the NIR beam in order to image in real time the evolution of the fluorescence from the NV centres as well as the auto-fluorescence from gold using an EMCCD camera.

In our experiment, the surface of a glass cover slip is patterned with a periodic array of gold gap antennas, each of them formed by two identical rods separated by a 40 nm gap. The dimensions of the rods (145 nm long, 56 nm wide, and 55 nm high) are chosen such that each individual antenna mode overlaps with the trapping wavelength at 1064 nm (Fig. 4.2). A pitch of 5 microns ensures reduced interaction between adjacent antennas. The patterned surface is covered with a 2:1 glycerol/water solution of NDs[1] (C=10 ppm). The NDs have an average size of 40 nm and host between 1 and 4 NV centres

---

[1] Adamas Diamond

each. We formed a closed chamber with a second cover slip. Monitoring of the ND containing NVs is performed by wide field fluorescence imaging using an EMCCD (section 2.2).

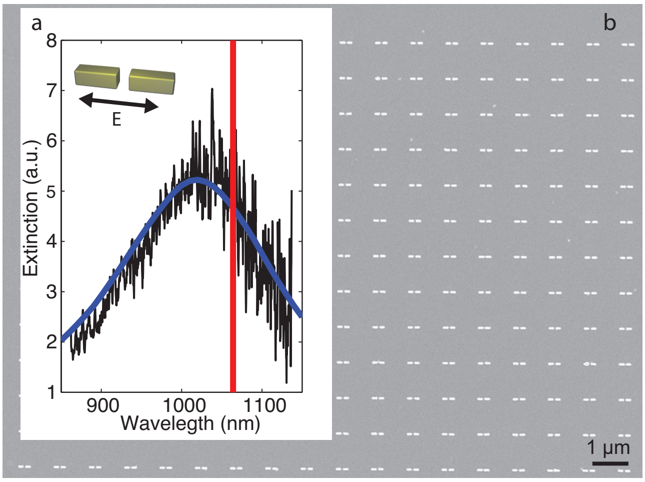

Figure 4.2: **Gold gap antenna for near field-assisted trapping of single nanodiamonds** a) The surface plasmon resonance of gold gap antennas immersed in a 2:1 glycerol/water environment is tuned into the NIR (measured black curve) for an antenna arm length l = 145 nm and gap g = 40 nm. The calculated extinction cross-section exhibits a pronounced maximum that peaks slightly above a wavelength of 1000 nm, corresponding to the excitation of the bonding dipole-dipole mode (blue curve), in good agreement with the measured extinction. The vertical red line indicates the wavelength of the trapping laser (λ = 1064 nm). b) SEM image of the dense antenna array (distance between antennas fixed at 1 μm) fabricated by electron beam lithography and used to measure the extinction cross-section spectrum presented in a).

Our approach consists in focusing the 1064 nm laser on a predefined antenna (3 mW incident power, and linear polarization along the antenna long axis). A ND diffusing near the antenna experiences an optical potential that results from the combined effect of the trapping beam and the near-field hotspots. As a result of that, the ND gets automatically guided towards the regions of maximum intensity and eventually sticks to the antenna. To facilitate sticking to the antenna, we use NDs that were chemically treated to enrich their surface with carboxylic groups, which are known to favor adhesion to gold [154]. Figure 4.4 displays the three most frequent configurations observed when systematically characterizing the position of the immobilized NVs.

4.1.2 Numerical optical near field of gap antennas

In order to obtain further insight into the trapping mechanism, we calculate the optical near-field intensity map of the fabricated gold antennas (Fig. 4.3) using the boundary-element method (BEM) [155, 135] and a dielectric function for gold taken from Ref. [156].

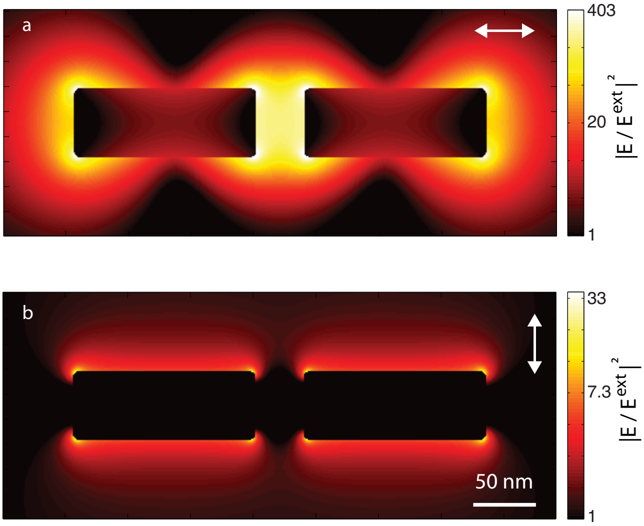

Figure 4.3: **Electric near-field intensity of a gold gap antenna.** a) Near-field intensity distribution in the half plane of a gap antenna illuminated with a NIR laser (1064 nm wavelength) polarized along the antenna long axis (white arrow). Light incidence is normal to the plane of representation. The field enhancement is very pronounced in the gap region, as well as at the ends of the antennas. b) For a laser polarized perpendicularly to the main antenna axis (white arrow), the near-field around the antenna shows much smaller values compared to a). As the optical trapping force of the antenna is proportional to the gradient of the electric field intensity, the particle is attracted to the position of maximum field enhancement at the metal surface. For the gap antenna the highest intensity is at the gap, as well as at the two outer ends.

For the calculations we use the geometrical parameters extracted from the SEM image (Fig. 4.4) of the fabricated antennas (55 nm diameter, 38.5 nm gap, and 145 nm length of each arm). For simplicity, we model the antennas as rounded cylinders of circular cross section. This is a reasonable simplification, as the lateral width of the antennas (56 nm) is very similar to the gold layer thickness (55 nm), and the actual particle morphologies are rounded at the edges. Furthermore, since the substrate index of refraction (n = 1.5) is similar to that of the surrounding liquid (n = 1.43), we assume a uniform environment of index of refraction 1.46. Fig. 4.3a shows the electric near-field intensity map at a wavelength of 1064 nm in the antenna half plane for incident polarization along the antenna long axis (see arrow). Each antenna arm exhibits a dipole-like profile, which contributes to three intensity maxima: a main maximum in the gap region, which is accompanied by two secondary maxima at the outer arm ends. Importantly, we did not observe any trapping events for an incident polarization perpendicular to the antenna long axis, thus confirming the dominant contribution of the antenna near-field (Fig. 4.3b).

4.2 Deterministic positioning of single ND in the hot spot of plasmonic antennas

The commercial NDs were annealed in air to remove *sp*^{2} carbon and treated with acid (HNO_3/H_2SO_4) to enrich the surface with carboxylic groups, which are known to favour adhesion to gold [154]. In a first step near-field assisted trapping brings NDs in the vicinity of gold structures. Once in the hot spot of the plasmonic antenna the carboxilic groups attach to the gold and the ND is adsorbed at the gold surface of the antenna.

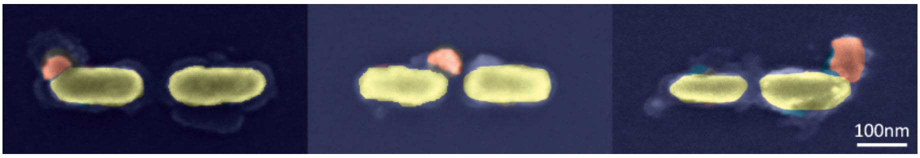

Figure 4.4: **SEM images of three different antennas with positioned NDs (false colour).** Their preferred positions match with the maximum field enhancement of the antenna.

In addition to SEM imaging (Fig. 4.4), we compare the fluorescence intensity map of the antenna array before and after ND trapping and positioning (Fig. 4.5). For this purpose, a green laser (532 nm wavelength, 100 μW power) is focused onto the sample and raster-scanned. An APD is used to collect the auto fluorescence of the gold and the fluorescence of the NV centre, both of them excited by the green laser. A higher fluorescence signal is observed from those antennas on which a ND was immobilized, as a result of additional fluorescence from the NV centre. Furthermore, Fig. 4.5 demonstrates the deterministic character of our approach. The NIR laser was intentionally positioned on a sequence of several gap-antennas forming a cross-like pattern (Fig. 4.5b). Fig. 4.5 demonstrates that only irradiated antennas show ND trapping.

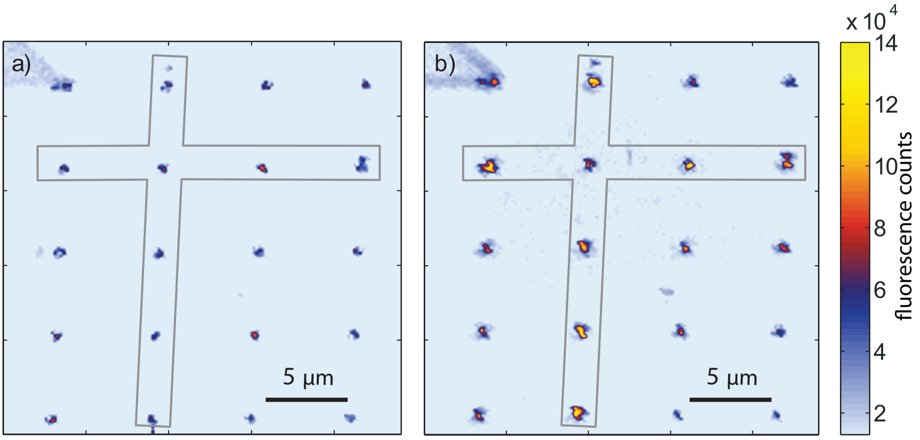

Figure 4.5: **Fluorescence map of the antennas before and after trapping NDs.** A green laser (532 nm wavelength, 100 μW power) is raster-scanned over an array of antennas before (a) and after (b) positioning the NDs. The auto fluorescence of the gold is clearly observed in (a), as it lies in the same spectral range as the fluorescence from the NV centres. After deterministic positioning of NDs at the irradiated antennas forming a cross shape, the same area is scanned with the green laser using the same power. The higher fluorescence contribution from the trapped NVs is shown in (b). The cross-shaped lines are a guide to the eye.

4.3 Coupling of the NV centre to the plasmon antenna

The interaction of the immobilized NV with the nano-antenna is quantified by analyzing the change in its fluorescence lifetime. The fluorescence lifetime of the hybrid system consisting of a single nano antenna coupled to 1-4 NV centres was measured using picosecond green laser excitation. The fluorescence from gold decays much faster (over a sub-picosecond time scale) [157] than the one from the NV centres (nanoseconds), so we can separate the two of them using a bi-exponential fit. Fig. 4.6 shows a histogram of the lifetime measured on different hybrid ND gap-antenna structures compared with lifetime measurements of NDs adsorbed on an unpatterned glass coverslip.

4.3.1 Fluorescent lifetime of the hybrid system

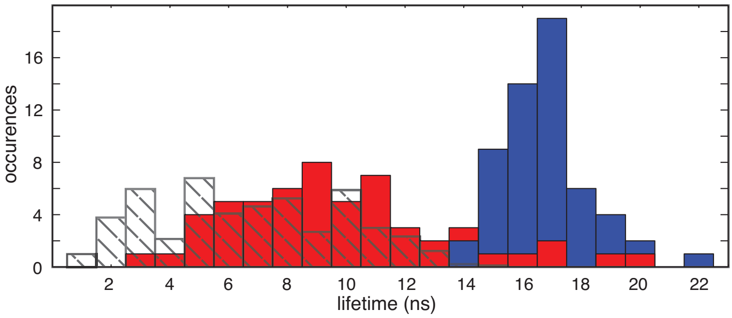

Figure 4.6: **Coupling of the immobilized NVs to the antenna.** Statistical distribution of the lifetime measured on single NDs adsorbed on a glass substrate (blue histogram), compared with that for NDs positioned on gold nano-antennas (red histogram). The presence of the gold nano-antenna both reduces the lifetime (from 17 ns to 8.5 ns) and broadens the statistics (FWHM from 3 ns to 7 ns). The hashed-bar histogram is obtained from the statistical average over the solid curves in Fig. 4.7 within the grey areas, assuming a homogenous distribution along the plotted ranges of x and y, and including the same broadening as in the blue histogram of the glass-supported NDs.

The lifetime τ of NV centres lying on glass peaks at around 17 ns. When coupled to a gap-antenna, it is reduced due to the Purcell effect. Its actual value strongly depends on the precise location on the structure. Indeed, statistical analysis on a large amount of complexes shows a lifetime distribution centered around $\tau = 8.5$ ns with values ranging from 5 ns up to 16 ns. A simplified theoretical analysis provides further insight into these results, as we discuss next. We first calculate the Purcell factor $\gamma(\omega) = \Gamma(\omega)/\Gamma_0(\omega)$ (or equivalently the normalized LDOS [95]) of a randomly oriented dipole for a frequency range corresponding to the emission from the NV centre (from 637 nm up to 800 nm). The frequency-integrated Purcell factor, with $\Gamma_0(\omega)$ the decay rate far from the antenna and weighted with the intensity of the NV centre spectrum $I(\omega)$ taken far from the antenna, takes maximum values near the plasmonic hotspots of the antenna (Fig. 4.7).

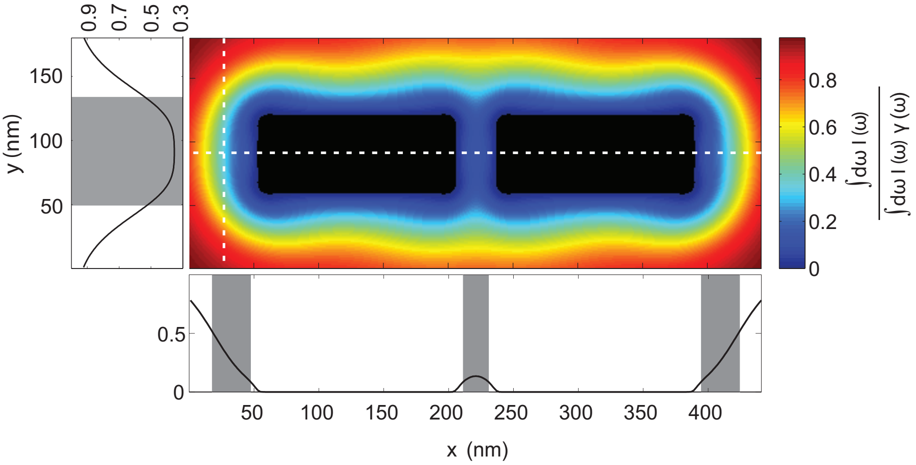

Figure 4.7: **Simulation of the modification in the NV center lifetime as a function of its position along the half plane of the gold gap-antenna.** The simulated geometry is the same as in Fig. 4.3. The Purcell factor was integrated over the whole fluorescence spectrum of a NV centre. The two dashed white lines indicate the regions along which the normalized calculated fluorescence lifetime is represented in the solid curves to the left and at the bottom of the main plot. Because the 40 nm NDs are attached to the antennas at the locations where the near field enhancement is sufficiently strong to produce trapping, a trapped NV center is most likely to be located at distances between 5 nm and 35 nm away from the external ends of the antenna or relative to the gap. These regions are highlighted in grey on the left and bottom plots, and used to produce the theory histogram in Fig. 4.6, as explained above.

We select two representative cuts (dashed white curves) along which we represent this magnitude (left and lower parts of Fig. 4.7). The grey areas on these plots show the preferred locations of the trapped NV centers, based on the following two assumptions: first, a 40 nm ND is most probably trapped at the regions of largest field enhancement; and second, a NV centre inside a ND is usually more than 5 nm away from the diamond surface [158, 106]. We therefore expect the most probable locations of the NV centre to be at distances ranging from 5 nm to 35 nm away from the end of each antenna or the gap region. The statistical analysis of this selected region provides a qualitative understanding of the observed large changes of the Purcell factor as a function of distance from the antenna. The statistical distribution of lifetimes, resulting from a convolution between the distribution of the Purcell factor extracted from the simulation in Fig. 4.7 and the distribution of the NV centre lifetime measured on glass, is represented in Fig. 4.6 (hashed bars), in good qualitative agreement with the experiment. Although this analysis is rather qualitative, it illustrates the mechanism leading to a reduction in lifetime and broadening of lifetime distribution: the former is a consequence of the Purcell effect that takes place in trapped NVs near the hotspots, whereas the latter results from the broad dispersion of the magnitude of the Purcell factor over the region most likely visited by the NVs of the trapped NDs. A more precise position determination of the NV in the ND would be obtained either through stimulated emission depletion (STED) [159] or through the cathodoluminescence measured in a electron microscope with sub-nanometer resolution [106, 160].

4.3.2 Quantum nature of the hybrid system

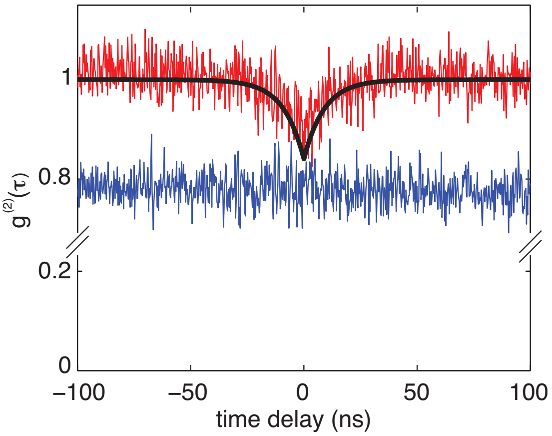

Figure 4.8: **Second order correlation function from NV centres positioned in the hot spot of a gold gap antenna.** Antibunching in the second order correlation verifies the quantum nature of the emitters. The blue curve is the correlation measurement of the background fluorescence from the antenna. The antibunching dip can not go below the background level, even for a single emitter.

To demonstrate the quantum nature of our system, second order correlation measurements show the presence of an antibunching dip at zero time delay (Fig. 4.8). Since the background of our measurement is very high due to the auto-fluorescence of the gold, the dip does not go below a certain value. This value is defined by coincidence measurements performed on a gold antenna. The correlation measurements confirm that our ND solution contains one to four NV defects per ND.

4.4 Conclusion

In conclusion, we have demonstrated a new tool capable to deterministically positioning a single ND hosting 1-4 NV centres into the hotspot of a plasmonic antenna. The gradient force of the excited plasmon acts as localized tweezers to drive the functionalized NDs to the regions of largest field enhancement of the antenna, where they are adsorbed. This is verified by SEM and fluorescence imaging. The proximity of the emitter to the antenna is further corroborated by the observation of a decrease in fluorescence lifetime. In section 5.2 we benefit from the NIR field enhancement at the position of the NV centre to demonstrate enhanced optical modulation of the NV excited lifetime using relatively low powers of the modulating NIR laser.

5

Fast optical modulation of the fluorescence from a single NV centre

During the study of manipulating a single ND with optical tweezers shown in chapter 3, we observed that the NIR laser illumination has a strong effect on the fluorescence yield of the NV. In this chapter we focus our attention on this effect and systematically study the fluorescence decrease, lifetime and ODMR signal in presence of NIR illumination to understand the origin. These experimental data are supported by a model based on the ability of the non resonant NIR laser to trigger a so far unknown fast decay channel of the NV centre by the promotion of the excited state electron to a dark band. Moreover we demonstrate that a single NV centre at room temperature can operate as an optical modulator under non-resonant CW illumination. More precisely, a modulation of the green laser driven fluorescence of more than 80% at a time response faster than 100 ns is measured, which is controlled through an independent near-infrared (NIR) gating laser. This simple concept opens a new approach towards the implementation of nanoscale optical switching devices.

5.1 Optical Switches

The motivation for using photons rather than electrons not only comes from their faster dynamics but also from their lower crosstalk and minor environmental decoherence, which enable a high degree of integration and the realization of quantum operations [161]. Unlike charged particles such as electrons, photons interact extremely weakly with each other [162]. Therefore, an optical switch requires the mediation of a physical system to produce efficient photon-photon interactions.

5.1.1 Different approaches for optical switching

Different approaches to optical transistors have been proposed [163, 164, 165], often based on nonlinearities in well-defined photonic resonators. The ultimate goal for future optical commutation technologies is to rely on single atoms or molecules having the ability to manipulate light down to the single photon level, which feature an intrinsically high nonlinearity and grant access to exploiting the quantum nature of light [2]. In this direction, a first single-molecule optical transistor has been recently achieved at low temperatures [4]. Additionally, the inclusion of a third, dark state in the electronic structure of the atom or molecule has been argued to be particularly advantageous to reduce the effect of thermal decoherence [166, 167]. The quest for operating such optical nano-transistor at room temperature is attracting considerable attention, as it would have major impact on photonic technologies and allow high-speed signal processing in general.

In parallel, research on single quantum emitters (either molecules or quantum dots (QDs)) has focused on achieving stable and efficient light emission with well-defined properties [21, 168, 18, 169]. However a long-term stable source of single photons at room temperature still remains challenging with these emitters, since they usually suffer from bleaching or blinking. In this context, NVs in diamond have recently been intensely investigated due to their emission stability [17].

5.1.2 NV centre as an optical modulator

NVs are artificial atoms protected from their environment by a diamond shell. Consequently, they are immune to both blinking and bleaching [17] and their electron spin features a long coherence time, even at room temperature [82]. Their suitability for quantum-optics experiments has opened a new route towards the implementation of solid-state quantum simulators at room temperature [170, 68]. Despite the sustained effort to study the properties of NVs

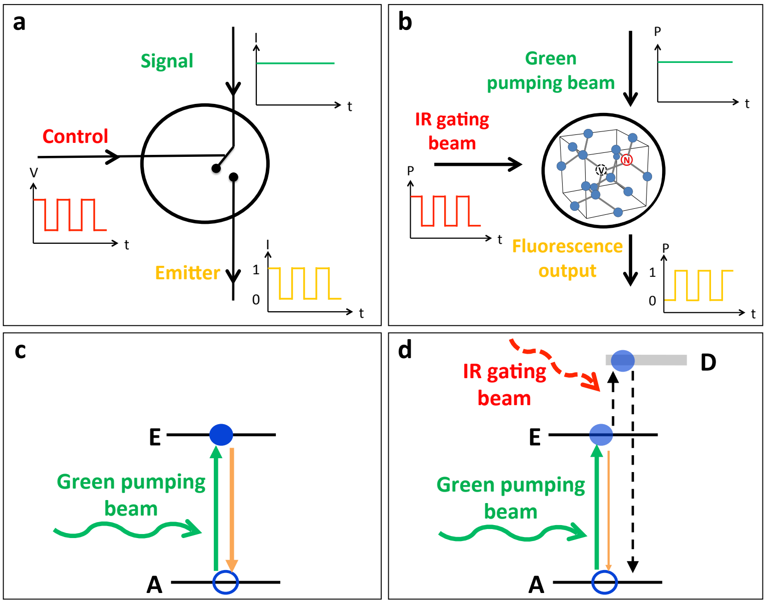

Figure 5.1: **Concept of optical switch based on a single NV centre.** a) and b), Similar to its electronic counterpart (a), the emitter signal of the optical switch (NV-fluorescence upon continuous green-laser illumination) is controlled by a gate provided by a modulated non-resonant NIR laser (b). c) In absence of the NIR laser, the NV centre can be regarded as a two level system excited by a green pumping beam. d), The NIR laser populates a dark band D, which decays non-radiatively, thus reducing the fluorescence output (d) compared with the emission without NIR laser (c).

over the last decade [22], new insights on their energy states are still emerging [171, 86]. In this section we describe an unconventional configuration in which a single NV operates as an all-optical nano-modulator at room temperature upon non-resonant continuous-wave (CW) near-infrared (NIR) illumination.

Our concept of an optical modulator based on a single NV centre is sketched in Fig. 5.1. The NV centre has a steady fluorescence (output signal) when pumped with a CW green laser (input signal). Illumination with a non-resonant CW NIR laser (gate signal) drives the excited state back to the ground state via non-radiative decay. In the following, we experimentally demonstrate the viability of this new gating channel, and speculate the potential involvement of a dark band of states to which the NIR laser promotes the excited state (section 5.3.1). This mechanism thus opens the possibility of controlling the number of emitted photons by adjusting the intensity of the NIR gating laser.

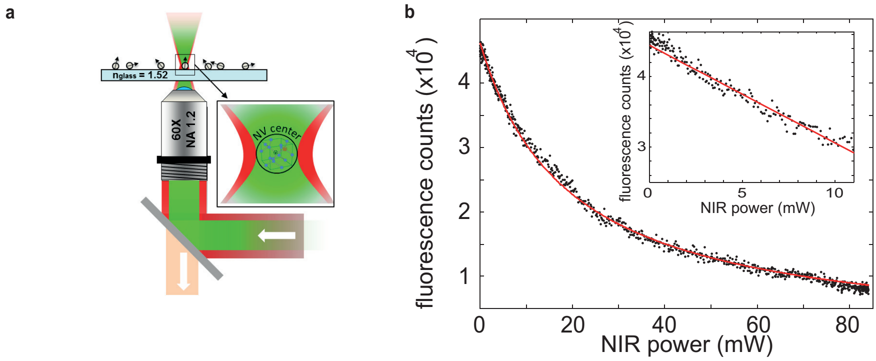

Figure 5.2: **Optical quenching of the NV luminescence under NIR illumination.** a) A green laser ($\lambda = 532$ nm) is focused through a high numerical-aperture objective (NA = 1.2) to excite a single NV centre in a ND crystal deposited on a glass coverslip. A NIR laser ($\lambda = 1064$ nm, shown in red in the sketch) is super-imposed to the 532 nm laser. The emitted fluorescence (orange) passes through a dichroic filter and is detected with two APDs. b) Setting the excitation power of the green laser to 55 μW while increasing the power of the NIR laser, a $1/(1 + P_{NIR}/Psat)$ fluorescence decrease is observed, which is apparently linear for small power (inset) and nonlinear when P_{NIR} increases.

In our experiment, 70 nm NDs are dispersed on a glass coverslip that is placed in the sample plane of a scanning confocal fluorescence microscope. The NVs are pumped with a 532 nm CW laser (input beam) after focusing through an immersion objective lens (NA=1.2), and their fluorescence (output beam) is collected back through the same objective and sent to an Avalanche PhotoDiode

(APD) (Fig. 5.2a). Handbury-Brown and Twist (HBT) measurements enable us to identify a ND that hosts a single NV (section 5.3.3). The 1064 nm laser beam (gating beam) is superimposed with the 532 nm beam after passing through an Acousto-Optic Modulator (AOM) that allows us to temporally modulate its power (Fig. 5.3).

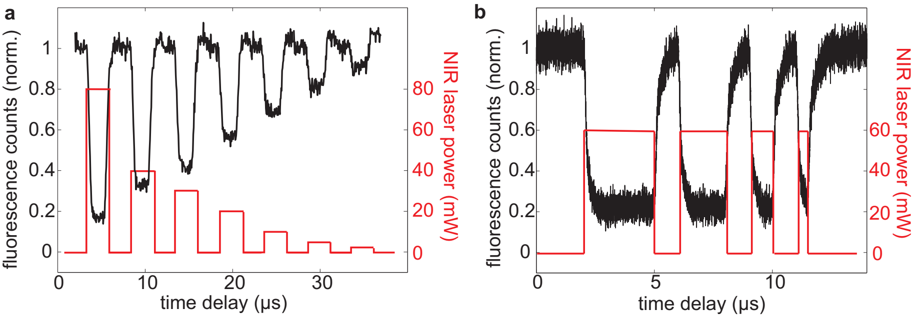

Figure 5.3: **Optical modulation of the NV luminescence.** By modulating the gating NIR laser with an Acousto-Optic Modulator (AOM) for constant green laser excitation power, a mimicking modulation of the NV fluorescence is observed. Tuning the power of the gating laser pulses allows us to reach different fluorescence decay levels (a). Here, we demonstrate the possibility of defining at least 8 states (i.e., well differentiated output levels) for potential application as a digital optical switch. The measured emission from the NV for different gating laser pulse lengths ranging from 3 μs down to 200 ns illustrates the time response of the system (b). In our configuration, the response is faster than 200 ns and is limited by the electronic time response of our AOM.

We start by examining the effect of 1064 nm illumination on the fluorescence yield of a single NV centre under constant pumping with 55 μW green light. The NIR power dependence of the fluorescence counts plotted in Fig 5.2b shows a monotonous drop that is apparently linear below 15 mW (inset of Fig. 5.2b) before reaching saturation. This demonstrates the possibility of modulating the fluorescence emission from a single NV by up to 80 % for this chosen green excitation power. Quenching of fluorescence could be obtained with other molecular species by means of alternative mechanisms such as conformational transformation in photochromic molecules [172, 173]. Nevertheless, conversely to what happens with molecules or QDs that can bleach or blink [21, 18], NV centers are stable and bright emitters, allowing us to observe this effect at room temperature and over a long time span [82, 22]. A decrease in the fluorescence of NVs has been observed in prior studies upon Stimulated Emission Depletion

(STED) under resonant excitation [159], multiphoton absorption induced by high power pulsed laser [174], or even local heating to hundreds of degrees [175], or even change of the NV centre charge state [176]. In contrast, we here invoke a radically different physical mechanism, as emphasized by the fact that our non-resonant CW NIR illumination of a few tens of mW cannot trigger any of the above-mentioned mechanisms.

Fig. 5.3a shows the evolution of fluorescence from the same NV centre while applying a sequence of NIR laser pulses (3 μs pulse width) with decreasing powers. The high stability of the NV emission enables us to define eight different output states. Thus, the NV centre gated by an NIR laser can be operated as a multi-level digital modulator. It is worth underlining that a single NV centre can be routinely used over several days without noticing any degradation in the emission properties. Also, identical results were repeated on several NVs from the same batch as well as on NVs from different providers. In order to assess the time response of the switch effect, the NIR pulse duration was changed from 3 μs to 200 ns while maintaining a fixed NIR laser power (Fig. 5.3b). The magnitude of the fluorescence drop is conserved for NIR pulses as short as 200 ns. We actually attribute this limit to the time response of the AOM used for the NIR laser modulation.

Working point of the modulator

The drop of fluorescence counts is dependent on the green excitation power as well as on the NIR laser power. Fig. 5.4a shows the evolution of the normalized fluorescence drop induced by a NIR laser as a function of the green excitation power for a fixed NIR gating power of $P_{NIR} = 80$ mW. The drop decreases when increasing the green excitation power. On the other hand, Fig. 5.4b shows the NIR saturation power P_{sat} as a function of the excitation power. The NIR saturation power P_{sat} is retrieved from the $1/(1+P_{NIR}/Psat)$ fluorescence decrease data shown in Fig. 5.2 for different excitation powers. The required NIR saturation power increases linearly when the green excitation power is increased. That means that the lower the excitation green power, the smaller the gating NIR power required to achieve large fluorescence modulation. Nevertheless, it is important to notice that a reduction of the green laser power leads to a decrease in fluorescence counts (as shown on the saturation curve in Fig. 5.7a). This implies that the power requirement of such modulator is limited by the sensitivity of the fluorescence detection and the coupling efficiency. Therefore, a trade-off in this system is to find a power that results in enough fluorescent counts and at the same time has the largest drop in fluorescence.

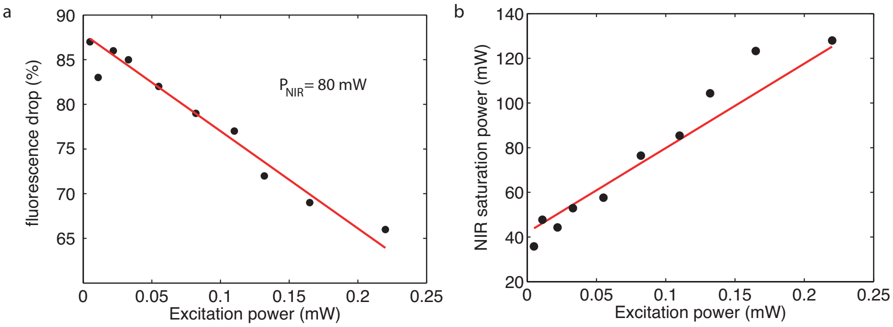

Figure 5.4: **Working point of the modulator** a) Fluorescence drop as a function of green excitation power for a fixed NIR power P_{NIR}=80 mW. b) Fitted NIR saturation power of the drop of fluorescence as a function of green excitation power. The red lines are linear fits.

5.2 Modulation enhancement with a plasmonic cavity

In the previous section we showed that for a fluorescence drop of 80 % we need NIR gating laser powers of almost 80 mW (Fig. 5.3). In practice, this power is still very high for application to an optical modulator. This gating laser power can be drastically decreased by coupling the NV center to a plasmonic cavity as demonstrated in chapter 4.

We have demonstrated that we are able to position a single ND with NV centers in the hot spots of a plasmonic gap antenna. The deterministic positioning of the ND in the hotspot of the antenna and its enhanced coupling has an additional intrinsic advantage: the ND is preferentially placed in a region of maximum NIR intensity enhancement, and therefore, any physical effect driven by the NIR light is expected to be amplified. In particular, we explore below the modulation of NV fluorescence in a hybrid NV-nanoantenna system driven by a NIR control laser.

Fig. 5.5 shows the switching property measured on the hybrid system for two different polarization directions. The green pumping laser power is set to 100 μW (close to saturation) and the NIR power has been fixed to 3.3 mW in Fig. 5.5a and temporally modulated in Fig. 5.5b. When the electric field of the NIR laser is orientated along the antenna we observe a background-corrected fluorescence drop of 80 % whereas a perpendicular polarization only produces a modulation of 20 %. Using the near field enhancement associated to the

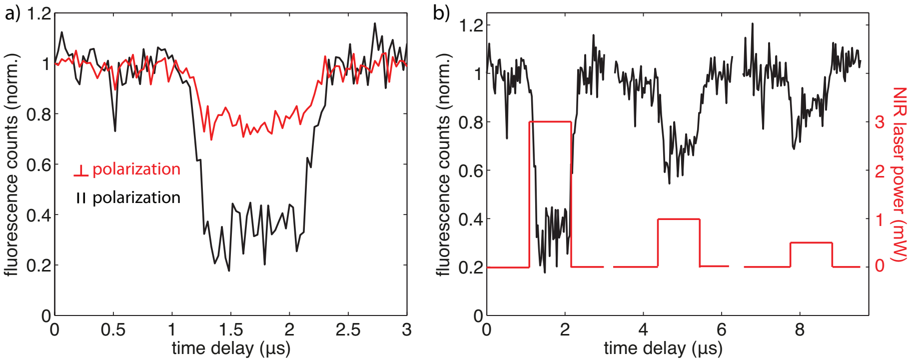

Figure 5.5: **Modulation of the NV centre fluorescence intensity using a NIR laser resonant with the gap plasmon of the gold nano-antenna.** a) Applying a 3.3 mW NIR laser, while maintaining the green-laser excitation power constant (P = 100 μW), a modulation of the NV fluorescence is observed. The modulation is strong when the electric field is polarized along the main antenna axis (black curve) due to the excitation of the antenna NIR gap plasmon. Lower modulation is observed for perpendicular polarization, where the gap plasmon resonance is not excited. This allows us to control the magnitude of the switching effect by adjucting the polarization. b) Using the near-field enhancement associated with the antenna plasmon resonance, we show that a NIR power as low as 0.5 mW is sufficient to modulate the fluorescence, whereas 10 mW are required to obtain the same change in the absence of a nano-antenna (Fig. 5.8). The graphs are normalized and background corrected.

antenna plasmon resonance, we show that a power as low as 3 mW is necessary to modulate the fluorescence by 80 % (versus 80 mW are required to get the same change in absence of nano-antenna).

5.3 Model for NIR gated fluorescence modulation

The dynamics and response of the fluorescence from a gated single NV is thoroughly analyzed in this section, where we find excellent agreement with a model based upon a master rate equation involving three energy bands (Fig. 5.6): the excited and ground states E and A, as well as a dark state D that is reached upon NIR illumination. After a few microseconds of CW green laser illumination, the system evolves towards the $m_s = 0$ manifold [22], and thus, we can assume that states A and E are spin polarized, with a high probability into the $m_s = 0$ levels of the ground and excited NV triplets. In fact, as most of the de-excitation events are associated with the intense and broad phonon sideband of the NV centre, narrow zero-phonon line features may be ignored in the fluorescence process and the excited states of the NV are treated as an energy band.

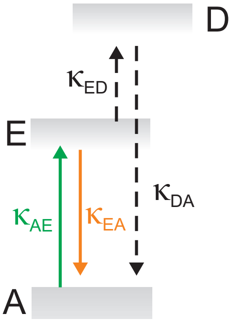

Figure 5.6: **Model of the switching mechanism of a single NV centre in diamond.** Model of energy bands for a NV centre gated with an NIR laser, consisting of a triplet ground state A, a triplet excited state E and a fast decaying dark band D. κ_{AE} is the pumping rate, κ_{EA} is the de-excitation rate from the excited state E, κ_{ED} is the transition rate towards the dark state D and κ_{DA} the decay rate from the dark state D to the ground state A.

5.3.1 Rate equation model

We model the dynamics of the NV by means of a master rate equation in which we neglect quantum coherences. This is a reasonable approximation when discussing statistical measurements such as those reported here. We consider three energy levels (A, E and D) as shown in Fig. 5.6. The population of these levels (ρ_A, ρ_E and ρ_D) is assumed to be spin-averaged and we neglect effects arising from inter-system crossing (ISC), which is valid for green laser excitation powers lower than saturation [119]. The dynamics of the system is then ruled by the master equation

$$\frac{d\rho_A}{dt} = -\kappa_{AE}\rho_A + \kappa_{EA}\rho_E + \kappa_{DA}\rho_D \tag{5.1}$$

$$\frac{d\rho_E}{dt} = \kappa_{AE}\rho_A - \kappa_{EA}\rho_E - \kappa_{ED}\rho_E \tag{5.2}$$

$$\frac{d\rho_D}{dt} = \kappa_{ED}\rho_E - \kappa_{DA}\rho_D \tag{5.3}$$

where κ_{EA} and κ_{DA} are intrinsic decay rates from the excited state E and the dark band D; $\kappa_{AE} = \alpha P_G \kappa_{EA}$ and $\kappa_{ED} = \beta P_{NIR} \kappa_{EA}$ are excitation rates assumed to be proportional to the green-laser and NIR-laser intensities, respectively, with proportionality constants α and β, expressed in units of the natural decay rate κ_{EA}. The steady-state solution of these equations is given by

$$\rho_A = \kappa_{DA}(\kappa_{EA} + \kappa_{ED})/[\kappa_{DA}(\kappa_{EA} + \kappa_{ED}) + \kappa_{AE}(\kappa_{DA} + \kappa_{ED})] \tag{5.4}$$

$$\rho_E = \kappa_{AE}\kappa_{DA}/[\kappa_{DA}(\kappa_{EA} + \kappa_{ED}) + \kappa_{AE}(\kappa_{DA} + \kappa_{ED})] \tag{5.5}$$

$$\rho_D = \kappa_{AE}\kappa_{ED}/[\kappa_{DA}(\kappa_{EA} + \kappa_{ED}) + \kappa_{AE}(\kappa_{DA} + \kappa_{ED})] \tag{5.6}$$

From here, we obtain the fluorescence rate as

$$F = \eta\kappa_{EA}\rho_E = \eta\kappa_{EA}\frac{\alpha P_G}{1 + \alpha P_G + \beta' P_{NIR}} \tag{5.7}$$

where

$$\beta' = \beta(1 + \frac{\kappa_{EA}}{\kappa_{DA}}\alpha P_G) \tag{5.8}$$

and η is the collection efficiency of the setup. Also, the lifetime of E is obtained from the rate equations by studying the exponential decay of ρ_E when the system is prepared as $\rho_E = 1$ and $\rho_A = \rho_D = 0$ at $t = 0$. This leads to the intuitive result

$$\tau_E = \kappa_{EA}^{-1}\frac{1}{1 + \beta P_{NIR}}. \tag{5.9}$$

When fitting our experimental data in section 5.3.2 using equation 5.7, we find that the best fit is obtained under the assumption of a large ratio $\kappa_{DA}/\kappa_{EA} >> 1$, so that we find an P_G-independent parameter $\beta' = \beta$.

The main assumption of the model is the additional fast decay proportional to P_{NIR}, which is plausibly mediated by promotion to a dark band D. The nature of this band is an open question, although it is likely connected with higher-energy states reached via NIR photon absorption from the E band. Higher-energy states are more susceptible to decay non-radiatively, as they can access a larger number of levels through Auger and other electronic processes mediated by Coulomb interaction. In our model, we assume a promotion rate $\kappa_{ED} = \beta P_{NIR}$ proportional to the NIR power, followed by fast decay from D to the ground state A. This is compatible with the sub-femtosecond time scale that is characteristic of non-radiative electronic transitions. Actually, the best fit to our data is obtained under the assumption $\kappa_{DA} >> \kappa_{EA}$ (section 5.3.2).

5.3.2 Experimental verification of the model

In what follows, we show that the NIR laser drives the system from E to A through an additional decay channel at very high rate compared with the natural decay rate κ_{EA}. In the absence of NIR illumination, only states A and E are involved. Excitation of the system from A to E occurs at a rate $\kappa_{AE} = \alpha P_G \kappa_{EA}$ proportional to the green-laser power P_G, whereas decay from E to A proceeds via radiative decay with a typical rate $\kappa_{EA} = 1/(35 \text{ ns})$, that can change for different NV centers [115]. In our time-averaged measurements, it is safe to neglect quantum coherences and describe the system through a master rate equation, which leads to a fluorescence rate (section 5.3.1)

$$F = \eta \kappa_{EA} \alpha P_G / (1 + \alpha P_G), \tag{5.10}$$

where $\eta = 0.005$ is the detection efficiency of our system [53]. This produces an excellent fit to the green-laser-power-dependent fluorescence rate in absence of the NIR laser by choosing $\alpha = 0.009\ \mu\text{W}^{-1}$ (Fig. 5.7a).

The effect of the NIR laser is best observed through the reduction that it produces in the lifetime of the excited state E (Fig. 5.7b). The NV is first prepared in the $m_s = 0$ manifold upon extended green laser illumination followed by a 1 μs waiting time and is then excited with a 100 ps green-laser pulse. The ensuing time-resolved fluorescence reveals the lifetime, which is controlled by both natural decay at a rate κ_{EA} and NIR-assisted decay at a rate $\beta P_{NIR} \kappa_{AE}$. According to section 5.3.1 the lifetime τ_E is given by $\tau_E = (\kappa_{EA})^{-1}(1 + \beta P_{NIR})^{-1}$. This produces an excellent fit to the measured data with the choice $\beta = 24.8\ \mu\text{W}^{-1}$ (Fig. 5.7b). The full dependence of the fluorescence rate on green-laser and

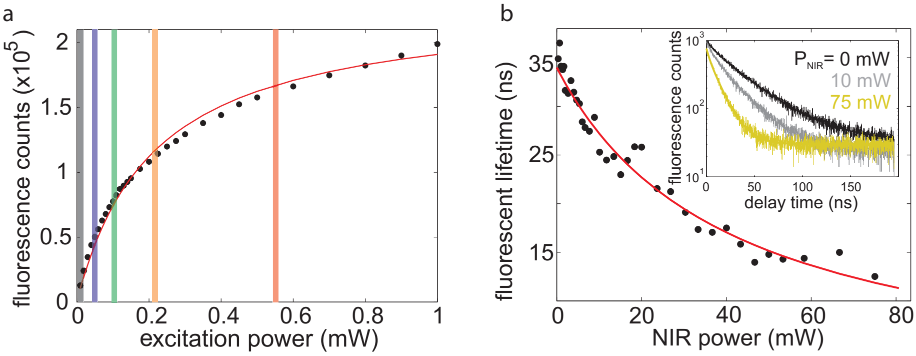

Figure 5.7: **Dependence of the fluorescence modulation of a single NV centre in diamond.** a) Saturation of the NV fluorescence as a function of green-laser power P_G in the absence of NIR laser ($P_{NIR} = 0$). The red solid curve is a fit of the fluorescence F to the formula extracted from the three-level rate equation model sketched in Fig. 5.6: $F = \eta\kappa_{EA}(\alpha P_G/(1 + \alpha P_G))$, where η is the detection efficiency, κ_{EA} is the natural E→ A decay rate and $\alpha = 0.009\ \mu\text{W}^{-1}$. b) Time-resolved measurements performed on a single NV centre after excitation with a 100 ps green laser pulse under continuous NIR illumination. The measured power dependence of the excited-state lifetime (black dots) is extracted from the fits, as shown in the inset for three different NIR powers. The red solid curve is a fit of the fluorescence lifetime to the model with equation 5.9, using $\beta = 24.8\ \mu\text{W}^{-1}$.

NIR-laser powers predicted by the rate-equation model reduces to

$$F = \eta\kappa_{EA}\frac{\alpha P_G}{1+\alpha P_G+\beta P_{NIR}} \tag{5.11}$$

with α= 0.009 μW^{-1} and β=24.8 μW^{-1}.

This simple expression, using the coefficients extracted from the previous fit, is actually reproducing a detailed set of measured NIR-power-dependent profiles for different green-laser powers rather accurately with the single abovementioned choice of parameters α and β (Fig. 5.8), thus corroborating the validity of our model.

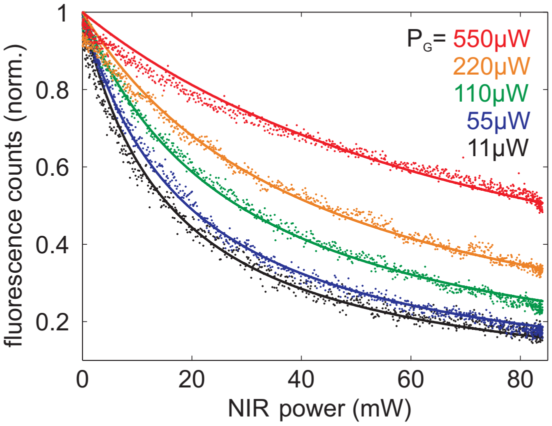

Figure 5.8: **Dependence of the fluorescence modulation of a single NV centre in diamond and its simulation.** Normalised drop in background-corrected fluorescence with increasing NIR laser power for different levels of CW green-laser excitation power (see labels), corresponding to the vertical lines in Fig. 5.7 with the same colour code. The solid curves are a fit of the fluorescence signal F using the previously fitted values of parameters α and β. All data are acquired from the same single NV centre, and all theory curves are calculated for the same values of parameters α and β.

This good agreement between experiment and theory (assuming D as a fast decaying dark state) is further verified in the following sections. We address a possible role of a ISC, a possible charge transformation, spin dependence and temperature dependence upon NIR illumination.

5.3.3 Second-order correlation upon NIR illumination

We have seen that our proposed model is in excellent agreement with the experimentally observed drop in fluorescence. Here we show, how the NIR illumination effect is observed in correlation measurements.

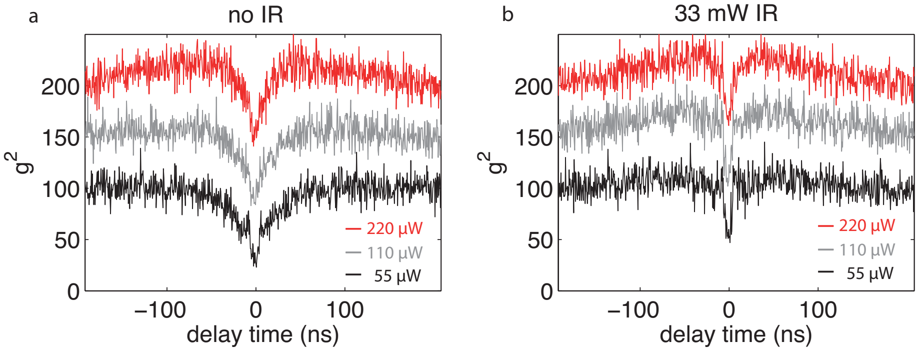

Figure 5.9: **Second-order correlation of a single NV centre with and without NIR illumination.** a) Second-order correlation taken without NIR illumination for different green excitation powers: below saturation (black), at saturation (grey) and above saturation (red). Bunching is observed for excitation powers above saturation. b) Second-order correlation in the presence of 33 mW NIR illumination for the same green excitation power as in (a). The decrease in lifetime is confirmed by the reduction of the width of the antibunching dip. A small increase in bunching is observed, which we attribute to transfer of population to the metastable state.

Fig. 5.9 presents second-order correlation measurements performed on the same single NV. The antibunching dip below 50 counts at zero delay time (Fig. 5.9a, black line) demonstrates that it contains a single NV centre. For increasing excitation power (Fig. 5.9a, grey line and red line) in the absence of NIR laser, bunching is observed when the power reaches the saturation level ($P_{sat} =$ 110 μW, Fig. 5.7a). This effect, already observed in previous experiments on NV centers (section 2.2.3), is attributed to the population of the metastable state [119, 17]. When exposing the NV centre to NIR illumination, we observe a reduction of the FWHM of the antibunching dip, which is consistent with the lifetime measurements displayed in Fig. 5.7b. Additionally, the presence of the NIR laser leads to a small increase in bunching when the green excitation power is above saturation. This indicates that, beyond the linear excitation regime, the NIR laser could also lead to a modification of the intersystem crossing (ISC) rate toward the metastable state by saturating the NV centre.

Nevertheless, the small effect observed on the bunching, even for high NIR power, indicates that the fluorescence modulation cannot be attributed to ISC. Moreover, the fast (below 100 ns) response of the effect here reported (Fig. 5.3) and the excellent agreement obtained by assuming a fast-decaying dark state in the model (section 5.3.1) both exclude an ISC mechanism.

5.3.4 Fluorescence spectrum upon NIR illumination

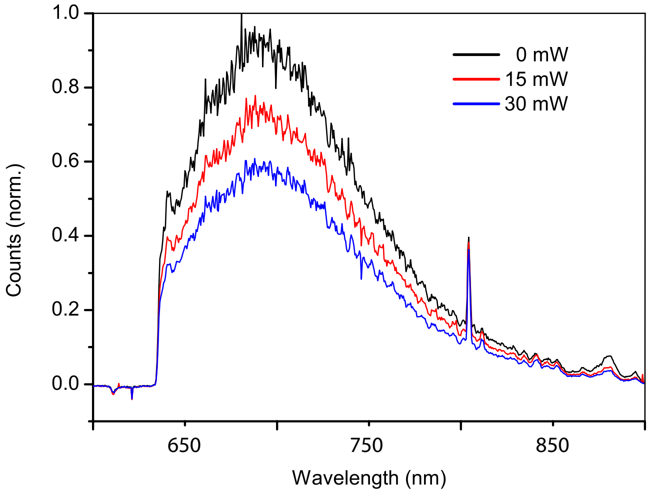

Figure 5.10: **Effect of the NIR laser irradiation on the luminescence spectrum of a single NV centre in diamond.** The spectra have been recorded for a fixed power excitation at 532 nm (200 μW) and different IR laser powers ranging from 0 mW (black curve) to 30 mW (blue curve). The spectral shape of the fluorescence is similar for different NIR powers, indicating the preservation of the NV^- charge state.

In order to rule out a charge state transformation from negative charged NV^- to neutral charged NV^0, we can additionally measure the fluorescence spectrum in dependence of NIR illumination. As the NV^0 charge state has a zero phonon line at 575 nm [177] a drastic change in the spectrum would be observed compared to the emission spectrum of the NV^-. In Fig. 5.10 the emission spectrum is shown for the same NV upon illumination of the NIR laser.

As we don't observe a change in the spectral shape apart from a decrease in counts, we can assume that the charge state is not changed. In fact, even at 30 mW the zero phonon line for the NV^- at 637 nm is still visible. The similar evolution of the phonon side band upon NIR illumination validates in some extend our assumption to define the excitation band as one state.

5.3.5 Maintaining spin polarization upon NIR illumination

When dealing with NV centers located inside NDs, spin polarization is generally not perfect and both spin states coexist [22]. As the lifetime of the excited $m_s = \pm 1$ and $m_s = 0$ spin states are different, a bi-exponential fit of the lifetime is required to fit the experimental data [178, 175]. The characteristic times of the two exponentials are associated with the fluorescent lifetime of each spin excited state and their amplitude coefficients give access to the spin polarization of the NV centre [175].

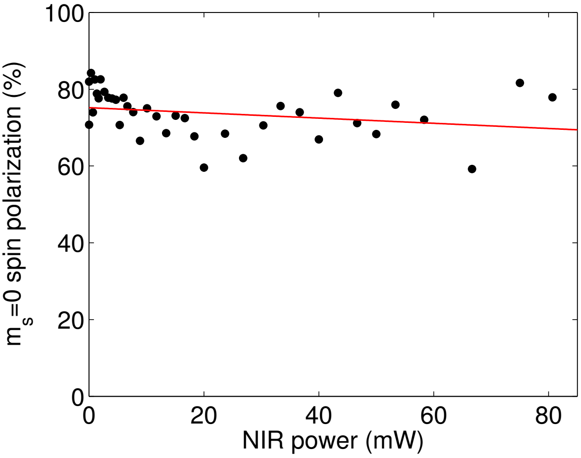

Figure 5.11: **Dependence of the spin polarization with the NIR power.** The values are extracted from the amplitude ratios of the bi-exponential fitted lifetime. The polarization is mainly kept in $m_s = 0$ state whatever NIR power applied.

In our case, we find that the spin polarization of the system is close to 80% and is not significantly modified with increasing NIR power (Fig. 5.11). Even if spin polarization was not perfectly conserved under CW NIR illumination, the fluorescence drop observed cannot be attributed to a spin depolarization, since the fluorescence drop observed (up to 80 %) is higher than the contrast between the $m_s = 0$ and $m_s = \pm 1$ states (up to 30 %). As the system is mainly polarized into the spin state $m_s = 0$, we then assume in our analysis that it can be modeled without taking into account the spin dependence of the NV centre in first approximation and Fig. 5.7a represents the lifetime dependence of the $m_s = 0$ sate.

5.3.6 Temperature dependence upon NIR illumination

We here report ODMR spectroscopy [22, 178, 82] measurements upon NIR laser illumination that allow us to rule out any temperature-related effect as the reason for the fluorescence drop. This technique relies on the possibility of optically reading out the spin state of a NV center by tracking the fluorescence emission while sweeping the frequency of an applied microwave field over the spin transition frequencies (section 2.3). When the microwave frequency is resonant with a spin transition, a drop in fluorescence is observed. In NDs, two resonances are usually observed because internal strains break the degeneracy between the $m_s = 0$ and $m_s = \pm 1$ transitions.

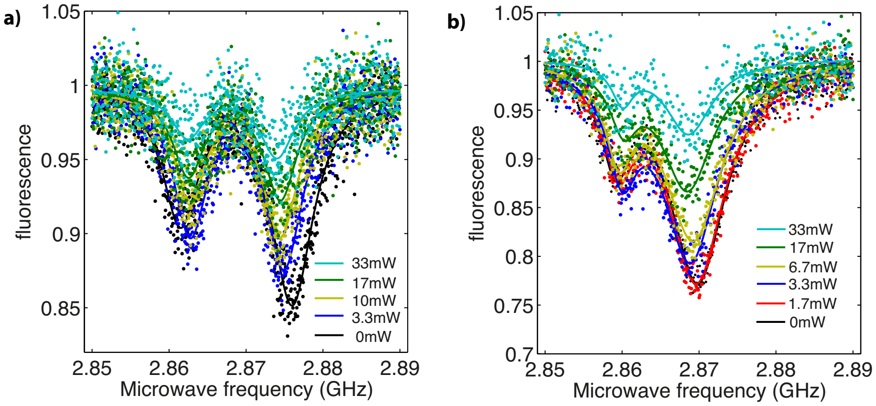

Figure 5.12: **NIR power dependence of ESR for individual NV centers**. ESR measurement for two different NV centers. Each graph shows a microwave frequency scan across the ground state transition frequencies for $m_s = 0$ and $m_s = \pm 1$. No magnetic field is applied. The splitting is due to strain inside the ND.

Several groups have recently shown a temperature dependence of the electronic spin in NV centers [175, 75, 45, 43, 44]. It was found that the zero field splitting (ZFS) parameter D of the spin Hamiltonian is shifted by 75 kHz/K [75], as extracted from an ESR measurement. An additional experiment shows that the ESR contrast of the resonances decreases with increasing temperature [175]. Here we perform ESR measurements to show the effect upon NIR illumination and demonstrate that our decrease in fluorescence is not related to a substantial increase in temperature.

Fig. 5.12 display the ESR measurements performed on two different individual NV centers as a function of NIR laser illumination. The presence of the NIR laser induces two main features, analyzed in Fig. 5.13. First, a clear decrease of the ESR contrast is observed in Fig. 5.13a,b for increasing NIR laser power. This is in good agreement with the experiments reported in section 5.3.2, where we show that the presence of the NIR laser produces a drop in fluorescence yield for the $m_s = 0$ spin state and consequently reduces the difference between the $m_s = \pm 1$ and $m_s = 0$ fluorescence intensities.

However, a similar ESR contrast decrease has already been observed for temperatures above 600 K [175]. In order to measure the temperature of the NV center, we have then analyzed the shift of the ZFS parameter D. Fig. 5.13c,d show the dependence of D on NIR power. We find a linear relation of 17 kHz/mW for NV1 and 6.3 kHz/mW for NV2, which imply a temperature increase of 7 K and 3 K, respectively, at 30 mW.

This result confirms that the fluorescence switching is not related to a temperature increase. In fact, the temperature increases by less than 10 K for a 30 mW NIR power, for which we already have a fluorescence decrease of 60 % (Fig. 5.3a). This amount of heating is typical of experiments involving focusing a mW NIR beam to a diffraction-limited spot.

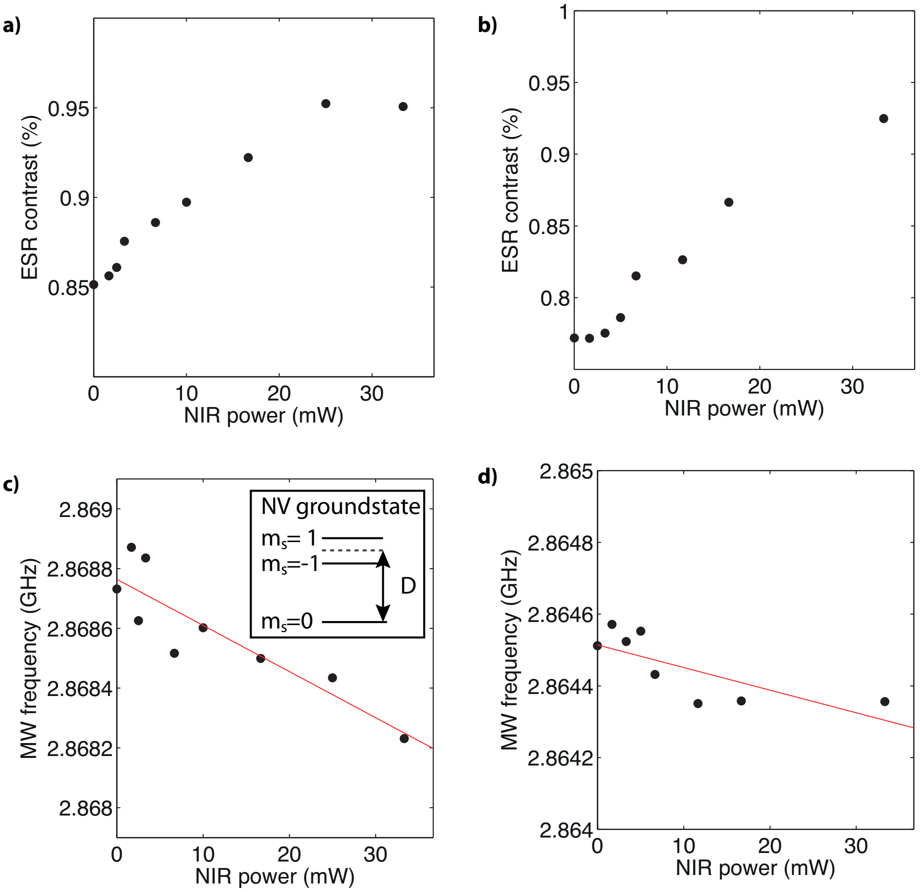

Figure 5.13: **NIR power dependence of ESR for individual NV centers**. a),b) ESR contrast in dependence of the NIR power associated to Fig. 5.12a and b, respectively. For increasing NIR power, the ESR contrast decreases as the difference in fluorescence intensity between the two spin states is decreasing due to the dark state excited by the NIR illumination. c),d), Dependence of the zero field splitting parameter D (see inset) on NIR power showing a thermally induced frequency shift of 75 kHz/K [75], which yields less than 10 K temperature increase for 30 mW illumination power.

5.4 Conclusion

We have shown a new mechanism to modify the fluorescence properties of the NV centre. The excellent agreement between our simple rate equation model and the experiment verifies the assumption that the electron in the excited state of the NV center can be promoted to a fast decaying dark band by NIR illumination.

The fast, efficient modulation of the emission of a single NV centre here presented furthermore demonstrates the principle of single-emitter optical switch operating at room temperature. The coupling to a plasmonic cavity enables to significantly decrease the necessary power of the NIR gating beam. A logical next step towards the exploitation of this concept for optical signal processing into an integrated scheme would consist in coupling a single NV to highly confined optical guided modes, as those supported for instance by a quasi-one-dimensional plasmonic waveguide [179, 180].

Conclusion and Outlook

In this thesis, I present a new avenue for manipulating an individual ND hosting a single NV centre in liquid environment. Our approach is based on optical tweezers focusing light to a diffraction limited spot creating an optical potential to deterministically trap 70 nm NDs. Remarkably, we find that the NV axis is nearly fixed inside the trap and can be controlled in situ by adjusting the polarization of the trapping light. By combining this unique spatial and angular control with coherent manipulation of the NV spin and fluorescence lifetime measurements near an integrated photonic system, we demonstrate individual optically trapped NV centres as a novel route for both three-dimensional vectorial magnetometry and sensing of the local density of optical states.

In a second step, our manipulation technique is further developed to deterministically positioning a single 40 nm ND hosting 1-4 NV centres into the hotspot of a plasmonic antenna. The gradient force of the excited plasmon acts as localized tweezers to drive the functionalized NDs to the regions of largest field enhancement of the antenna, where they are adsorbed. The proximity of the immobilized NV to the nano-antenna is corroborated by the observed decrease in its fluorescence lifetime.

During the above mentioned experiments we observe a NV fluorescence decrease upon NIR illumination. We identify the promotion of the excited electron to a so far unknown dark band with a fast decay channel as the origin of the fluorescence decrease. This assumption is verified by the excellent agreement between our simple rate equation model and the experiment.

Last but not least we demonstrate that a single NV can operate as an efficient and fast optical switch controlled through an independent NIR gating laser. Furthermore the hybrid system formed by a single NV coupled to a gold gap antenna enhances the modulation depth. We show a modulation of the NV fluorescence by more than 80 % with time response faster than 100 ns with NIR gating laser powers of a few mW.

Manipulation and positioning of individual NDs was so far achieved using AFM-based techniques. Our new approach opens a new path for sensing magnetic fields and temperature in biological environment and microfluidic channels. Besides the sensing ability, NDs with a single NV centre are promising building blocks for quantum information and quantum optics. Here, accurate positioning of the ND at predefined locations is essential. For this aim the demonstrated near field positioning of NDs hosting NV centres is an alternative approach to AFM or e-beam lithography and chemistry based techniques. Additionally, the coupling of the electric dipole to photonic and plasmonic structures is important for the realization of efficient optical interfaces for solid-state atom-like systems with potential applications in quantum communications and quantum information processing.

Moreover, the understanding of the discovered fluorescence modulation upon NIR illumination is important to possible integrated all optical circuits and the coupling to nanophotonic structures using NIR excitation sources. Furthermore the proof of the existence of a dark state population will be beneficial for further optical trapping experiments with NV centres [176].

The stable trapping of a single ND with a single NV centre could further be optimized using NDs with a higher aspect ratio in combination with a feedback trapping technique [133]. This improvement would lead to a power reduction of the trapping beam and thus prevent to alter the environment of the trapped ND, which is especially important for bio-applications.

Our approach would as well benefit from ongoing developments in the fabrication of NDs with low ^{13}C impurities to increase the coherence time of the electron spin [108]. This is important as sensitivities of magnetometry and temperature measurement depend on the coherence time of the electron spin. Furthermore NDs could then also be used for quantum information, where the spin decoherence limits the number of operations performed on one qubit.

The proof of trapping a single ND and simultaneously reading out the electron spin of the NV centre could also be conducted to the field of optomechanics. It was shown that the electron spin of the NV centre, placed on the tip of a cantilever can be coupled to the motion of the latter [181]. In parallel trapping of a nanometer sized particle in vacuum and cooling down the centre of mass was demonstrated [176, 182, 183, 184]. Trapping a ND with a single NV centre would pave the way toward a new type of magnetic field sensing by monitoring the oscillation of the ND in the trap as well as toward a hybrid system for single photon optomechanics.

Bibliography

[1] E. Comission, "http://ec.europa.eu/nanotechnology/index_en.html."

[2] D. E. Chang, A. S. Sø rensen, E. A. Demler, and M. D. Lukin, "A single-photon transistor using nanoscale surface plasmons," *Nat. Phys.*, vol. 3, pp. 807–12, 2007.

[3] M. Orrit, "Quantum light switch," *Nat. Phys.*, vol. 3, pp. 755–6, 2007.

[4] J. Hwang, M. Pototschnig, R. Lettow, G. Zumofen, A. Renn, S. Götzinger, and V. Sandoghdar, "A single-molecule optical transistor.," *Nature*, vol. 460, pp. 76–80, 2009.

[5] O. Benson, "Assembly of hybrid photonic architectures from nanophotonic constituents.," *Nature*, vol. 480, pp. 193–9, 2011.

[6] B. Lounis and M. Orrit, "Single-photon sources," *Reports Prog. Phys.*, vol. 68, p. 1129, 2005.

[7] D. E. Chang, A. S. Sø rensen, P. R. Hemmer, and M. D. Lukin, "Quantum Optics with Surface Plasmons," *Phys. Rev. Lett.*, vol. 97, p. 053002, 2006.

[8] A. V. Akimov, A. Mukherjee, C. L. Yu, D. E. Chang, A. S. Zibrov, P. R. Hemmer, H. Park, and M. D. Lukin, "Generation of single optical plasmons in metallic nanowires coupled to quantum dots," *Nature*, vol. 450, pp. 402–406, Nov. 2007.

[9] I. Aharonovich, S. Castelletto, D. A. Simpson, C.-H. Su, A. D. Greentree, and S. Prawer, "Diamond-based single-photon emitters," *Reports Prog. Phys.*, vol. 74, p. 076501, 2011.

[10] H. J. Kimble, M. Dagenais, and L. Mandel, "Photon Antibunching in Resonance Fluorescence," *Phys. Rev. Lett.*, vol. 39, pp. 691–5, 1977.

[11] B. Darquie, M. P. A. Jones, J. Dingjan, J. Beugnon, S. Bergamini, Y. Sortais, G. Messin, A. Browaeys, and P. Grangier, "Controlled single photon emission from a single trapped two-level atom," *Science*, vol. 309, pp. 454–6, 2005.

[12] F. Diedrich and H. Walther, "Nonclassical radiation of a single stored ion," *Phys. Rev. Lett.*, vol. 58, pp. 203–7, 1987.

[13] T. Basché, W. E. Moerner, M. Orrit, and H. Talon, "Photon antibunching in the fluorescence of a single dye molecule trapped in a solid," *Phys. Rev. Lett.*, vol. 69, pp. 1516–9, 1992.

[14] B. Lounis and W. E. Moerner, "Single photons on demand from a single molecule at room temperature," *Nature*, vol. 407, pp. 491–3, 2000.

[15] P. Michler, A. Kiraz, C. Becher, W. V. Schoenfeld, P. M. Petroff, L. Zhang, E. Hu, and A. Imamoglu, "A quantum dot single-photon turnstile device.," *Science*, vol. 290, pp. 2282–5, 2000.

[16] C. Santori, M. Pelton, G. Solomon, Y. Dale, and Y. Yamamoto, "Triggered Single Photons from a Quantum Dot," *Phys. Rev. Lett.*, vol. 86, pp. 1502–5, 2001.

[17] C. Kurtsiefer, S. Mayer, P. Zarda, and H. Weinfurter, "Stable solid-state source of single photons," *Phys. Rev. Lett.*, vol. 85, no. 2, pp. 290–3, 2000.

[18] B. Mahler, P. Spinicelli, S. Buil, X. Quelin, J.-P. Hermier, and B. Dubertret, "Towards non-blinking colloidal quantum dots.," *Nat. Mater.*, vol. 7, pp. 659–64, 2008.

[19] M. Orrit and T. Basché, "Steady light from quantum dots, at last. But how?," *ChemPhysChem*, vol. 10, pp. 2383–5, 2009.

[20] V. Zwiller, T. Aichele, F. Hatami, W. T. Masselink, and O. Benson, "Growth of single quantum dots on preprocessed structures: Single photon emitters on a tip," *Appl. Phys. Lett.*, vol. 86, p. 091911, 2005.

[21] W. E. Moerner, "Illuminating Single Molecules in Condensed Matter," *Science*, vol. 283, pp. 1670–6, Mar. 1999.

[22] F. Jelezko and J. Wrachtrup, "Single defect centres in diamond: A review," *Phys. Status Solidi A*, vol. 203, pp. 3207–25, 2006.

[23] C. Bradac, T. Gaebel, N. Naidoo, M. J. Sellars, J. Twamley, L. J. Brown, A. Barnard, T. Plakhotnik, A. V. Zvyagin, and J. R. Rabeau, "Observation and control of blinking nitrogen-vacancy centres in discrete nanodiamonds," *Nat. Nanotechnol.*, vol. 5, pp. 345–9, 2010.

[24] Y. Y. Hui, C.-L. Cheng, and H.-C. Chang, "Nanodiamonds for optical bioimaging," *J. Phys. D. Appl. Phys.*, vol. 43, pp. 1–11, 2010.

[25] D. Maclaurin, L. T. Hall, a. M. Martin, and L. C. L. Hollenberg, "Nanoscale magnetometry through quantum control of nitrogenvacancy centres in rotationally diffusing nanodiamonds," *New J. Phys.*, vol. 15, p. 013041, 2013.

[26] A. W. Schell, G. G. Kewes, T. Hanke, A. Leitenstorfer, R. Bratschitsch, O. Benson, and T. Aichele, "Single defect centers in diamond nanocrystals as quantum probes for plasmonic nanostructures," *Opt. Express*, vol. 19, pp. 7914–20, 2011.

[27] S. Schietinger, M. Barth, T. Aichele, and O. Benson, "Plasmon-Enhanced Single Photon Emission from a Nanoassembled MetalDiamond Hybrid Structure at Room Temperature," *Nano Lett.*, vol. 9, pp. 1694–8, 2009.

[28] A. Huck, S. Kumar, A. Shakoor, and U. L. Andersen, "Controlled Coupling of a Single Nitrogen-Vacancy Center to a Silver Nanowire," *Phys. Rev. Lett.*, vol. 106, p. 096801, 2011.

[29] M. Barth, J. Stingl, J. Kouba, N. Nüsse, B. Löchel, and O. Benson, "A hybrid approach towards nanophotonic devices with enhanced functionality," *Phys. Status Solidi*, vol. 246, pp. 298–301, 2009.

[30] M. Barth, N. Nüsse, B. Löchel, and O. Benson, "Controlled coupling of a single-diamond nanocrystal to a photonic crystal cavity.," *Opt. Lett.*, vol. 34, pp. 1108–10, 2009.

[31] S. Schietinger and O. Benson, "Coupling single NV-centres to high- Q whispering gallery modes of a preselected frequency-matched microresonator," *J. Phys. B At. Mol. Opt. Phys.*, vol. 42, p. 114001, 2009.

[32] J. Wolters, A. W. Schell, G. G. Kewes, N. Nusse, M. Schoengen, H. Doscher, T. Hannappel, B. Lochel, M. Barth, and O. Benson, "Enhancement of the zero phonon line emission from a single nitrogen vacancy center in a nanodiamond via coupling to a photonic crystal cavity," *Appl. Phys. Lett.*, vol. 97, p. 141108, 2010.

[33] M. Barth, S. Schietinger, S. Fischer, J. Becker, N. Nüsse, T. Aichele, B. Löchel, C. Sönnichsen, and O. Benson, "Nanoassembled plasmonic-photonic hybrid cavity for tailored light-matter coupling.," *Nano Lett.*, vol. 10, pp. 891–5, 2010.

[34] T. Schröder, F. Gädeke, M. J. Banholzer, and O. Benson, "Ultrabright and efficient single-photon generation based on nitrogen-vacancy centres in nanodiamonds on a solid immersion lens," *New J. Phys.*, vol. 13, p. 055017, 2011.

[35] K. Beha, H. Fedder, M. Wolfer, M. C. Becker, P. Siyushev, M. Jamali, A. Batalov, C. Hinz, J. Hees, L. Kirste, H. Obloh, E. Gheeraert, B. Naydenov, I. Jakobi, F. Dolde, S. Pezzagna, D. Twittchen, M. Markham, D. Dregely, H. Giessen, J. Meijer, F. Jelezko, C. E. Nebel, R. Bratschitsch, A. Leitenstorfer, and J. Wrachtrup, "Diamond nanophotonics.," *Beilstein J. Nanotechnol.*, vol. 3, pp. 895–908, 2012.

[36] T. Schröder, P. Engel, E. Schmidt, and O. Benson, "Integrated and compact fiber-coupled single-photon system based on nitrogen-vacancy centers and gradient-index lenses.," *Opt. Lett.*, vol. 37, no. 14, pp. 2901–3, 2012.

[37] T. van der Sar, Z. H. Wang, M. S. Blok, H. Bernien, T. H. Taminiau, D. M. Toyli, D. a. Lidar, D. D. Awschalom, R. Hanson, and V. V. Dobrovitski, "Decoherence-protected quantum gates for a hybrid solid-state spin register.," *Nature*, vol. 484, pp. 82–6, 2012.

[38] D. DiVincenzo, "Quantum bits: Better than excellent," *Nat Mater*, vol. 9, pp. 468–9, 2010.

[39] M. V. Gurudev Dutt, L. Childress, L. Jiang, E. Togan, J. Maze, F. Jelezko, a. S. Zibrov, P. R. Hemmer, and M. D. Lukin, "Quantum register based on individual electronic and nuclear spin qubits in diamond," *Science*, vol. 316, pp. 1312–6, 2007.

[40] L. Jiang, J. S. Hodges, J. R. Maze, P. Maurer, J. M. Taylor, D. G. Cory, P. R. Hemmer, R. L. Walsworth, A. Yacoby, a. S. Zibrov, and M. D. Lukin, "Repetitive Readout of a Single Electronic Spin via Quantum Logic with Nuclear Spin Ancillae," *Science*, vol. 326, pp. 267–72, 2009.

[41] H. Bernien, B. Hensen, W. Pfaff, G. Koolstra, M. S. Blok, L. Robledo, T. H. Taminiau, M. Markham, D. J. Twitchen, L. Childress, and R. Hanson, "Heralded entanglement between solid-state qubits separated by three metres.," *Nature*, vol. 497, pp. 86–90, 2013.

[42] J. M. Taylor, P. Cappellaro, L. Childress, L. Jiang, D. Budker, P. R. Hemmer, A. Yacoby, R. Walsworth, and M. D. Lukin, "High-sensitivity diamond magnetometer with nanoscale resolution," *Nat. Phys.*, vol. 4, pp. 810–6, 2008.

[43] G. Kucsko, P. C. Maurer, N. Y. Yao, M. Kubo, H. J. Noh, P. K. Lo, H. Park, and M. D. Lukin, “Nanometre-scale thermometry in a living cell.,” *Nature*, vol. 500, pp. 54–8, 2013.

[44] P. Neumann, I. Jakobi, F. Dolde, C. Burk, R. Reuter, G. Waldherr, J. Honert, T. Wolf, A. Brunner, J. H. Shim, D. Suter, H. Sumiya, J. Isoya, and J. Wrachtrup, “High-Precision Nanoscale Temperature Sensing Using Single Defects in Diamond.,” *Nano Lett.*, vol. 13, pp. 2738–42, 2013.

[45] D. M. Toyli, C. F. de Las Casas, D. J. Christle, V. V. Dobrovitski, and D. D. Awschalom, “Fluorescence thermometry enhanced by the quantum coherence of single spins in diamond.,” *PNAS*, vol. 110, pp. 8417–21, 2013.

[46] S. Schietinger, T. Schröder, and O. Benson, “One-by-one coupling of single defect centers in nanodiamonds to high-Q modes of an optical microresonator.,” *Nano Lett.*, vol. 8, pp. 3911–5, 2008.

[47] A. W. Schell, G. Kewes, T. Schröder, J. Wolters, T. Aichele, and O. Benson, “A scanning probe-based pick-and-place procedure for assembly of integrated quantum optical hybrid devices.,” *Rev. Sci. Instrum.*, vol. 82, p. 073709, 2011.

[48] A. Cuche, A. Drezet, Y. Sonnefraud, O. Faklaris, F. Treussart, J.-F. Roch, and S. Huant, “Near-field optical microscopy with a nanodiamond-based single-photon tip,” *Opt. Express*, vol. 17, pp. 19969–80, 2009.

[49] G. Balasubramanian, I. Y. Chan, R. Kolesov, M. Al-Hmoud, J. Tisler, C. Shin, C. Kim, A. Wojcik, P. R. Hemmer, A. Krueger, T. Hanke, A. Leitenstorfer, R. Bratschitsch, F. Jelezko, and J. J. Wrachtrup, “Nanoscale imaging magnetometry with diamond spins under ambient conditions,” *Nature*, vol. 455, pp. 648–51, 2008.

[50] P. Maletinsky, S. Hong, M. S. Grinolds, B. Hausmann, M. D. Lukin, R. L. Walsworth, M. Loncar, A. Yacoby, MaletinskyP., HongS., G. S., HausmannB., L. D., W. L., LoncarM., and YacobyA., “A robust scanning diamond sensor for nanoscale imaging with single nitrogen-vacancy centres,” *Nat. Nanotechnol.*, vol. 7, pp. 320–4, 2012.

[51] K. Dholakia and T. Čižmár, “Shaping the future of manipulation,” *Nat. Photonics*, vol. 5, pp. 335–42, 2011.

[52] O. M. Maragò, P. H. Jones, P. G. Gucciardi, G. Volpe, and A. C. Ferrari, “Optical trapping and manipulation of nanostructures,” *Nat. Nanotechnol.*, vol. 8, pp. 807–19, 2013.

[53] R. Brouri, A. Beveratos, J.-P. Poizat, and P. Grangier, “Photon antibunching in the fluorescence of individual color centers in diamond,” *Opt. Lett.*, vol. 25, pp. 1294–6, 2000.

[54] T. Schroder, A. W. Schell, G. Kewes, T. Aichele, and O. Benson, “Fiber-integrated diamond-based single photon source,” *Nano Lett.*, vol. 11, pp. 198–202, 2011.

[55] N. Mizuochi, T. Makino, H. Kato, D. Takeuchi, M. Ogura, H. Okushi, M. Nothaft, P. Neumann, A. Gali, F. Jelezko, J. Wrachtrup, and S. Yamasaki, “Electrically driven single-photon source at room temperature in diamond,” *Nat. Photonics*, vol. 6, pp. 299–303, 2012.

[56] T. M. Babinec, B. J. M. Hausmann, M. Khan, Y. Zhang, J. R. Maze, P. R. Hemmer, and M. Loncar, “A diamond nanowire single-photon source,” *Nat. Nanotechnol.*, vol. 5, pp. 195–9, 2010.

[57] D. Englund, B. Shields, K. Rivoire, F. Hatami, J. Vuckovic, H. Park, and M. D. Lukin, “Deterministic coupling of a single nitrogen vacancy center to a photonic crystal cavity,” *Nano Lett.*, vol. 10, pp. 3922–6, 2010.

[58] L. A. Stewart, Y. Zhai, J. M. Dawes, M. J. Steel, J. R. Rabeau, and M. J. Withford, “Single Photon Emission from Diamond nanocrystals in an Opal Photonic Crystal,” *Opt. Express*, vol. 17, pp. 18044–53, 2009.

[59] P. E. Barclay, K.-M. C. Fu, C. Santori, and R. G. Beausoleil, “Chip-based microcavities coupled to nitrogen-vacancy centers in single crystal diamond,” *Appl. Phys. Lett.*, vol. 95, pp. 191113–5, 2009.

[60] W. Pfaff, A. Vos, and R. Hanson, “Top-down fabrication of plasmonic nanostructures for deterministic coupling to single quantum emitters,” *J. Appl. Phys.*, vol. 113, p. 024310, 2013.

[61] C.-C. Fu, H.-Y. Lee, K. Chen, T.-S. Lim, H.-Y. Wu, P.-K. Lin, P.-K. Wei, P.-H. Tsao, H.-C. Chang, and W. Fann, “Characterization and application of single fluorescent nanodiamonds as cellular biomarkers.,” *PNAS*, vol. 104, pp. 727–32, 2007.

[62] L. T. Hall, G. C. G. Beart, E. a. Thomas, D. a. Simpson, L. P. McGuinness, J. H. Cole, J. H. Manton, R. E. Scholten, F. Jelezko, J. Wrachtrup, S. Petrou, and L. C. L. Hollenberg, “High spatial and temporal resolution wide-field imaging of neuron activity using quantum NV-diamond.,” *Sci. Rep.*, vol. 2, pp. 1–9, 2012.

[63] F. Jelezko, T. Gaebel, I. Popa, A. Gruber, and J. Wrachtrup, “Observation of coherent oscillations in a single electron spin,” *Phys. Rev. Lett.*, vol. 92, p. 76401, 2004.

[64] F. Jelezko, T. Gaebel, I. Popa, M. Domhan, A. Gruber, and J. Wrachtrup, “Observation of Coherent Oscillation of a Single Nuclear Spin and Realization of a Two-Qubit Conditional Quantum Gate,” *Phys. Rev. Lett.*, vol. 93, p. 130501, 2004.

[65] P. Neumann, N. Mizuochi, F. Rempp, P. Hemmer, H. Watanabe, S. Yamasaki, V. Jacques, T. Gaebel, F. Jelezko, and J. Wrachtrup, “Multipartite entanglement among single spins in diamond,” *Science*, vol. 320, pp. 1326–9, 2008.

[66] F. Dolde, I. Jakobi, B. Naydenov, N. Zhao, S. Pezzagna, C. Trautmann, J. Meijer, P. Neumann, F. Jelezko, and J. Wrachtrup, “Room-temperature entanglement between single defect spins in diamond,” *Nat. Phys.*, vol. 9, pp. 139–43, 2013.

[67] C. L. Degen, “Scanning magnetic field microscope with a diamond single-spin sensor,” *Appl. Phys. Lett.*, vol. 92, p. 243111, 2008.

[68] G. Balasubramanian, P. Neumann, D. Twitchen, M. Markham, R. Kolesov, N. Mizuochi, J. Isoya, J. Achard, J. Beck, J. Tissler, V. Jacques, P. R. Hemmer, F. Jelezko, and J. J. Wrachtrup, “Ultralong spin coherence time in isotopically engineered diamond,” *Nat. Mater.*, vol. 8, pp. 383–7, 2009.

[69] J. R. Maze, P. L. Stanwix, J. S. Hodges, S. Hong, J. M. Taylor, P. Cappellaro, L. Jiang, M. V. G. Dutt, E. Togan, a. S. Zibrov, A. Yacoby, R. L. Walsworth, and M. D. Lukin, “Nanoscale magnetic sensing with an individual electronic spin in diamond,” *Nature*, vol. 455, pp. 644–7, 2008.

[70] B. J. Maertz, A. P. Wijnheijmer, G. D. Fuchs, M. E. Nowakowski, and D. D. Awschalom, “Vector magnetic field microscopy using nitrogen vacancy centers in diamond,” *Appl. Phys. Lett.*, vol. 96, p. 092504, 2010.

[71] L. Rondin, J.-P. P. Tetienne, P. Spinicelli, C. D. Savio, K. Karrai, G. Dantelle, A. Thiaville, S. Rohart, J.-F. F. Roch, and V. Jacques, “Nanoscale magnetic field mapping with a single spin scanning probe magnetometer,” *Appl. Phys. Lett.*, vol. 100, pp. 153114–8, 2012.

[72] L. T. Hall, J. H. Cole, C. D. Hill, and L. C. L. Hollenberg, “Sensing of Fluctuating Nanoscale Magnetic Fields Using Nitrogen-Vacancy Centers in Diamond,” *Phys. Rev. Lett.*, vol. 103, p. 220802, 2009.

[73] F. C. Ziem, N. S. Goetz, A. Zappe, S. Steinert, and J. Wrachtrup, "Highly Sensitive Detection of Physiological Spins in a Microfluidic Device," *Nano Lett.*, vol. 13, pp. 4093–8, 2013.

[74] F. Dolde, H. Fedder, M. W. Doherty, T. Nöbauer, F. Rempp, G. Balasubramanian, T. Wolf, F. Reinhard, L. C. L. Hollenberg, F. Jelezko, and J. Wrachtrup, "Electric-fields sensing using single diamond spins," *Nat. Phys.*, vol. 7, pp. 459–63, 2011.

[75] V. M. Acosta, E. Bauch, a. Jarmola, L. J. Zipp, M. P. Ledbetter, and D. Budker, "Broadband magnetometry by infrared-absorption detection of nitrogen-vacancy ensembles in diamond," *Appl. Phys. Lett.*, vol. 97, no. 17, p. 4, 2010.

[76] Y. Mita, "Change of absorption spectra in type-Ib diamond with heavy neutron irradiation," *Phys. Rev. B*, vol. 53, pp. 11360–4, 1996.

[77] J. H. N. Loubser and J. A. van Wyk, "Electron Spin Resonance in Annealed Type 1b Diamond," *Diam. Res.*, vol. 11, pp. 4–7, 1977.

[78] J. H. N. Loubser and J. A. van Wyk, "Electron spin resonance in the study of diamond," *Reports Prog. Phys.*, vol. 41, p. 1201, 1978.

[79] L. du Preez, *PhD Thesis*. PhD thesis, University of Witwaters, 1965.

[80] G. Davies and M. F. Hamer, "Optical studies of the 1.945 eV vibronic band in diamond," *Proc. R. Soc. Lond.*, vol. 348, pp. 285–98, 1976.

[81] P. Kehayias, M. W. Doherty, D. English, R. Fischer, A. Jarmola, K. Jensen, N. Leefer, P. Hemmer, N. B. Manson, and D. Budker, "Infrared absorption band and vibronic structure of the nitrogen-vacancy center in diamond," *Phys. Rev. B*, vol. 88, no. 16, p. 165202, 2013.

[82] M. W. Doherty, N. B. Manson, P. Delaney, F. Jelezko, J. Wrachtrup, and L. C. L. Hollenberg, "The nitrogen-vacancy colour centre in diamond," *Phys. Rep.*, vol. 528, pp. 1–45, 2013.

[83] N. Aslam, G. Waldherr, P. Neumann, F. Jelezko, and J. Wrachtrup, "Photo-induced ionization dynamics of the nitrogen vacancy defect in diamond investigated by single-shot charge state detection," *New J. Phys.*, vol. 15, p. 013064, 2013.

[84] A. Gali, M. Fyta, and E. Kaxiras, "Ab initio supercell calculations on nitrogen-vacancy center in diamond: Electronic structure and hyperfine tensors," *Phys. Rev. B*, vol. 77, p. 155206, 2008.

[85] A. Gali, E. Janzen, P. Deak, G. Kresse, and E. Kaxiras, "Theory of Spin-Conserving Excitation of the N-V Center in Diamond," *Phys. Rev. Lett.*, vol. 103, p. 186404, Oct. 2009.

[86] P. Delaney, J. J. C. Greer, and J. A. Larsson, "Spin-Polarization Mechanisms of the Nitrogen-Vacancy Center in Diamond," *Nano Lett.*, vol. 10, pp. 610–4, 2010.

[87] A. Gali, T. Simon, and J. E. Lowther, "An ab initio study of local vibration modes of the nitrogen-vacancy center in diamond," *New J. Phys.*, vol. 13, p. 025016, 2011.

[88] N. Manson, J. Harrison, and M. Sellars, "Nitrogen-vacancy center in diamond: Model of the electronic structure and associated dynamics," *Phys. Rev. B*, vol. 74, pp. 1–11, Sept. 2006.

[89] F. M. Hossain, M. W. Doherty, H. F. Wilson, and L. C. L. Hollenberg, "Ab Initio Electronic and Optical Properties of the N-V Center in Diamond," *Phys. Rev. Lett.*, vol. 101, p. 226403, 2008.

[90] L. J. Rogers, S. Armstrong, M. J. Sellars, and N. B. Manson, "Infrared emission of the NV centre in diamond: Zeeman and uniaxial stress studies," *New J. Phys.*, vol. 10, p. 103024, 2008.

[91] J. Maze, A. Gali, E. Togan, Y. Chu, A. Trifonov, E. Kaxiras, and M. Lukin, "Properties of nitrogen-vacancy centers in diamond: group theoretic approach," *New J. Phys.*, vol. 13, p. 025025, 2011.

[92] M. W. Doherty, F. Dolde, H. Fedder, F. Jelezko, J. Wrachtrup, N. Manson, and L. C. L. Hollenberg, "Theory of the ground-state spin of the NV center in diamond," *Phys. Rev. B*, vol. 85, p. 205203, 2012.

[93] V. M. Acosta, A. Jarmola, E. Bauch, and D. Budker, "Optical properties of the nitrogen-vacancy singlet levels in diamond," *Phys. Rev. B*, vol. 82, p. 201202, 2010.

[94] J. Harrison, M. Sellars, and N. Manson, "Optical spin polarisation of the N-V centre in diamond," *J. Lumin.*, vol. 107, pp. 245–8, 2004.

[95] F. García de Abajo and M. Kociak, "Probing the Photonic Local Density of States with Electron Energy Loss Spectroscopy," *Phys. Rev. Lett.*, vol. 100, p. 106804, 2008.

[96] L. Novotny and B. Hecht, *Principle of Nano-Optics.* University Press, Cambridge, 2006.

[97] J. Meijer, B. Burchard, M. Domhan, C. Wittmann, T. Gaebel, I. Popa, F. Jelezko, and J. Wrachtrup, "Generation of single color centers by focused nitrogen implantation," *Appl. Phys. Lett.*, vol. 87, pp. 261903–9, 2005.

[98] J. R. Rabeau, P. Reichart, G. Tamanyan, D. N. Jamieson, S. Prawer, F. Jelezko, T. Gaebel, I. Popa, M. Domhan, and J. Wrachtrup, "Implantation of labelled single nitrogen vacancy centers in diamond using 15N," *Appl. Phys. Lett.*, vol. 88, p. 23113, 2006.

[99] D. M. Toyli, C. D. Weis, G. D. Fuchs, T. Schenkel, and D. D. Awschalom, "Chip-Scale Nanofabrication of Single Spins and Spin Arrays in Diamond," *Nano Lett.*, vol. 10, pp. 3168–72, 2010.

[100] D. Budker and D. F. Jackson Kimball, eds., *Optical Magnetometry.* Cambridge University Press, 2013.

[101] L. T. Hall, C. D. Hill, J. H. Cole, and L. C. L. Hollenberg, "Ultrasensitive diamond magnetometry using optimal dynamic decoupling," *Phys. Rev. B*, vol. 82, p. 045208, 2010.

[102] G. de Lange, Z. H. Wang, D. Ristè, V. V. Dobrovitski, and R. Hanson, "Universal dynamical decoupling of a single solid-state spin from a spin bath.," *Science*, vol. 330, pp. 60–3, 2010.

[103] B. Naydenov, F. Dolde, L. T. Hall, C. Shin, H. Fedder, L. C. L. Hollenberg, F. Jelezko, and J. Wrachtrup, "Dynamical Decoupling of a single electron spin at room temperature," *Phys. Rev. B*, vol. 83, p. 081201, 2010.

[104] T. Staudacher, F. Ziem, L. Haussler, R. Stohr, S. Steinert, F. Reinhard, J. Scharpf, A. Denisenko, and J. Wrachtrup, "Enhancing the spin properties of shallow implanted nitrogen vacancy centers in diamond by epitaxial overgrowth," *Appl. Phys. Lett.*, vol. 101, p. 212401, 2012.

[105] K. Ohno, F. Joseph Heremans, L. C. Bassett, B. A. Myers, D. M. Toyli, A. C. Bleszynski Jayich, C. J. Palmstrom, and D. D. Awschalom, "Engineering shallow spins in diamond with nitrogen delta-doping," *Appl. Phys. Lett.*, vol. 101, p. 082413, 2012.

[106] L. H. G. Tizei and M. Kociak, "Spectrally and spatially resolved cathodoluminescence of nanodiamonds: local variations of the NV(0) emission properties.," *Nanotechnology*, vol. 23, p. 175702, 2012.

[107] J. S. Hodges, L. Li, M. Lu, E. H. Chen, M. E. Trusheim, S. Allegri, X. Yao, O. Gaathon, H. Bakhru, and D. Englund, "Long-lived NV spin

coherence in high-purity diamond membranes," *New J. Phys.*, vol. 14, p. 093004, 2012.

[108] M. E. Trusheim, L. Li, A. Laraoui, E. H. Chen, H. Bakhru, T. Schroder, O. Gaathon, C. A. Meriles, and D. Englund, "Scalable Fabrication of High Purity Diamond Nanocrystals with Long-Spin-Coherence Nitrogen Vacancy Centers," *Nano Lett.*, 2013.

[109] "http://physics.mq.edu.au."

[110] T. Schroeder, M. Fujiwara, T. Noda, H.-Q. Zhao, O. Benson, S. Takeuchi, and T. Schröder, "A nanodiamond-tapered fiber system with high single-mode coupling efficiency," *Opt. Express*, vol. 20, pp. 10490–7, 2012.

[111] R. Kolesov, B. Grotz, G. Balasubramanian, R. J. Stohr, A. A. L. Nicolet, P. R. Hemmer, F. Jelezko, and J. Wrachtrup, "Wave-particle duality of single surface plasmon polaritons," *Nat. Phys.*, vol. 5, pp. 470–4, 2009.

[112] A. Cuche, O. Mollet, A. Drezet, and S. Huant, "Deterministic quantum plasmonics.," *Nano Lett.*, vol. 10, pp. 4566–70, 2010.

[113] T. Van Der Sar, E. C. Heeres, G. M. Dmochowski, G. de Lange, L. Robledo, T. H. Oosterkamp, and R. Hanson, "Nanopositioning of a diamond nanocrystal containing a single nitrogen-vacancy defect center," *Appl. Phys. Lett.*, vol. 94, p. 173104, 2009.

[114] G. Colas des Francs, G. Sanchez-Mosteiro, M. Ujue-Gonzalez, L. Markey, N. van Hulst, and A. Dereux, "Single molecules probe local density of modes (LDOS) around photonic nanostructures," *J. Microsc.*, vol. 229, pp. 210–6, 2008.

[115] J. Tisler, G. Balasubramanian, B. Naydenov, R. Kolesov, B. Grotz, R. Reuter, J.-P. Boudou, P. a. Curmi, M. Sennour, A. Thorel, M. Borsch, K. Aulenbacher, R. Erdmann, P. R. Hemmer, F. Jelezko, and J. Wrachtrup, "Fluorescence and Spin Properties of Defects in Single Digit Nanodiamonds," *ACS Nano*, vol. 3, pp. 1959–65, 2009.

[116] M. Fox, *Quantum Optics - An Introduction.* Oxford University Press, 2006.

[117] M. Orrit, "Photon Statistics in Single Molecule Experiments," *Single Mol.*, vol. 3, pp. 255–65, 2002.

[118] R. Hanbury-Brown and R. Q. Twiss, "Correlation between photons in two coherent beams of light.," *Nature*, vol. 177, pp. 27–9, 1956.

[119] A. Beveratos, R. Brouri, J. P. Poizat, P. Grangier, and P. Poizat, “Bunching and antibunching from single NV color centers in diamond,” *QCM Proc.*, pp. 1–7, 2000.

[120] G. B. Chavhan, P. S. Babyn, T. Bejoy, M. M. Shroff, and E. M. Haacke, “Principles , Techniques , and Applications of T2 * - based MR Imaging and Its Special Applications 1,” *RadioGraphics*, vol. 29, pp. 1433–49, 2009.

[121] K. C. Neuman and S. M. Block, “Optical trapping.,” *Rev. Sci. Instrum.*, vol. 75, pp. 2787–809, 2004.

[122] K. Berg-Sø rensen and H. Flyvbjerg, “Power spectrum analysis for optical tweezers,” *Rev. Sci. Instrum.*, vol. 75, p. 594, 2004.

[123] P. Zemanek, A. Jonas, L. Sramek, and M. Liska, “Optical trapping of nanoparticles and microparticles by a Gaussian standing wave,” *Opt. Lett.*, vol. 24, pp. 1448–50, 1999.

[124] F. J. García De Abajo, “Collective oscillations in optical matter,” *Opt. Express*, vol. 15, pp. 11082–94, 2007.

[125] E. Togan, Y. Chu, A. S. Trifonov, L. Jiang, J. Maze, L. Childress, M. V. G. Dutt, A. S. Sø rensen, P. R. Hemmer, A. S. Zibrov, and M. D. Lukin, “Quantum entanglement between an optical photon and a solid-state spin qubit.,” *Nature*, vol. 466, pp. 730–4, 2010.

[126] G. D. Fuchs, G. Burkard, P. V. Klimov, and D. D. Awschalom, “A quantum memory intrinsic to single nitrogenvacancy centres in diamond,” *Nat. Phys.*, vol. 7, pp. 789–93, 2011.

[127] P. Neumann, R. Kolesov, B. Naydenov, J. Beck, F. Rempp, M. Steiner, V. Jacques, G. Balasubramanian, M. L. Markham, D. J. Twitchen, S. Pezzagna, J. Meijer, J. Twamley, F. Jelezko, and J. Wrachtrup, “Quantum register based on coupled electron spins in a room-temperature solid,” *Nat. Phys.*, vol. 6, pp. 249–53, 2010.

[128] P. Galajda and P. Ormos, “Orientation of flat particles in optical tweezers by linearly polarized light,” *Opt. Express*, vol. 11, pp. 446–51, 2003.

[129] R. Gans, “The shape of ultra microscopic gold particles,” *Ann. Phys.*, vol. 37, p. 881, 1912.

[130] L. Novotny, M. Beversluis, K. Youngworth, and T. Brown, “Longitudinal Field Modes Probed by Single Molecules,” *Phys. Rev. Lett.*, vol. 86, pp. 5251–4, 2001.

[131] R. S. Schoenfeld and W. Harneit, "Real Time Magnetic Field Sensing and Imaging Using a Single Spin in Diamond," *Phys. Rev. Lett.*, vol. 106, p. 030802, 2011.

[132] A. Dréau, M. Lesik, L. Rondin, P. Spinicelli, O. Arcizet, J. F. Roch, and V. Jacques, "Avoiding power broadening in optically detected magnetic resonance of single NV defects for enhanced DC-magnetic field sensitivity," *Phys. Rev. B*, vol. 84, p. 195204, 2011.

[133] A. Balijepalli, J. J. Gorman, S. K. Gupta, and T. W. LeBrun, "Significantly Improved Trapping Lifetime of Nanoparticles in an Optical Trap using Feedback Control," *Nano Lett.*, vol. 12, pp. 2347–51, 2012.

[134] V. R. Horowitz, B. J. Alemán, D. J. Christle, A. N. Cleland, and D. D. Awschalom, "Electron spin resonance of nitrogen-vacancy centers in optically trapped nanodiamonds.," *PNAS*, vol. 109, pp. 13493–7, 2012.

[135] F. García de Abajo and A. Howie, "Retarded field calculation of electron energy loss in inhomogeneous dielectrics," *Phys. Rev. B*, vol. 65, p. 115418, 2002.

[136] R. R. Chance, A. Prock, and R. Silbey, "Lifetime of an emitting molecule near a partially reflecting surface," *J. Chem. Phys.*, vol. 60, pp. 2744–8, 1974.

[137] V. N. Mochalin, O. Shenderova, D. Ho, and Y. Gogotsi, "The properties and applications of nanodiamonds.," *Nat. Nanotechnol.*, vol. 7, pp. 11–23, 2012.

[138] L. P. Mc Guinness, Y. Yan, A. Stacey, D. A. Simpson, L. T. Hall, D. Maclaurin, S. Prawer, P. Mulvaney, J. Wrachtrup, F. Caruso, R. E. Scholten, and L. C. L. Hollenberg, "Quantum measurement and orientation tracking of fluorescent nanodiamonds inside living cells," *Nat. Nanotechnol.*, vol. 6, pp. 358–63, 2011.

[139] D. P. Di Vincenzo, *The Physical Imlpementation of Quantum Computation: Scalable Quantum Computers.* Wiley-V C H Verlag Gmbh, 2005.

[140] M. L. Juan, M. Righini, and R. Quidant, "Plasmon nano-optical tweezers," *Nat. Photonics*, vol. 5, pp. 349–56, 2011.

[141] C. Santori, P. E. Barclay, K.-M. C. Fu, R. G. Beausoleil, S. Spillane, and M. Fisch, "Nanophotonics for quantum optics using nitrogen-vacancy centers in diamond.," *Nanotechnology*, vol. 21, p. 274008, 2010.

[142] M. Barth, S. Schietinger, T. Schroeder, T. Aichele, and O. Benson, "Controlled coupling of NV defect centers to plasmonic and photonic nanostructures," *J. Lumin.*, vol. 130, pp. 1628–1634, Sept. 2010.

[143] A. G. Curto, G. Volpe, T. H. Taminiau, M. P. Kreuzer, R. Quidant, and N. F. van Hulst, "Unidirectional Emission of a Quantum Dot Coupled to a Nanoantenna," *Science*, vol. 329, pp. 930–3, 2010.

[144] C. Gruber, A. Trügler, A. Hohenau, U. Hohenester, and J. R. Krenn, "Spectral modifications and polarization dependent coupling in tailored assemblies of quantum dots and plasmonic nanowires," *Nano Lett.*, vol. 13, pp. 4257–62, 2013.

[145] D. Dregely, K. Lindfors, J. Dorfmüller, M. Hentschel, M. Becker, J. Wrachtrup, M. Lippitz, R. Vogelgesang, and H. Giessen, "Plasmonic antennas, positioning, and coupling of individual quantum systems," *Phys. Status Solidi*, vol. 249, pp. 666–77, 2012.

[146] Y. Alaverdyan, N. Vamivakas, J. Barnes, C. Lebouteiller, J. Hare, and M. Atatüre, "Spectral tunability of a plasmonic antenna with a dielectric nanocrystal," *Opt. Express*, vol. 19, p. 18175, 2011.

[147] M. Righini, P. Ghenuche, S. Cherukulappurath, V. Myroshnychenko, F. J. de Abajo, and R. Quidant, "Nano-optical Trapping of Rayleigh Particles and Escherichia coli Bacteria with Resonant Optical Antennas," *Nano Lett.*, vol. 9, pp. 3387–91, 2009.

[148] W. Zhang, L. Huang, C. Santschi, and O. J. F. Martin, "Trapping and Sensing 10 nm Metal Nanoparticles Using Plasmonic Dipole Antennas," *Nano Lett.*, vol. 10, pp. 1006–11, 2010.

[149] Y. Tanaka, S. Kaneda, and K. Sasaki, "Nanostructured potential of optical trapping using a plasmonic nanoblock pair.," *Nano Lett.*, vol. 13, pp. 2146–50, 2013.

[150] S. A. Maier, *Plasmonics: Fundamentals and Applications.* Springer, 2007.

[151] J. Becker, *Plasmons as Sensors.* Springer, 2012.

[152] G. Volpe, R. Quidant, G. Badenes, and D. Petrov, "Surface Plasmon Radiation Forces," *Phys. Rev. Lett.*, vol. 96, p. 238101, 2006.

[153] M. Righini, A. S. Zelenina, C. Girard, and R. Quidant, "Parallel and selective trapping in a patterned plasmonic landscape," *Nat. Phys.*, vol. 3, pp. 477–80, 2007.

[154] J. C. Love, L. A. Estroff, J. K. Kriebel, R. G. Nuzzo, and G. M. Whitesides, "Self-assembled monolayers of thiolates on metals as a form of nanotechnology.," *Chem. Rev.*, vol. 105, pp. 1103–70, 2005.

[155] F. J. García de Abajo and A. Howie, "Relativistic Electron Energy Loss and Electron-Induced Photon Emission in Inhomogeneous Dielectrics," *Phys. Rev. Lett.*, vol. 80, pp. 5180–3, 1998.

[156] P. B. Johnson and R. W. Christy, "Optical Constants of the Noble Metals," *Phys. Rev. Lett.*, vol. 6, p. 4370, 1972.

[157] M. Beversluis, A. Bouhelier, and L. Novotny, "Continuum generation from single gold nanostructures through near-field mediated intraband transitions," *Phys. Rev. B*, vol. 68, p. 115433, 2003.

[158] C. Bradac, T. Gaebel, N. Naidoo, J. R. Rabeau, and A. S. Barnard, "Prediction and measurement of the size-dependent stability of fluorescence in diamond over the entire nanoscale.," *Nano Lett.*, vol. 9, pp. 3555–64, 2009.

[159] E. Rittweger, K. Y. Han, S. E. S. Irvine, C. Eggeling, and S. W. S. Hell, "STED microscopy reveals crystal colour centres with nanometric resolution," *Nat. Photonics*, vol. 3, pp. 144–7, 2009.

[160] L. H. G. Tizei and M. Kociak, "Spatially Resolved Quantum Nano-Optics of Single Photons Using an Electron Microscope," *Phys. Rev. Lett.*, vol. 110, p. 153604, 2013.

[161] E. Knill, R. Laflamme, and G. J. Milburn, "A scheme for efficient quantum computation with linear optics," *Nature*, vol. 409, no. 6816, pp. 46–52, 2001.

[162] M. Marklund and P. Shukla, "Nonlinear collective effects in photon-photon and photon-plasma interactions," *Rev. Mod. Phys.*, vol. 78, pp. 591–640, 2006.

[163] X. Hu, P. Jiang, C. Ding, H. Yang, and Q. Gong, "Picosecond and low-power all-optical switching based on an organic photonic-bandgap microcavity," *Nat. Photonics*, vol. 2, pp. 185–9, 2008.

[164] M. Albert, A. Dantan, and M. Drewsen, "Cavity electromagnetically induced transparency and all-optical switching using ion Coulomb crystals," *Nat. Photonics*, vol. 5, pp. 633–6, 2011.

[165] I. Fushman, D. Englund, A. Faraon, N. Stoltz, P. Petroff, and J. Vučković, "Controlled Phase Shifts with a Single Quantum Dot," *Science*, vol. 320, pp. 769–72, 2008.

[166] M. Orrit, "Photons pushed together," *Nature*, vol. 460, 2009.

[167] M. Segal, "Single-molecule transistor: Light switch," *Nat. Nanotechnol.*, 2009.

[168] G. Wrigge, I. Gerhardt, J. Hwang, G. Zumofen, and V. Sandoghdar, "Efficient coupling of photons to a single molecule and the observation of its resonance fluorescence," *Nat. Phys.*, vol. 4, pp. 60–6, 2008.

[169] O. Chen, J. Zhao, V. Chauhan, and J. Cui, "Compact high-quality CdSeCdS coreshell nanocrystals with narrow emission linewidths and suppressed blinking," *Nat. Mater.*, vol. 12, pp. 445–451, May 2013.

[170] J. Cai, A. Retzker, F. Jelezko, and M. B. Plenio, "A large-scale quantum simulator on a diamond surface at room temperature," *Nat. Phys.*, vol. 9, pp. 168–73, 2013.

[171] P. Neumann, R. Kolesov, V. Jacques, J. Beck, J. Tisler, A. Batalov, L. Rogers, N. B. Manson, G. Balasubramanian, F. Jelezko, and J. Wrachtrup, "Excited-state spectroscopy of single NV defects in diamond using optically detected magnetic resonance," *New J. Phys.*, vol. 11, p. 13017, 2009.

[172] M. Irie, S. Kobatake, and M. Horichi, "Reversible surface morphology changes of a photochromic diarylethene single crystal by photoirradiation.," *Science*, vol. 291, pp. 1769–72, 2001.

[173] M. Pärs, C. C. Hofmann, K. Willinger, P. Bauer, M. Thelakkat, and J. Köhler, "An organic optical transistor operated under ambient conditions.," *Angew. Chem. Int. Ed. Engl.*, vol. 50, pp. 11405–8, 2011.

[174] N. D. Lai, O. Faklaris, D. Zheng, V. Jacques, H.-C. Chang, J.-F. Roch, and F. Treussart, "Quenching nitrogenvacancy center photoluminescence with an infrared pulsed laser," *New J. Phys.*, vol. 15, p. 033030, 2013.

[175] D. M. Toyli, D. J. Christle, A. Alkauskas, B. B. Buckley, C. G. Van De Walle, and D. D. Awschalom, "Measurement and Control of Single Nitrogen-Vacancy Center Spins above 600 K," *Phys. Rev. X*, vol. 2, p. 031001, 2012.

[176] L. P. Neukirch, J. Gieseler, R. Quidant, L. Novotny, and N. A. Vamivakas, "Observation of nitrogen vacancy photoluminescence from an optically levitated nanodiamond.," *Opt. Lett.*, vol. 38, pp. 2976–9, 2013.

[177] P. Siyushev, H. Pinto, M. Vörös, A. Gali, F. Jelezko, and J. Wrachtrup, "Optically Controlled Switching of the Charge State of a Single Nitrogen-Vacancy Center in Diamond at Cryogenic Temperatures," *Phys. Rev. Lett.*, vol. 110, p. 167402, 2013.

[178] T. Ishikawa, K.-M. C. Fu, C. Santori, V. M. Acosta, R. G. Beausoleil, H. Watanabe, S. Shikata, and K. M. Itoh, "Optical and spin coherence properties of nitrogen-vacancy centers placed in a 100 nm thick isotopically purified diamond layer.," *Nano Lett.*, vol. 12, pp. 2083–7, 2012.

[179] S. I. Bozhevolnyi, V. S. Volkov, E. Devaux, J.-Y. Laluet, and T. W. Ebbesen, "Channel plasmon subwavelength waveguide components including interferometers and ring resonators," *Nature*, vol. 440, pp. 508–11, 2006.

[180] A. Gonzalez-Tudela, D. Martin-Cano, E. Moreno, L. Martin-Moreno, C. Tejedor, and F. J. Garcia-Vidal, "Entanglement of Two Qubits Mediated by One-Dimensional Plasmonic Waveguides," *Phys. Rev. Lett.*, vol. 106, p. 20501, 2011.

[181] O. Arcizet, V. Jacques, A. Siria, P. Poncharal, P. Vincent, and S. Seidelin, "A single nitrogen-vacancy defect coupled to a nanomechanical oscillator," *Nat. Phys.*, vol. 7, pp. 879–83, 2011.

[182] J. Gieseler, B. Deutsch, R. Quidant, and L. Novotny, "Subkelvin Parametric Feedback Cooling of a Laser-Trapped Nanoparticle," *Phys. Rev. Lett.*, vol. 109, p. 103603, 2012.

[183] T. Li, S. Kheifets, D. Medellin, and M. G. Raizen, "Measurement of the instantaneous velocity of a Brownian particle.," *Science*, vol. 328, pp. 1673–5, 2010.

[184] T. Li, S. Kheifets, and M. G. Raizen, "Millikelvin cooling of an optically trapped microsphere in vacuum," *Nat. Phys.*, vol. 7, pp. 527–30, 2011.

List of Publications

This thesis is based on the following publications:

”Three-dimensional optical manipulation of a single electron spin”
M. Geiselmann, M. L. Juan, J. Renger, J. M. Say, L. J. Brown, F. J. García de Abajo, F. Koppens, and R. Quidant
Nature Nanotechnology **8**, 175 (2013)

”Fast optical modulation of the fluorescence from a single nitrogen vacancy centre”
M. Geiselmann, R. Marty, F. J. García de Abajo, and R. Quidant
Nature Physics **9**, 785 (2013)

”Deterministic optical-near-field-assisted positioning of nitrogen-vacancy centres”
M. Geiselmann, R. Marty, J. Renger, F. J. García de Abajo, and R. Quidant
Nano Letters, DOI: 10.1021/nl4047587